UNIVERSITY OF SOUTHAMPTON
Faculty of Engineering, Science and Mathematics
School of Engineering Sciences

Reducing the cost of crystalline silicon solar cells by using fluorescent collectors

by

Pattareeya Kittidachachan

Thesis for the degree of Doctor of Philosophy

October 2007

UNIVERSITY OF SOUTHAMPTON

ABSTRACT

FACULTY OF ENGINEERING, SCIENCE AND MATHEMATICS

SCHOOL OF ENGINEERING SCIENCES

MATERIALS RESEARCH GROUP

Doctor of Philosophy

REDUCING THE COST OF CRYSTALLINE SILICON SOLAR CELLS BY USING FLUORESCENT COLECTORS

by Pattareeya Kittidachachan

Fluorescent collectors offer the potential to reduce the cost of crystalline silicon (c-Si) solar cells, but so far their effectiveness has been demonstrated only theoretically. The major obstacles in obtaining high practical efficiency of the device are photon transport losses and material instability. This research is concerned with overcoming the first obstacle, by aiming to increase the fundamental understanding of photon transport in fluorescent collectors, and to explore the feasibility of employing these devices to improve the energy collection of c-Si solar cells.

This thesis presents the theoretical and experimental results obtained during the development and characterisation of fluorescent collectors and c-Si solar cells. Two different structures of c-Si cells were successfully fabricated. The first type was a wafer-based c-Si solar cell with an $n^+/p/p^+$ structure, and the second type was a thin-film c-Si solar cell whose structure can exploit the benefit of fluorescent concentration. Characterisation of the wafer-based device revealed the presence of a heavily doped region near the front surface. To gain a deeper insight into the influence of this layer, a theoretical model was developed and used to analyse the collection efficiency of minority carriers within the base and emitter regions of the device.

A method for preparing fluorescent collector plates was established by spin-coating dye-doped PMMA (Polymethylmethacrylate) on glass slides. An optical characterisation technique for determining re-absorption loss of the fluorescent collectors was developed and used to evaluate the performance of the fluorescent collectors based on Rhodamine 6G. The validity of this approach was verified by comparing the results

with theoretical solutions, derived using a model adapted from Weber and Lambe's theory.

The two different collector structures were developed and characterised for their electrical performance. For structures based on conventional cells, the experimental results showed a significant increase in the output current at an optimum dye concentration. The hybrid thin-film fluorescent collector was also successfully fabricated. Preliminary results showed that the performance of this novel structure with a much higher geometrical gain ratio could be improved by optimising the dye concentration, and using multiple dyes.

Contents

List of Figures

List of Tables

Acknowledgements

This thesis would not have been possible without the help from many people and organisations.

First of all, I would like to thank my supervisors Dr. Tom Markvart and Dr. Darren Bagnall for giving me an opportunity, resources, and freedom to carry out the research during my PhD study. I am deeply grateful to Tom for his patience in helping me solve technical and non-technical problems throughout my time here. Without his endless support, this thesis would not have been possible. In addition, I would like to express my special gratitude to Darren for his great advice in device design and fabrication issues.

My coworkers in the solar energy research group, Dr. Robert Greef, Dr. Lefteris Danos, and Thomas Meyer, have also helped me a great deal. I would like to thank them for all the wonderful discussions that we had throughout the years and also for their help with many experiments.

I would also like to acknowledge all technical staff from SUMC (INNOS) especially Dr. Graham, Jean, and Tony for their advice and technical assistance in device design and processing.

The help and support of all material research group members are also greatly appreciated. In particular, I would like to thank Prof. Arthur Willoughby, Dr. Janet Bonar and Dr. Suresh Uppal for their helpful discussions and valuable suggestions about diffusion mechanisms. I would also like to acknowledge Dr. Scuncai Wang for his kind help in SEM, Dr. Ling Wang and Ram for their help with the Talysurf-Profilometer. In addition, I would like to thank Dave, Rob, Eric, Chris, Erik, Brian and Gwyneth for always providing me with excellent technical and administrative support. I would also like to thank the system administrators Paul Bosson and Marcela for their computing support.

I would like to acknowledge Dr. Wilhelm Warta and Dr. Andreas Bett, Fraunhofer Institute for Solar Energy Systems, Germany, for their kind support with the reference solar cell. I am also grateful to Dr. Keith Emery and Tom Moriarty of National Renewable Energy Laboratory (NREL), and for solar cell characterisations. Also, I would like to thank Paul Basore for useful discussion about fitting experimental data with the PC1D program. Special thanks to Vichai Maneemongkolkiat, School of Electrical and Computer Engineering, Georgia Institute of Technology for the help in reflectance measurements.

With the oversight of my main supervisor, editorial advice has been sought. No changes of intellectual content were made as a result of this advice. I thank Bob, Lefteris, Max, Rakesh, Nick, Tristan, and Stuart for proof-reading my work. I also thank Ann and Aim for their great help with the Latex program.

I would like to express my gratitude to the Royal Thai Government for the financial support and also for giving me a great oppotunity to pursue my education at the University of Southampton. I would also like to acknowledge Supergen for the financial support in the experimental work of this thesis. I also wish to acknowledge the School of Engineering Sciences for some financial support during my PhD course.

Last but not least, I wish to express my deepest gratitude to my parents for their unconditional love and support. I would also like to express gratitude for all the friendship I have received during my study here; especially, thanks to Badin for always being with me through the ups and downs of my PhD experience.

List of Symbols

Symbol	Description	Unit
A	area	cm^2
D_n	diffusion coefficient of electron	cm^2/s
D_p	diffusion coefficient of hole	cm^2/s
E	energy	eV
E_{fn}	electron quasi-Fermi energy level	eV
E_{fp}	hole quasi-Fermi energy level	eV
$\mathbf{E}$	electric field	V/cm
G_n	electron generation rate per unit volume	photons/cm^3·s
G_p	hole generation rate per unit volume	photons/cm^3·s
I_{sc}	short circuit current	A
J_{sc}	short circuit current density	A/cm^2
J_{scr}	depletion region current density	A/cm^2
J_n	electron current density	A/cm^2
J_p	hole current density	A/cm^2
k	Boltzmann's constant	J/K
L_n	diffusion length of electron	cm
L_p	diffusion length of hole	cm
n	density of electrons per unit volume	cm^{-3}
n_0	equilibrium electron density	cm^{-3}
n_i	intrinsic carrier density	cm^{-3}
N_a	density of acceptor impurity atoms	cm^{-3}
N_d	density of donor impurity atoms	cm^{-3}
p	density of holes per unit volume	cm^{-3}
p_0	equilibrium hole density	cm^{-3}
q	electronic charge	C
S_n	electron surface recombination velocity	cm/s
S_p	hole surface recombination velocity	cm/s
U_n	electron recombination rate per unit volume	photons/cm^3·s

U_p	hole recombination rate per unit volume	photons/cm^3·s
V	voltage	V
V_{oc}	open circuit voltage	V
μ_n	electron mobility	cm^2/(V·s)
μ_p	hole mobility	cm^2/(V·s)
λ	wavelength of light	μm or nm
τ_n	electron lifetime	s
τ_p	hole lifetime	s
α	absorption coefficient	cm^{-1}
Φ	photon fluxes density	photons/(cm^2·s)
ϕ_f	fluorescence quantum yield	%
η_{FC}	efficiency of fluorescent colllector	%
Q_A	absorption efficiency	%
Q_C	collection efficiency	%
Φ_G	photon flux gain	
θ_c	critical angle	
∇	grad operator with respect to position	
FF	fill factor	
n	refractive index or density of electrons per unit volume	
G	geometric gain	
P	fraction of photons emitted through the critical angle	
$r(\lambda)$	re–absorption probability at wavelenght λ	
R	reflectance or resistance or re–absorption probability	
T	transmittance	

Chapter 1

Introduction

1.1 Background and Motivation

Fossil fuels like coal, oil and natural gas supply approximately 80% of the world's energy (see Fig. 1.1) [1]. These fuels are a finite resource and they are being depleted as world energy requirement is increasing dramatically. Additionally, there is a special concern about the increase in concentration of atmospheric greenhouse gases which are waste products of burning the fossil fuels. These higher concentrations leads to the enhancement of the greenhouse effect, which is the major cause of climate change [2, 3]. In view of these facts, a gradual shift from fossil fuels to renewable energy sources appears to be the proper solution to this problem.

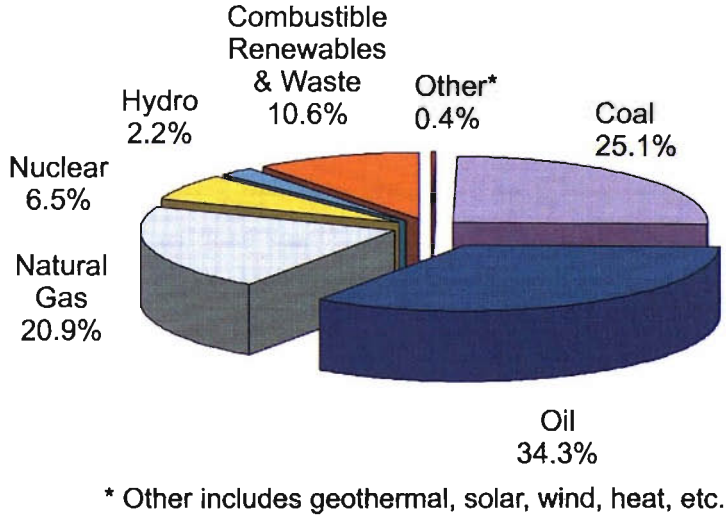

FIGURE 1.1: World energy consumption by energy source (2004) [1]

Renewable energy refers to the energy derived from resources that are regenerative or for all practical purposes can not be depleted [4]. Among the renewable energy resources available at the present, solar energy is one of the most promising candidates. This energy resource can be converted into electricity, one of the most useful forms of energy, by the use of solar cells, also known as photovoltaic (PV) cells.

Solar cells can be made from a range of materials, from the crystalline silicon (c-Si) wafers to the thin-film silicon cells and devices composed of plastic or organic semiconductors. Regarding to PV production in 2005, it was shown that c-Si accounts for 93.5% of total production [5]. The dominance of c-Si in the market can be explained by the fact that the silicon technology has already been highly developed for semiconductor devices and integrated circuits technology before the advent of photovoltaic cells. The solar cell technology, thus, gains a great benefit from this [6].

Although PV technology based on silicon has already broken the barrier of mass production and its products are widely available on the market, it has still been hampered by the costs of material processing. For this reason, several efforts are being made to overcome the high cost problem. One approach involves the development of c-Si thin film solar cells. This approach has been pursued because the silicon wafers used to make the cells are relatively expensive, making up approximately half of the final module cost. The reduction in silicon consumption is thus a driving force in the development of thin film modules [7].

Another approach is to concentrate sunlight onto the solar cells. By using a light concentrator, the solar cell is illuminated with a higher incident power and thus produces a higher electrical output. The area of the solar cells can be reduced, as a result minimising the cost. The light concentration systems can be categorised into two types: passive and active concentrators [8]. Passive or geometrical concentrators are concentrators that can concentrate light based on their geometrical system. Their operation does not rely on a frequency shift of light. Examples of the passive concentrators are mirrors and lenses. These concentrators have been widely employed in the PV concentration system to date since they have proven to be very stable and efficient in concentrating the light. However, considering the design of the concentration system, it can be seen that concentration of light by using lenses or mirrors seems to be more complicated. This is because of the limited acceptance angle of the lenses or mirrors that require them to orient towards to sun directly. As a result, the concentration systems have to be equipped with an extra mechanical system that allows them to track the sun. This tracking system, therefore, leads to the additional cost of the electrical energy produced [9].

Active concentrators are any concentrators whose operations are based on a frequency–shift mechanism. A good example of the concentrators of this type is the fluorescent collector (FC). The FC is a transparent plastic or glass plate doped with fluorescent materials. It was considered for use as a light concentrator for a solar cell because of several advantages, i.e., [10, 11]

1. it does not require a tracking system,
2. it can collect and concentrate both direct and diffuse light,
3. it has good heat dissipation from a large area of the FC plate,
4. it can select certain frequencies of light and focus them on solar cells that work best at those frequencies,
5. it can be used as a beam splitter to split the light into different spectral ranges. This feature allows the fraction of light to be concentrated and delivered to the solar cells with different band gaps.

The device, which is composed of an FC and solar cell, is generally known as fluorescent solar concentrator or fluorescent solar collector (FSC). Its conventional structure is shown in Fig. 1.2.

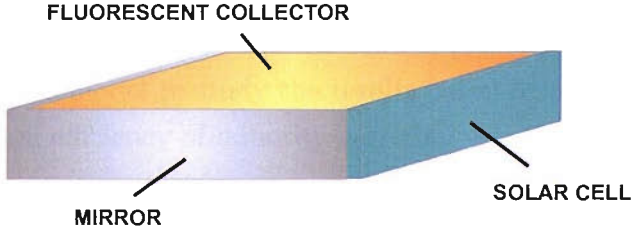

FIGURE 1.2: A schematic perspective view of a fluorescent solar collector. The device comprises a rectangular slab of fluorescent collector, a solar cell and reflecting materials.

The operation of the device relies on four major mechanisms: light absorption, light emission, light propagation and conversion of light into electricity. The absorption process begins when the light is incident onto the large area of the FC. Photons, whose wavelengths lie within the absorption band of the fluorescent materials, are absorbed and subsequently re–emitted at longer wavelengths. A large fraction of the emitted light is trapped within the FC because the refractive index of the FC is higher than that of the surrounding medium. The trapped light is then delivered to the edges of the FC via total internal reflection and converted to electricity by a solar cell.

Although the FSC has been researched for over three decades, the expected high efficiency of the device has not been realised in practice yet. One reason is probably the lag of continuous research due to the limitations of dye molecules. In recent years, the performance of dye materials is improved [12, 13]. In addition, some new advanced materials such as quantum dots[1][14] and photonic band-stop filter [15, 16] have been introduced to improve the performance of the fluorescent collectors. The research in this field has, therefore, been stimulated and has gained increasing attention from various research groups [16–23].

1.2 Aim and Objectives

The aim of this thesis is to increase the fundamental understanding of photon transport in fluorescent solar collectors and to explore the feasibility of employing fluorescent collectors to improve the energy collection of c-Si solar cells. To accomplish this aim, the research pursued the following objectives:

Development of crystalline silicon solar cells, which are one of the key components of the fluorescent solar collector.

- design, fabrication and characterisation of an experimental batch of c-Si solar cells,
- development of a model to study the results based on a detailed consideration of the collection efficiency of minority carriers.

Development and studies of the optical properties of the FC, focusing on the characterisation of photon transport losses and re-absorption losses within the FC plate.

- development of a method to prepare the fluorescent collector plates,
- development of a measurement technique to characterise the optical properties of the FC samples,
- analysis of the results using a novel modelling technique.

Integration of the FC with a solar cell.

- development of fluorescent solar collectors based on conventional c-Si solar cells, and waffle-shape thin-film c-Si devices,

[1]Quantum dots are nanometer-sized crystallite semiconductors which have advantages over dyes in that the absorption threshold and the red-shift between absorption and luminescence can be tuned by adjusting the size of the dots.

- characterisation of the electrical performance and recommendations for optimum structure.

1.3 Thesis Outline

The thesis is organised into three parts. The first part, Chapter 2-4, deals with the development and study of the performance of c-Si solar cells.

In Chapter 2, a review of literature essential to understand the principal operation of p–n junction solar cells is provided. The chapter also presents the optical properties of c–Si and interactions of light with the solar cell.

Chapter 3 describes the details of design, fabrication and characterisations of $n^+/p/p^+$ c-Si solar cells. The major results presented in this chapter are emitter doping profiles, I-V curves, spectral response characteristics and reflectance of light at the front surface.

Chapter 4 deals with the method developed to analyse the collection efficiency of minority carriers within the base and emitter of a p–n junction solar cell. The device parameters obtained from applying the method to determine the performance of the fabricated device are presented and discussed.

The second part of the thesis, Chapter 5-8, deals with the development and study of fluorescent collectors.

In Chapter 5, a literature review essential to understand the principal operation of fluorescent solar collectors is given. A review of the early work related to the development of fluorescent solar collectors is also discussed in this chapter.

Chapter 6 describes the techniques and theoretical models for quantitative analysis of FSC performance. The major parameters discussed in this chapter include: the absorption efficiency, the fluorescence quantum yield, the re-absorption probabilities, the collection efficiency and the efficiency of the fluorescent collector.

Chapter 7 presents the method and procedures to fabricate fluorescent collectors. The chapter also provides the details of the measurement systems developed to characterise the optical properties of the fluorescent collectors.

Chapter 8 presents the results obtained from the characterisations fluorescent collectors. The analysis of the experimental data is also given in this chapter.

The final part of the thesis, Chapter 9, is concerned with the development of fluorescent solar collectors. Two different structures of the FSC– conventional FSC and hybrid thin film FSC are presented and discussed. The major results obtained throughout the research and suggestions for further work are also given in this part (see Chapter 10).

Part I

Crystalline Silicon Solar Cell

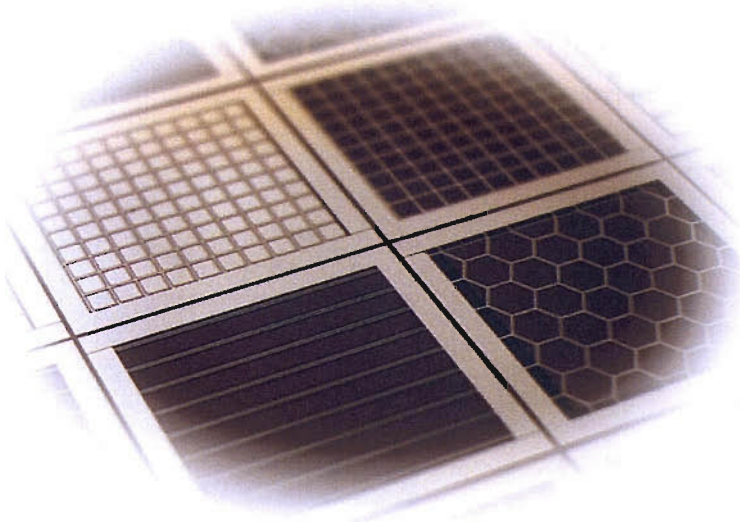

Chapter 2

Literature Review

2.1 Principal Operation of p–n Junction Solar Cell

A schematic diagram of a typical p–n junction solar cell and the basic processes that occur during the photovoltaic effect is presented in Fig. 2.1. The device is comprised of two major regions: n-type and p-type semiconductors, which are capable to conduct negative and positive charges. When the device is illuminated, the electron–hole pairs will be generated within these regions. The generated carriers may be swept across the junction by the electric field at the junction, resulting in the electricity for the connected load.

Figure 2.2 shows the energy-band diagram of the device. The charge carriers generated within the material including the transporation of charge carriers are also presented.

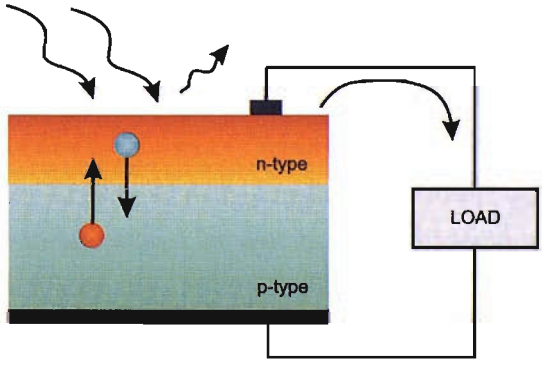

FIGURE 2.1: A schematic diagram of a typical p–n junction solar cell and the basic processes that occur during the photovoltaic effect. Three major processes include the reflection of light at the front surface, free carrier generation via the absorption of light and charge transport to the contacts.

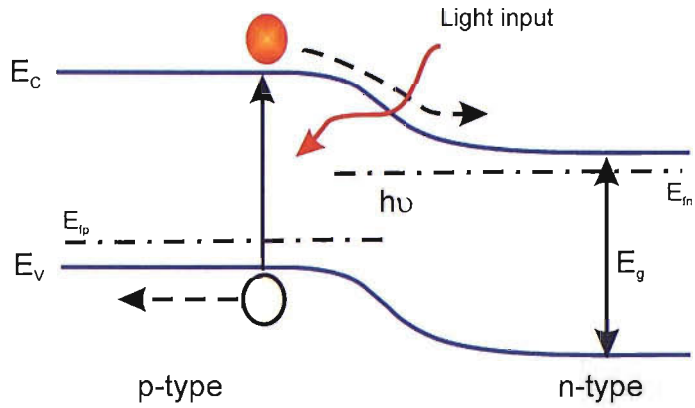

FIGURE 2.2: Energy band diagram of p–n junction solar cell. The photons, which have their energy ($h\nu$) equal or higher than the band gap energy (E_g), excite electrons from the the valence band (E_V) to the conduction band (E_C). The charge carriers generated within the material diffuse to the junction where they are swept across by the strong built-in electric field. The dotted lines E_{fp} and E_{fn} are the fermi levels of holes in the p-side and electrons in the n-side, respectively.

2.2 Theoretical Analysis of Solution of Current Densities in p–n Junction Solar Cells

2.2.1 Current Density Equations

The total or net carrier current densities in a semiconductor arise as the combined result of drift and diffusion as follows [24]:

$$J_n = q\mu_n n\mathbf{E} + qD_n\nabla n \tag{2.1}$$

$$J_p = q\mu_p p\mathbf{E} - qD_p\nabla p \tag{2.2}$$

where J_n and J_p are the electron current density and hole current density, respectively. They consist of drift component caused by electric field ($\mathbf{E}$) and a diffusion component caused by carrier concentration gradient (∇n or ∇p),
D_n and D_p are electron and hole diffusion lengths, respectively,
μ_n and μ_p are mobilities of electron and hole, respectively,
n and p are minority carriers in p-type and n-type semiconductors, respectively.

2.2.2 Continuity Equations

The continuity equations used to determine the changing rate of electrons and holes concentration per unit time are:

$$\frac{\partial n}{\partial t} = G_n - U_n + \frac{1}{q}\nabla \cdot J_n \tag{2.3}$$

$$\frac{\partial p}{\partial t} = G_p - U_p + \frac{1}{q}\nabla \cdot J_p \tag{2.4}$$

where G_n and G_p are the electron and hole generation rates caused by external influence,

U_p is the hole recombination rate in an n-type semiconductor and

U_n is the electron recombination rate in a p-type semiconductor.

2.2.3 General Solution for Current Densities in p–n Junction Solar Cells

Figure 2.3 presents the structure of the p–n junction in equilibrium and its basic parameters considered in this analysis.

To find the general solution of current densities in p–n junction solar cells, we consider a junction illuminated by a flux density of $\Phi(\lambda)$ of photons of energy $E(\lambda)$ and subject to an applied bias V.

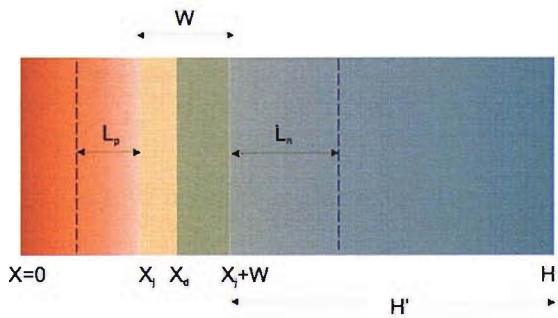

FIGURE 2.3: The p–n junction structure. W is the depletion width, L_p is the diffusion length of holes, L_n is the diffusion length of electrons, H is the cell thickness, x_j is the n-emitter neutral region, H' is the p-base neutral region and x_d is the metallurgical junction.

Additionally, for simplicity of the analysis, several assumptions have been made as follows:

- The particular system under analysis is one-dimensional, i.e., all variables are a function of just one coordinate.
- The p–n junction solar cells are being operated under steady state condition.
- The doping concentrations are uniform in both sides of the junction.
- The depletion layer is abrupt. This means the electric field vanishes at a fixed distance from both side of the junction, leaving neutral p and n-type regions.
- The injected minority carrier densities are small compared with the majority carrier densities, i.e., low–level injection assumption.
- The junction is free of interface states.
- The thermal generation-recombination is negligible throughout the depletion region.

In the electrically neutral p and n regions, the electric field is zero. The carrier current density, Eqs. 2.1 and 2.2, are simplified to

$$J_n = qD_n\frac{dn}{dx} \quad at \;\; x \geq x_j + W \tag{2.5}$$

$$J_p = -qD_p\frac{dp}{dx} \quad at \;\; x \leq x_j \tag{2.6}$$

The minority carrier diffusion equations for electrons in the neutral p region and for holes in the neutral n region are shown in Eqs. 2.7 and 2.8, respectively.

$$D_n\frac{d^2n}{dx^2} - \left(\frac{n-n_0}{\tau_n}\right) + G(E(\lambda),x) = 0 \quad for \;\; x \geq x_j + W \tag{2.7}$$

$$D_p\frac{d^2p}{dx^2} - \left(\frac{p-p_0}{\tau_p}\right) + G(E(\lambda),x) = 0 \quad for \;\; x \leq x_j \tag{2.8}$$

where τ_n and τ_p are electron and hole lifetimes, respectively.

The $G(E(\lambda),x)$ is the generation rate of electron-hole pairs after the device is illuminated by photons of energy $E(\lambda)$ in a thin layer at depth $x \rightarrow x+\delta x$. It relates to the reflectance $R(\lambda)$, absorption coefficient $\alpha(\lambda)$ and photon fluxes $\Phi(\lambda)$ as follows:

$$G(E,x) = [1 - R(\lambda)]\alpha(\lambda)\Phi(\lambda)e^{-\alpha(\lambda)x} \tag{2.9}$$

To find out the photocurrent density due to holes or electrons collected at the deletion edge, the following boundary conditions are applied:

- There exists the surface recombination velocity at the outer surface

$$-D_n\frac{dn}{dx} = S_n(n-n_0) \quad at \;\; x = H \tag{2.10}$$

$$-D_p\frac{dp}{dx} = S_p(p-p_0) \quad at \;\; x = 0 \tag{2.11}$$

- The quasi-Fermi levels (E_{Fn} and E_{Fp}) are continuous and E_{Fn}-$E_{Fp} = qV$ throughout the space charge region

$$n - n_0 = \frac{n_i^2}{N_a}\left(e^{\frac{qV}{kT}} - 1\right) \quad at \;\; x = x_j + W \tag{2.12}$$

$$p - p_0 = \frac{n_i^2}{N_d}\left(e^{\frac{qV}{kT}} - 1\right) \quad at \;\; x = x_j \tag{2.13}$$

where S_n and S_p are surface recombination velocities at $x = H$ and $x = 0$,
n_0 is an equilibrium electron density in the p region,
p_0 is an equilibrium hole density in the n region.

Solving Eqs. 2.7 and 2.8 using these boundary conditions, we obtained the solutions for the electron current density J_n at the depletion edge x_j+W and the hole current density J_p at x_j, as follows:

$$\begin{aligned} J_n &= qD_n\left(\tfrac{dn}{dx}\right)_{x_j+W} = \tfrac{q\Phi(1-R)\alpha L_n}{\alpha^2 L_n^2-1}\exp\left[-\alpha(x_j+W)\right] \\ &\times\left\{\alpha L_n - \tfrac{(S_nL_n/D_n)[\cosh(H'/L_n)-\exp(-\alpha H')]+\sinh(H'/L_n)+\alpha L_n\exp(-\alpha H')}{(S_nL_n/D_n)\sinh(H'/L_n)+\cosh(H'/L_n)}\right\} \\ &+\frac{qD_nn_0\left(e^{\frac{qV}{kT}}-1\right)}{L_n}\left\{\begin{matrix}\frac{S_nL_n}{D_n}\cosh\frac{H'}{L_n}+\sinh\frac{H'}{L_n} \\ \frac{S_nL_n}{D_n}\sinh\frac{H'}{L_n}+\cosh\frac{H'}{L_n}\end{matrix}\right\} \end{aligned} \tag{2.14}$$

$$\begin{aligned} J_p &= -qD_p\left(\tfrac{dp}{dx}\right)_{x_j} = \left[q\Phi(1-R)\alpha L_p/(\alpha^2L_p^2-1)\right] \\ &\times\left[\frac{\left(\frac{S_pL_p}{D_p}+\alpha L_p\right)-e^{-\alpha x_j}\left(\frac{S_pL_p}{D_P}\cosh\frac{x_j}{L_p}+\sinh\frac{x_j}{L_p}\right)}{(S_pL_p/D_p\sinh(x_j/L_p)+\cosh(x_j/L_p)} - \alpha L_pe^{-\alpha x_j}\right] \\ &+\frac{qD_pp_0\left(e^{\frac{qV}{kT}}-1\right)}{L_p}\left\{\begin{matrix}\frac{S_pL_p}{D_p}\cosh\frac{x_j}{L_p}+\sinh\frac{x_j}{L_p} \\ \frac{S_pL_p}{D_p}\sinh\frac{x_j}{L_p}+\cosh\frac{x_j}{L_p}\end{matrix}\right\} \end{aligned} \tag{2.15}$$

The depletion region current density can simply be determined from

$$J_{scr} = q \int_{x_j}^{x_j+W} (U - G)dx \tag{2.16}$$

J_{scr} is equal to the net electron and hole currents generated between x_j and x_j+W region. It is sometimes referred to as a recombination-generation current. J_{SCR} can be divided into two terms: the recombination current J_{rec} and the generation current J_{gen}. J_{rec} and J_{gen} can be expressed by

$$J_{rec} = q \int_{x_j}^{x_j+W} U dx \tag{2.17}$$

$$J_{gen}(\lambda) = -q \int_{x_j}^{x_j+W} G(E(\lambda), x)dx \tag{2.18}$$

If the recombination process is dominated by defect levels, the recombination rate U can be given by

$$U = \frac{np - n_i^2}{\tau_p(n + n_1) + \tau_n(p + p_1)} \tag{2.19}$$

where

$$n_1 = n_i \exp\left(\frac{E_t - E_i}{kT}\right) \quad and \quad p_1 = p_i \exp\left(\frac{E_t - E_i}{kT}\right) \tag{2.20}$$

Then, J_{rec} is can be rewritten as,

$$J_{rec} = -q \int_{x_j}^{x_j+W} \frac{np - n_i^2}{\tau_p(n + n_1) + \tau_n(p + p_1)} dx \tag{2.21}$$

Assuming that the intrinsic carrier potential energy varies linearly across the depletion region, then Eq. 2.21 can be simply expressed as [25]

$$J_{rec} = \frac{qn_i(W)}{\sqrt{\tau_n \tau_p}} \frac{2\sinh(qV/2kT)}{q(V_{bi}-V)/kT} \xi \tag{2.22}$$

where the factor ξ tends to $\pi/2$ at sufficient large forward bias. Substitute Eqs. 2.9, 2.18 and 2.22 into 2.16, we obtain

$$\begin{aligned} J_{scr} &= \frac{qn_i(W)}{\sqrt{\tau_n \tau_p}} \frac{2\sinh(qV/2kT)}{q(V_{bi}-V)/kT} \frac{\pi}{2} \\ &\quad -q \int (1-R)\Phi e^{-\alpha(x_j)}(1-e^{-\alpha(W)})d\lambda \end{aligned} \tag{2.23}$$

Equations 2.14, 2.15 and 2.23 give us the full solutions for the current-voltage characteristic of the junction in the depletion approximation. In the following sections, we consider the simplified solutions in various cases.

2.2.3.1 p–n Junction Under Dark Condition

Case I: At equilibrium

Consider the operation of the p–n junction under equilibrium, i.e., without any applied bias and illumination first. In this case the carrier populations in each region obey

$$n(x) = N_d \qquad p(x) = p_0 \qquad for \;\; x < x_j \tag{2.24}$$

$$p(x) = N_a \qquad n(x) = n_0 \qquad for \;\; x > x_j + W \tag{2.25}$$

$$pn = n_i^2 \qquad for \;\; x_j < x < x_j + W \tag{2.26}$$

Case II: Under applied bias

When the junction is biased in the forward direction, i.e., positive bias to the p region and negative bias to the n region, the built in potential barrier is reduced. This leads to the increasing of the majority carriers diffusing across the junction. The total current obtains under this case is equal to

$$J_{dark} = J_n(x_j + W) + J_p(x_j) + J_{scr} \tag{2.27}$$

J_n, J_p and J_{scr} are obtained from Eqs. 2.14, 2.15 and 2.23, respectively, with the assumption that the neutral p and n layers are thick compared to L_n and L_p. Under this case, the surface recombination becomes irrelevant and the equations can be expressed in the simple forms as follows:

$$J_n(x_j + W) = \frac{qn_i^2 D_n}{N_a L_n}\left(e^{\frac{qV}{kT}} - 1\right) \tag{2.28}$$

$$J_p(x_j) = \frac{qn_i^2 D_p}{N_d L_p}\left(e^{\frac{qV}{kT}} - 1\right) \tag{2.29}$$

$$J_{scr} = \frac{qn_i(W)}{\sqrt{\tau_n \tau_p}}\left(e^{\frac{qV}{2kT}} - 1\right) \tag{2.30}$$

Since J_n and J_p are resulted from a minority carrier diffusion, they can be grouped together and referred to as a diffusion current, J_{dif}.

$$J_{dif}(V) = J_n(x + W) + J_p(x_j) = J_{dif,0}(e^{qV/kT} - 1) \tag{2.31}$$

where

$$J_{dif,0} = qn_i^2\left(\frac{D_n}{N_a L_n} + \frac{D_p}{N_d L_p}\right) \tag{2.32}$$

The approximation form of Eq. 2.30 is given by [26]

$$J_{scr}(V) = J_{scr,0}(e^{qV/2kT} - 1) \tag{2.33}$$

where

$$J_{scr,0} = \frac{qn_i(W)}{\sqrt{\tau_n \tau_p}} \tag{2.34}$$

Substitute Eq. 2.31 and Eq. 2.33 into Eq. 2.27, we have

$$J_{dark}(V) = J_{dif,0}(e^{qV/kT} - 1) + J_{scr,0}(e^{qV/2kT} - 1) \tag{2.35}$$

This equation represents the diode equation with applied bias voltage V under dark condition.

2.2.4 p–n Junction Under Light

We consider the characteristic of the device in two cases: under no bias ($V = 0$) and under applied bias ($V \neq 0$)

Case I: Under no bias

Consider when the p–n junction is illuminated with light and with $V = 0$. In this case, the term that includes V of Eqs. 2.14 and 2.15 are vanished, resulting in the following equations:

$$\begin{aligned} J_n &= \frac{q\Phi(1-R)\alpha L_n}{\alpha^2 L_n^2 - 1} \exp\left[-\alpha(x_j + W)\right] \\ &\times \left\{\alpha L_n - \frac{(S_n L_n/D_n)[\cosh(H'/L_n) - \exp(-\alpha H')] + \sinh(H'/L_n) + \alpha L_n \exp(-\alpha H')}{(S_n L_n/D_n)\sinh(H'/L_n) + \cosh(H'/L_n)}\right\} \end{aligned} \tag{2.36}$$

$$\begin{aligned} J_p &= \left[qF(1-R)\Phi L_p/(\alpha^2 L_p^2 - 1)\right] \\ &\times \left[\frac{\left(\frac{S_p L_p}{D_p} + \alpha L_p\right) - e^{-\alpha x_j}\left(\frac{S_p L_p}{D_p}\cosh\frac{x_j}{L_p} + \sinh\frac{x_j}{L_p}\right)}{(S_p L_p/D_p)\sinh(x_j/L_p) + \cosh(x_j/L_p)} - \alpha L_p e^{-\alpha x_j}\right] \end{aligned} \tag{2.37}$$

and

$$J_{scr} = q\Phi(1-R)e^{-\alpha(x_p - W_p)}\left(1 - e^{-\alpha(W_p + W_n)}\right) \tag{2.38}$$

In this case, the total current, which will be called later as a short circuit current over that total spectrum, is

$$J_{sc} = \int (J_n + J_p + J_{scr})d\lambda \tag{2.39}$$

Case II: Under applied bias

If the cell is illuminated and $V \neq 0$, the terms that include V in Eqs. 2.14 and 2.15 are still existed. The solution for the current under this case is found by the algebraic sum of the integrated short-circuit photocurrent and dark current at that bias.

$$J(V) = J_{sc} - J_{dark}(V) \tag{2.40}$$

Substitute J_{dark} from Eq. 2.35 into Eq. 2.40, we obtain

$$J(V) = J_{sc} - \left[J_{dif,0}(e^{qV/kT} - 1) + J_{scr,0}(e^{qV/2kT} - 1)\right] \tag{2.41}$$

2.3 Device Characteristics

2.3.1 I-V Characteristic

I-V characteristic or I-V curve is a graphical presentation of the current versus the voltage from a photovoltaic device as the load is increased from the short circuit (no load) condition to the open circuit (maximum voltage) condition. The shape of the curve characterises cell performance [27].

To understand the I-V characteristic of a solar cell, it is important to consider an equivalent circuit of the device shown in Fig. 2.4. The current source represents the photocurrent (I_{ph}), the diode represents the p–n junction with reverse saturation current (I_0). The series resistance R_s is due to the conductivity of materials and the thickness of various layers. The shunt resistance R_{sh} is due to the short circuit pathways that allow charge carriers to recombine before they can be collected at the contacts. These include electrical shorts and also non-radiative recombination [28].

The I-V equation of the circuit that can be derived from Kirchhoff's current law is given by [29]

$$I = I_{ph} - I_{01}(e^{q(V+IR_s)/k_BT} - 1) - I_{02}(e^{q(V+IR_s)/2k_BT} - 1) - \frac{V + IR_s}{R_{sh}} \tag{2.42}$$

where k_B is the Boltzmann constant, T is the absolute temperature, q is the electronic charge and V is the voltage at the terminal of the cell.

Figure 2.5 shows the I-V curves of the solar cell under ideal and non-ideal conditions. The important parameters that are usually obtained from the I-V curve are:

- Short circuit current (I_{sc})
- Open circuit voltage (V_{oc})

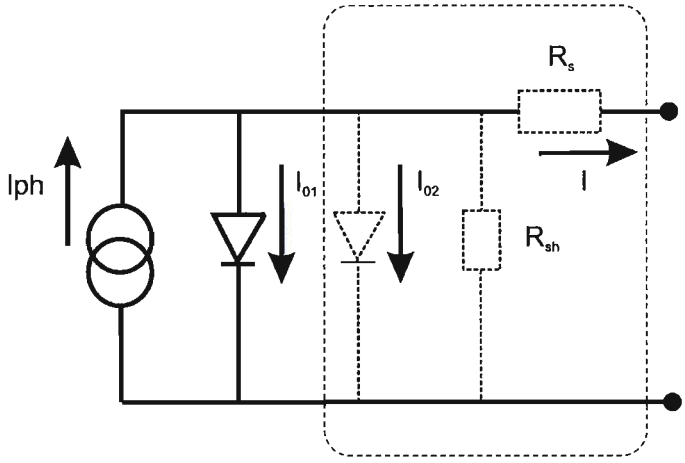

FIGURE 2.4: The equivalent circuit of an ideal solar cell (solid lines). Non ideal components are shown as the dotted lines.

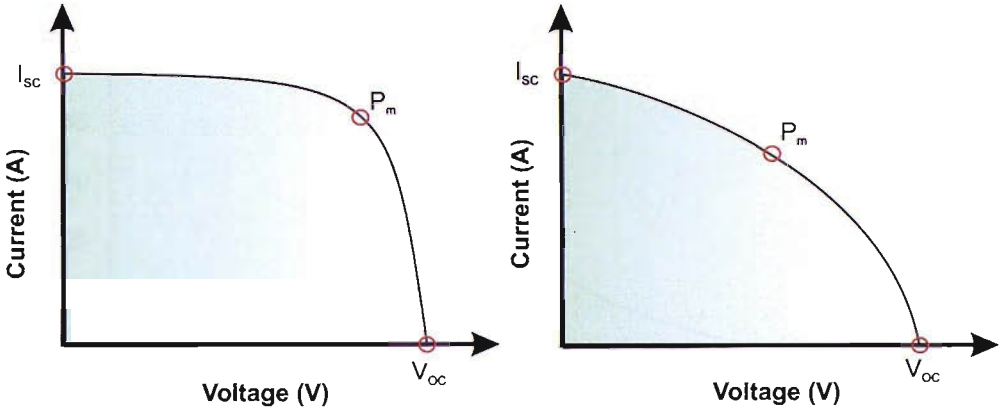

(a) Ideal solar cell

(b) Non-ideal solar cell

FIGURE 2.5: I-V curve of solar cell.

- Fill Factor (FF)
- Efficiency (η)

2.3.1.1 Short Circuit Current

Short circuit current is the maximum current that can be obtained from the solar cell when the voltage is equal to zero. This current relates directly with the incident spectral photon flux density and the probability that the incident photons will deliver the electrons to the external circuit. For the ideal condition, assume that there is no reflection of the incident light and the generated electrons and holes are collected to generate power, the photo-generated current or short circuit current is

$$I_{sc} = qA \int \Phi(\lambda) d\lambda \tag{2.43}$$

where A is the area,

$\Phi(\lambda)$ is the incident spectral photon flux density

From Eq. 2.43, we can calculate the theoretical short circuit current that solar cells can generate. Figure 2.6 illustrates the upper limit of the short circuit current density that can be obtained from the single gap semiconductor solar cells under AM1.5 condition[1].

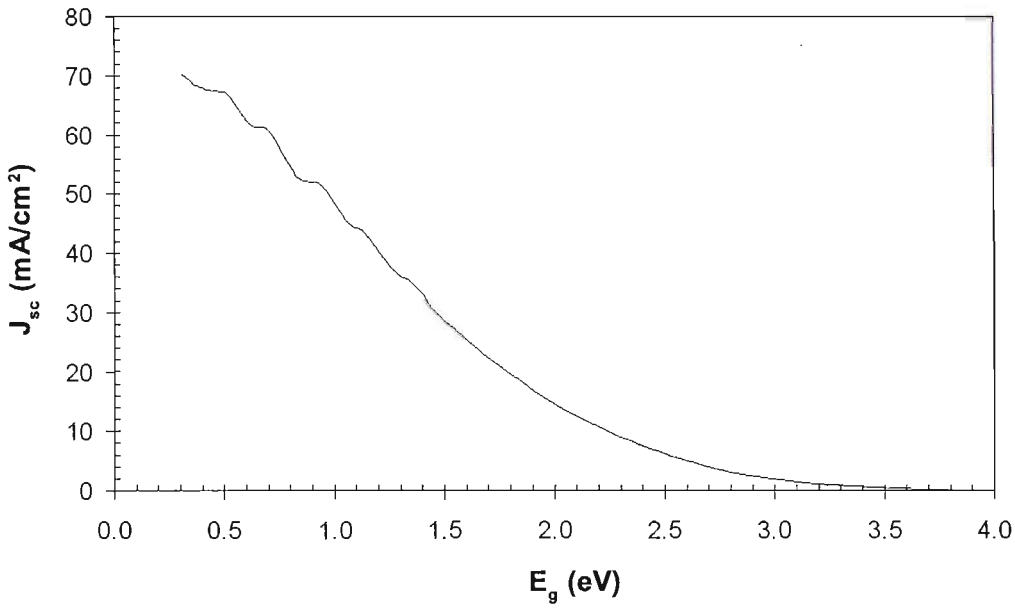

FIGURE 2.6: The theoretical limit on photo-generated current for the materials with different energy gaps.

2.3.1.2 Open Circuit Voltage

Open circuit voltage is defined as the maximum voltage that can be obtained from the solar cell under open circuit condition. This parameter can be found from the diode equation by setting $I(V) = 0$. The open circuit voltage can be expressed as

$$V_{oc} = \frac{k_B T}{q} \ln\left(\frac{I_{sc}}{I_0} + 1\right) \tag{2.44}$$

[1]AM1.5 or Air mass 1.5 is referred to the solar spectrum which has its total power density equal to 1 kW/m^2.

The theoretical upper limit value of the open circuit voltage can also be determined by employing the following equation [30]:

$$V_{oc} = \frac{E_g}{q}\left(1 - \frac{T_C}{T_S}\right) - \frac{k_B T_C}{q}\ln\left(\frac{\pi}{\omega_S}\right) + \frac{k_B T_C}{q}\ln\left(\frac{T_S}{T_C}\right) \tag{2.45}$$

where E_g is the energy gap of the solar cell,
T_S is the temperature of the sun,
T_C is the temperature of the solar cell and
ω_S is the solid angle subtended by the sun.

Figure 2.7 presents the theoretical upper limit of the open circuit voltage as a function of the energy gap of the cells calculated by using Eq. 2.45.

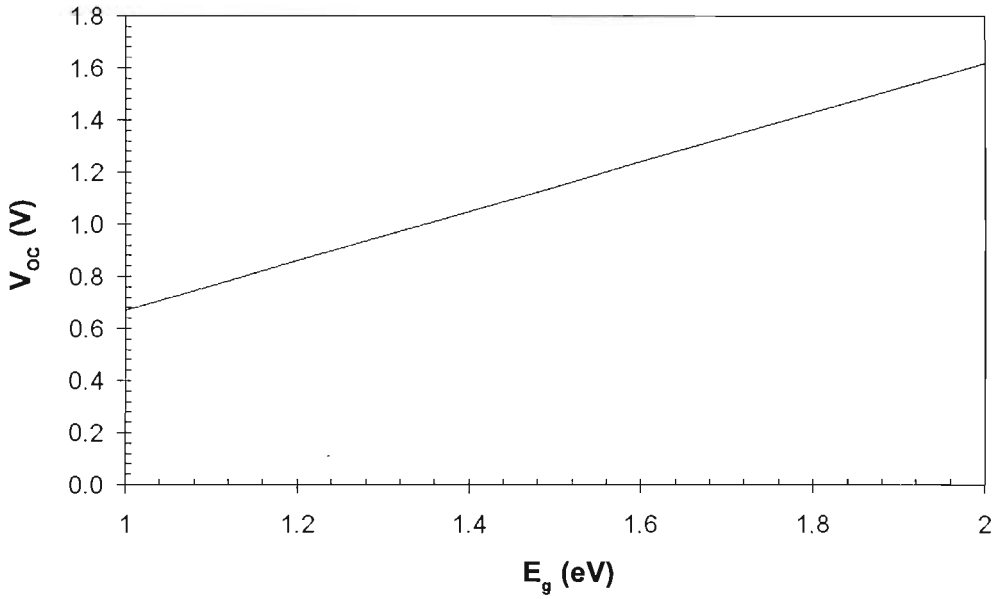

FIGURE 2.7: The theoretical limit on open-circuit voltage for the materials with different energy gaps.

2.3.1.3 Fill Factor

Fill factor is defined as the ratio of maximum power ($V_m I_m$) to the variable ($V_{oc} I_{sc}$). It is the factor which determines the squareness of the I-V curve. It is expressed as shown in Eq. 2.46.

$$FF = \frac{V_m I_m}{V_{oc} I_{sc}} \tag{2.46}$$

For the cell whose characteristics are described by a single exponential curve, the ideal fill factor of a solar cell can be approximated to a high degree of accuracy by the expression [31].

$$FF = \frac{v_{oc} - [\ln(v_{oc} + 0.72)]}{v_{oc} + 1} \tag{2.47}$$

where v_{oc} is the normalised value of the cell open-circuit voltage

$$v_{oc} = \frac{V_{oc}}{(k_B T/q)} \tag{2.48}$$

Figure 2.8 presents the theoretical limit of the fill factor.

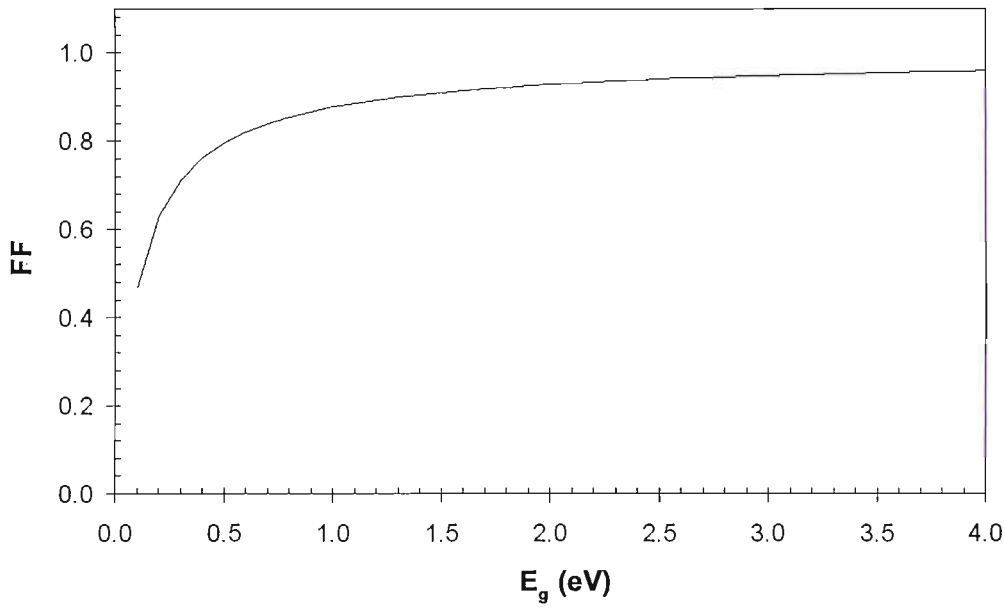

FIGURE 2.8: The theoretical limit on fill factor for the materials with different energy gaps.

2.3.1.4 Efficiency

The efficiency of a solar cell is defined as the ratio of the maximum output power P_m to the power of the incident light P_L:

$$\eta = \frac{P_m}{P_L} = \frac{FF \cdot I_{sc} \cdot V_{oc}}{P_L} \tag{2.49}$$

Based on the Shockley and Queisser theory [32], the maximum efficiency that one can obtain from the single gap solar cell is presented as shown in Figure 2.9.

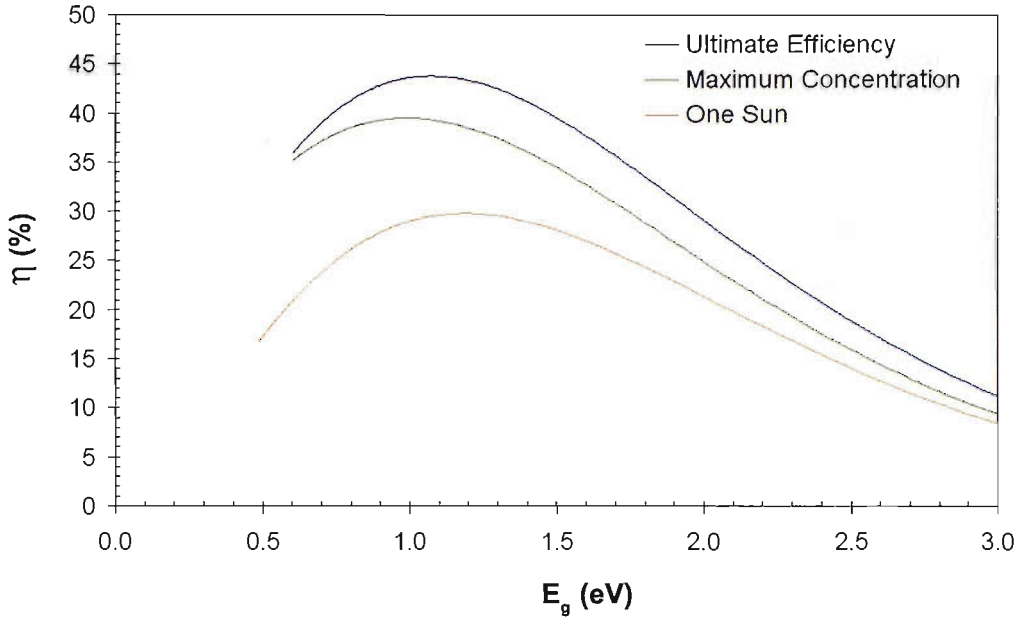

FIGURE 2.9: The theoretical limit on efficiency of p–n junction solar cells [33]. The curve labelled 'ultimate efficiency' is calculated based on the blackbody radiation with sun's temperature 6000 K. The curve labelled 'one sun' corresponds to the AM0 solar intensity, as observed outside the Earth's atmosphere. The curve labelled maximum concentration' corresponds to light focused on the cell, by a mirror or a lens, at the maximum concentration ratio of 1/f = 45,872.

2.3.2 Spectral Response and Quantum Efficiency

The spectral response of a solar cell is defined as the ratio of the output current density under short–circuit condition per unit incident power in monochromatic light as a function of wavelength. Mathematically, the spectral response of a solar cell is defined as

$$SR(\lambda) = \frac{J_{sc}(\lambda)}{I(\lambda)} \tag{2.50}$$

where $SR(\lambda)$ is the spectral response of the device at wavelength $d\lambda$,

$J_{sc}(\lambda)$ is the short–circuit current density of radiation of wavelength $d\lambda$,

$I(\lambda)$ is the incident power of monochromatic light. It relates to photon flux $\Phi(\lambda)$ and wavelength of incident light λ as follows

$$I(\lambda) = \Phi(\lambda)\frac{hc}{\lambda} \tag{2.51}$$

From the spectral response, we can determine the internal quantum efficiency (IQE) and external quantum efficiency (EQE) of the solar cell by using the following expressions:

$$IQE(\lambda) = SR(\lambda)\frac{\frac{hc}{q\lambda}}{1 - R(\lambda)} = \frac{J_{sc}(\lambda)}{q\Phi(\lambda)(1 - R(\lambda))} \tag{2.52}$$

$$EQE(\lambda) = IQE(\lambda)(1 - R(\lambda)) = SR(\lambda)\frac{hc}{q\lambda} \tag{2.53}$$

2.4 Optical Properties of Silicon

The optical properties of a material are generally related to the complex index of refraction n_c given by

$$n_c = n - i\kappa \tag{2.54}$$

The real part of n_c is the refractive index of the material, n, and the imaginary part is the extinction coefficient, κ. The refractive index is generally used to determine the reflectivity of the material. A material with high n reflects light more than a material with low n (see section 2.6). The extinction coefficient is related to the absorption coefficient of the material $\alpha(\lambda)$ by

$$\alpha(\lambda) = \frac{4\pi\kappa(\lambda)}{\lambda} \tag{2.55}$$

Figure 2.10 presents the real and imaginary parts of the refractive index of pure silicon. It can be seen that below the onset of direct bandgap energy (~3.4 eV), the extinction coefficient is very small. The complex index of refraction of silicon thus contains only the real part. The refracive index of silicon is equal to approximately 3.5

The absorption coefficient of silicon as a function of wavelength is illustrated in Fig. 2.11. At short wavelengths the absorption coefficient is very high. This means the high energy photons can excite electrons directly from states in heavily occupied valence band, to states in the lightly occupied conduction band, without changing the electron quasi-momentum. As the wavelength increases, the photon energy becomes too low

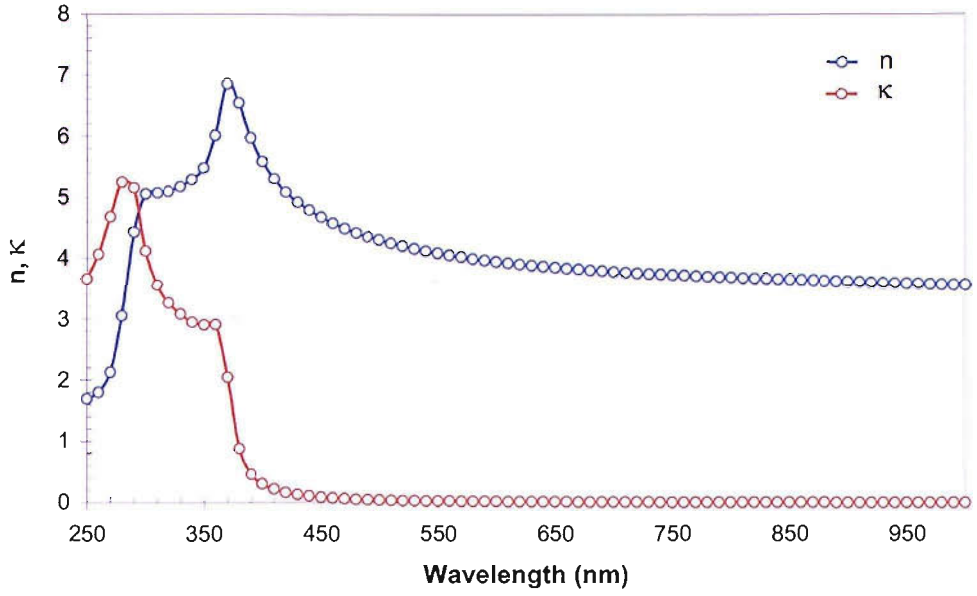

FIGURE 2.10: Real and imaginary components of the complex index of refraction for silicon at 300 K [34].

to allow direct excitation of electrons from the valence band to the conduction band. The absorption process must therefore be assisted by one or more phonons which accommodate the change in crystal momentum between the initial and final states. For wavelengths above 1100 nm, the absorption coefficient is very low. The silicon is thus effectively transparent for long wavelengths [34].

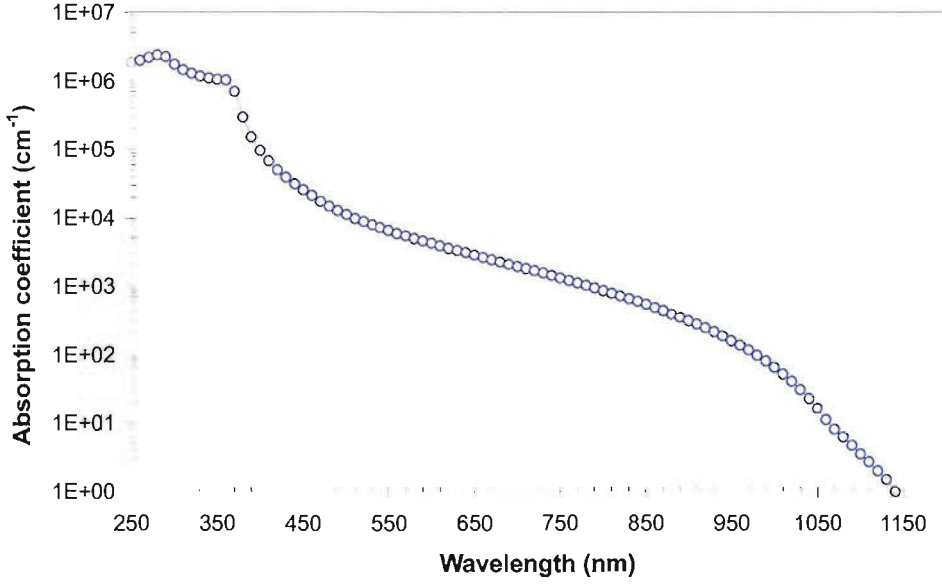

FIGURE 2.11: Absorption coefficient of pure silicon [34].

2.5 Light Absorption

The ability to absorb light of materials can be considered quantitatively through the general principle known as the Beer–Lambert law or Beer's law [35].

$$A(\lambda) = log\frac{I_0(\lambda)}{I_i(\lambda)} = \epsilon(\lambda)cd = \alpha(\lambda)d \tag{2.56}$$

where A(λ) is absorbance,

$I_0(\lambda)$ is the intensity of light leaving the absorbing medium,

$I_i(\lambda)$ is the intensity of light entering the absorbing medium,

$\epsilon(\lambda)$ is the extinction coefficient or absorptivity,

c is the molar concentration,

$\alpha(\lambda)$ is the absorption coefficient and

d is the optical path length.

According to Eq. 2.56, the intensity of light leaving the absorbing medium can be expressed as

$$I_0(\lambda) = I_i(\lambda)10^{-\epsilon(\lambda)cl} = I_i(\lambda)10^{-\alpha(\lambda)d} \tag{2.57}$$

The fraction of light absorbed within the material is given by

$$\frac{I_i(\lambda) - I_0(\lambda)}{I_i(\lambda)} = 1 - 10^{-\alpha(\lambda)d} \tag{2.58}$$

Let us now consider a beam of light, which is incident onto the front surface of a material, as shown in Fig. 2.12. Some portion of the light is reflected and some can be transmitted. The amount of light that can be absorbed within a material can be expressed as

$$\Phi_{abs} = \int_{\lambda_1}^{\lambda_2} (1 - R(\lambda))\Phi(\lambda)\left[1 - 10^{-\alpha(\lambda)d}\right] d\lambda \tag{2.59}$$

where Φ_{abs} is the number of the photons absorbed within the material,

$\Phi(\lambda)$ is the number of the photons illuminated onto the front face of the

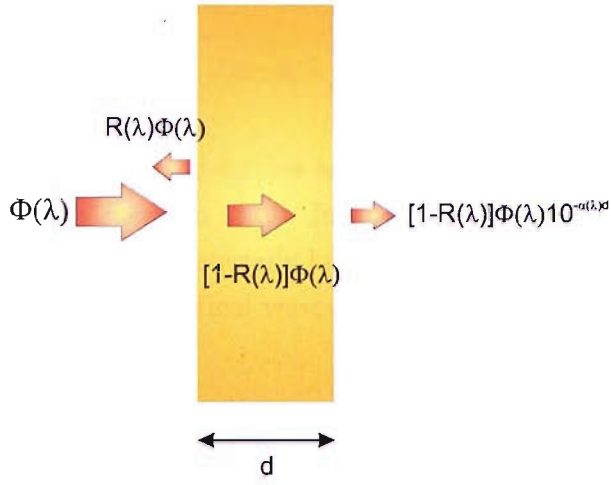

FIGURE 2.12: A beam of light as it travels through a material with thickness d.

material at wavelength $d\lambda$,
$R(\lambda)$ is the reflectance of the front surface and
d is the absorption path length.

2.6 Refraction and Reflection

2.6.1 Refraction

When light propagates from a medium of refractive index n_1 into a medium of refractive index n_2, the propagation direction changes according to

$$n_1 sin\theta_1 = n_2 sin\theta_2 \tag{2.60}$$

where θ_1 is the angle of incidence and θ_2 is the angle of refraction (see Fig. 2.13).

From Eq. 2.60, two possible cases can happen to the ray of light:

(i) the angle with the normal is decreased by refraction if the incident medium has the smaller index of refraction (Fig. 2.13(a)), or

(ii) the angle with the normal is increased by refraction, if the incident medium has the larger index of refraction (Fig. 2.13(b)).

Thus in case (ii), we can have a situation where the refracted angle reaches 90° if the angle of incidence is increased until it reaches the critical angle θ_c as given by

$$sin\theta_c = \frac{n_2}{n_1} \tag{2.61}$$

If the angle of incidence is increased further beyond the critical angle, the light will not pass through to the second medium at all. Instead, all of it will be reflected back into the first medium. This process is generally known as total internal reflection (TIR). It is important in fibre optics and optical waveguides where light is confined to the core or the waveguide media.

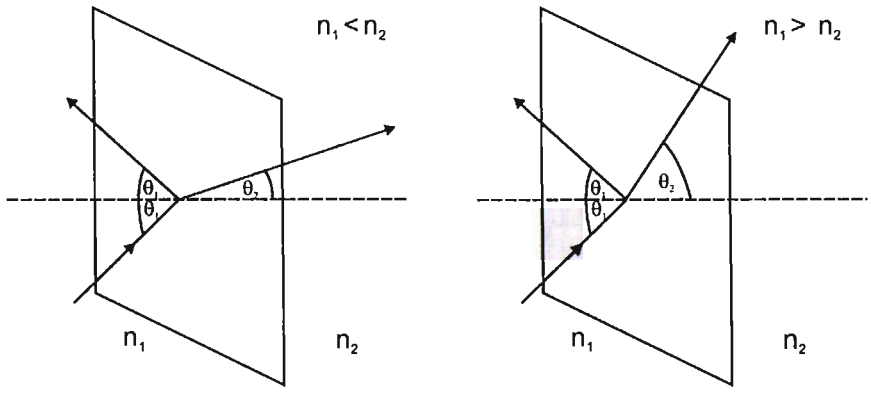

(a) The angle with the normal is decreased by refraction.

(b) The angle with the normal is increased by refraction

FIGURE 2.13: Reflection and refraction of light at the interface. The angles of incidence, reflection and refraction are denoted by θ_1 and θ_2. The parameters n_1 and n_2 denote the refractive indices in the two media [36].

2.6.2 Reflection (Fresnel's Equations)

A ray of light encountering a boundary between media with different refractive indices will not only refract, but will also partly reflect. According to the Fresnel's theory, the ratios of the amplitudes of the reflected and transmitted waves to that of the incident wave are known as the amplitude reflection and transmission coefficients, r and t. The amplitudes of these coefficients depend on the angles of incidence θ_1, the refraction θ_2 and the polarisation of the light as summarised below.

Case I: The component of the electric field E_i is parallel (||) to the plane of incidence (Fig. 2.14(a))

The reflection ($r_{||}$) and transmission ($t_{||}$) coefficients are:

$$r_{||} = \left(\frac{E_r}{E_i}\right)_{||} = \frac{n_2 cos\theta_1 - n_1 cos\theta_2}{n_2 cos\theta_1 + n_1 cos\theta_2} \tag{2.62}$$

$$t_{||} = \left(\frac{E_t}{E_i}\right)_{||} = \frac{2n_1 cos\theta_1}{n_2 cos\theta_1 + n_1 cos\theta_2} \tag{2.63}$$

Case II: The component of the electric field E_i is perpendicular to the plane of incidence (Fig. 2.14(b))

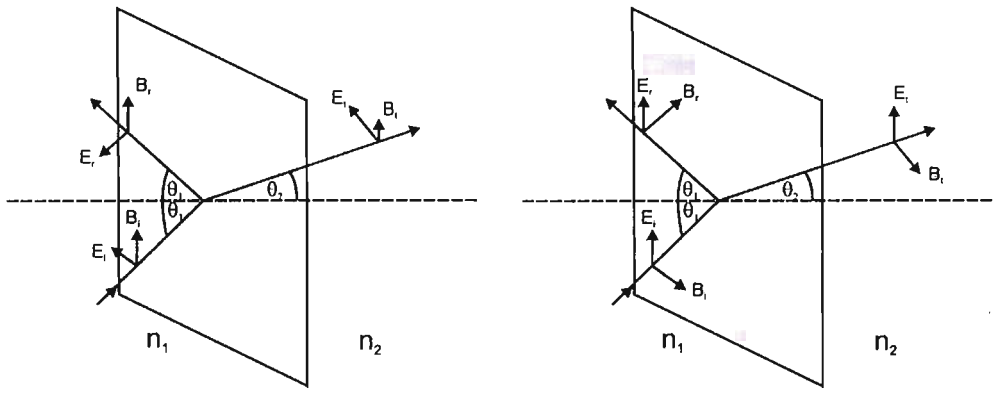

(a) The directions of the vector fields are shown for E-vector in the plane of incidence.

(b) The directions of the vector fields are shown for B-vector in the plance of incidence.

FIGURE 2.14: Reflected and refracted rays at a boundary. The angles of incidence, reflection and refraction are denoted by θ_1 and θ_2. The polarised electric and magnetic field components that are parallel (||) and perpendicular ($\perp$) to the plane of incidence are denoted by **E** and **B**. The parameters n_1 and n_2 denote the refractive indices in the two media [36].

The reflection ($r_\perp$) and transmission ($t_\perp$) coefficients are:

$$r_\perp = \left(\frac{E_r}{E_i}\right)_\perp = \frac{n_1 cos\theta_1 - n_2 cos\theta_2}{n_1 cos\theta_1 + n_2 cos\theta_2} \tag{2.64}$$

$$t_\perp = \left(\frac{E_t}{E_i}\right)_\perp = \frac{2n_1 cos\theta_1}{n_1 cos\theta_1 + n_2 cos\theta_2} \tag{2.65}$$

Using Snell's law of refraction (Eq. 2.60), the amplitude reflection and transmission coefficients can be expressed in terms of angles as follows:

$$r_{||} = \frac{tan(\theta_1 - \theta_2)}{tan(\theta_1 + \theta_2)} \tag{2.66}$$

$$r_{\perp} = \frac{sin(\theta_1 - \theta_2)}{sin(\theta_1 + \theta_2)} \tag{2.67}$$

$$t_{||} = \frac{2sin\theta_2 cos\theta_1}{sin(\theta_1 + \theta_2)cos(\theta_1 - \theta_2)} \tag{2.68}$$

$$t_{\perp} = \frac{2sin\theta_2 cos\theta_1}{sin(\theta_1 + \theta_2)} \tag{2.69}$$

The reflectance (the ratio of reflected power to incident power) R is proportional to the square of $r_{||}$ and $r_{\perp}$ as given by

$$R = \frac{1}{2}r^2 = \frac{1}{2}(|r_{||}|^2 + |r_{\perp}|^2) \tag{2.70}$$

and the transmittance is

$$T = n\left(\frac{cos\theta_2}{cos\theta_1}\right)t^2 \tag{2.71}$$

For normal incidence, the reflection and transmission coefficients are independent of polarisation. Equations 2.66-2.69 can be simplified to

$$r_{||} = -r_{\perp} = \frac{n_2 - n_1}{n_1 + n_2} \tag{2.72}$$

$$t_{||} = t_{\perp} = \frac{2n_1}{n_1 + n_2} \tag{2.73}$$

The reflectance R and transmittance T can be simply computed using the following expressions

$$R = r^2 = \left(\frac{n_2 - n_1}{n_1 + n_2}\right)^2 \tag{2.74}$$

$$T = \frac{n_2}{n_1}t^2 = \frac{4n_1n_2}{(n_1+n_2)^2} \tag{2.75}$$

For some optical devices, e.g., solar cells and photodetectors, the reflectance at the interface is considered as a loss mechanism. Hence, antireflection coatings are required to minimise this loss.

2.7 Antireflection Coatings

An antireflection (AR) coating is a thin, dielectric or metallic film, or several films, applied to an optical surface to reduce its reflectance and thereby increase its transmittance [37].

Figure 2.15 presents the basic concept of how the AR coating helps in reducing the reflectivity. Light reflected from the second interface arrives back at the first interface out of phase with that reflected from the first interface, causing destructive interference.

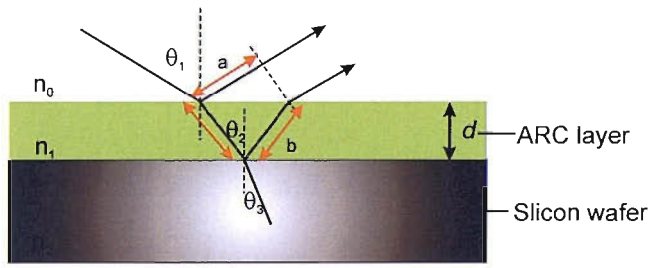

FIGURE 2.15: Single layer antireflection coating.

The expressions used to determine the reflectances for the coated surface at oblique incidence, accounting for both inteferences and the phase differences between the reflected waves, are given by [38, 39]

$$R_p = \frac{r_{01p}^2 + r_{12p}^2 + 2r_{01p}r_{12p}cos2\Theta}{1 + r_{01p}^2 r_{12p}^2 + 2r_{01p}r_{12p}cos2\Theta} \tag{2.76}$$

$$R_s = \frac{r_{01s}^2 + r_{12s}^2 + 2r_{01s}r_{12s}cos2\Theta}{1 + r_{01s}^2 r_{12s}^2 + 2r_{01s}r_{12s}cos2\Theta} \tag{2.77}$$

The average reflectance $\overline{R}$ is given by

$$\overline{R} = \frac{1}{2}(R_p + R_s) \tag{2.78}$$

where r_{01p}, r_{12p}, r_{01s}, r_{12s} are reflection coefficients at n_0-n_1 interface and n_1-n_2 interface for both the p and s polarisations:

$$r_{01p} = \frac{n_1 cos\theta_0 - n_0 cos\theta_1}{n_1 cos\theta_0 + n_0 cos\theta_1}, \qquad r_{12} = \frac{n_2 cos\theta_1 - n_1 cos\theta_2}{n_2 cos\theta_1 + n_1 cos\theta_2} \tag{2.79}$$

$$r_{01s} = \frac{n_0 cos\theta_0 - n_1 cos\theta_1}{n_0 cos\theta_0 + n_1 cos\theta_1}, \qquad r_{12} = \frac{n_1 cos\theta_1 - n_2 cos\theta_2}{n_1 cos\theta_1 + n_2 cos\theta_2} \tag{2.80}$$

Θ is the phase difference (in the external medium) between waves reflected from the first and second surfaces of the coating.

$$\Theta = \frac{2\pi n_1 d cos\theta_2}{\lambda} \tag{2.81}$$

The average reflectance has its minimum value when $\Theta = \pi/2$. At this condition, the waves reflected from the front and rear interface of the thin film are out of phase and interfere destructively. The thickness of the AR layer is expressed as

$$n_1 d = \frac{\lambda}{4} \tag{2.82}$$

and the minimum reflectance, $\overline{R}_{min}$, is given by

$$\overline{R}_{min} = \frac{(n_1^2 - n_0 n_2)^2}{(n_1^2 + n_0 n_2)^2} \tag{2.83}$$

From Eq. 2.83, the $\overline{R}_{min}$ vanishes if

$$n_1 = \sqrt{n_0 n_2} \tag{2.84}$$

Table 2.1 presents, for example, the AR coating materials used for solar cells and their refractive indices.

TABLE 2.1: AR coating materials for solar cells and their refractive indices

Material	Refractive index
SiO_2	1.4–1.5
Al_2O_3	1.8–1.9
Si_3N_4	1.9
MgF_2	1.3–1.4
TiO_2	2.3
ZnS	2.3–2.4

2.8 Loss Mechanisms in Solar Cells

Loss processes in solar cells can be classified into two types: optical losses and electrical losses. Optical losses reduce the amount of the photon flux utilised by the solar cells, whereas the electrical losses lower both current and voltage of the devices.

2.8.1 Optical Losses

Optical losses result from several reasons as follows:

- Reflection at the interface or boundary due to the difference of the refractive index of the materials.
- Shadowing of the light due to top contact structure.
- Not absorbed radiation due to the properties of the material.

2.8.2 Electrical Losses

Electrical losses in the solar cells are classified into two types: recombination losses and ohmic losses.

2.8.2.1 Recombination Losses

Recombination losses refer to the process where the minority carriers recombine before they can diffuse to the device terminal. Figure 2.16 presents the principal recombination processes which are most frequently encountered in practical operation of solar cells. These are radiative recombination, Auger recombination and recombination via defect levels.

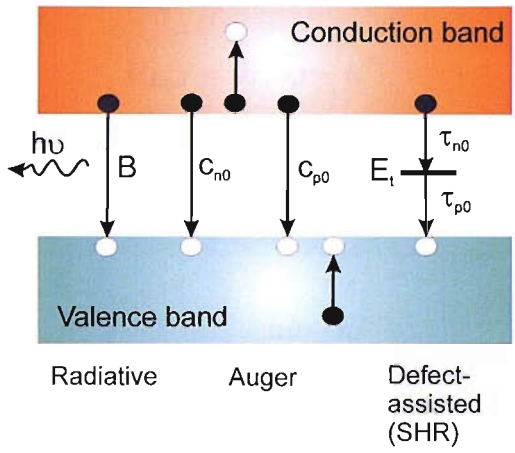

FIGURE 2.16: The principal recombination processes in solar cells [33].

■ Radiative Recombination

Radiative recombination is the term used to express the process of recombining of an electron from the conduction band with a hole in the valence band which results in the release of the excess energy in the production of a photon. This mechanism is used for semiconductor lasers and light emitting diodes, but is not particularly significant for the silicon solar cell [40].

■ Auger Recombination

In the Auger recombination process, the band-to-band recombination occurs simultaneously with the collision between two like carriers. The energy released by the recombination is transferred during the collision to the second electron in the conduction band or valence band. The excited electrons subsequently lose their energy in small steps through heat-producing collisions with the semiconductor lattice.

■ Recombination via Defect Levels

Recombination via defect levels refers to the recombination process where the minority carriers are trapped or recombined due to the presence of impurities and crystal defects. In this case the recombination of the electron and hole happens in a two-step process. First, one type of carrier, say electron, travels into the vicinity of the trap level, it is then caught by the potential well associated with the center and is trapped. Subsequently, another type of the carrier, i.e., hole in this case comes along. The hole is attracted to the trapped carrier, losses energy and annihilates the former carrier within the trap level. Equations 2.85-2.87 summarises the recombination rate of each type [33].

$$U_{Rad} = B(np - n_i^2) \tag{2.85}$$

$$U_{Auger} = (C_{p0}p + C_{n0}n)(np - n_i^2) \tag{2.86}$$

$$U_{SRH} = \frac{np - n_i^2}{\tau_p(n + n_1) + \tau_n(p + p_1)} \tag{2.87}$$

where U_{Rad} is radiative recombination rate,

U_{Auger} is Auger recombination rate,

U_{SRH} is recombination rate via defects level or also called Shockley–Read–Hall recombination.

2.8.2.2 Ohmic Loss

Figure 2.17 shows the ohmic series resistances of p–n junction solar cells. The individual resistances shown in the figure are:

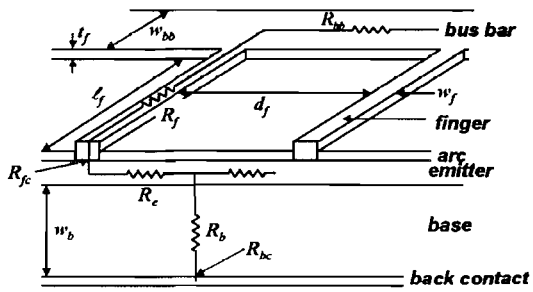

FIGURE 2.17: Series resistance in a solar cell. Figure is reproduced after [33].

R_b the resistance of the semiconductor used as base of the device,
R_e the resistance of the emitter between two grid fingers,
R_f the resistance of the grid finger,
R_{cb} the resistance of the collection bus,
R_{bc} the metal-semiconductor contact on total back surface,
R_{fc} the metal-semiconductor contact on the grid finger.

The resistances shown in the figure are related with the structure and designed parameters of the device, i.e., the spacing between grid finger d_f, the finger width w_f, the

finger length l_f, the busbar width w_{bb}, the contact thickness t_f, the base resistivity ρ_b, the base thickness w_b, the sheet resistance of the emitter $R_\square$, the metal resistivity ρ_m, the front and back contact resistivities ρ_{fc} and ρ_{bc} and the contact area A as presented in Table 2.2.

TABLE 2.2: The recombination rates of the principal recombination mechanisms

Component of resistance	**Expression**
Resistance of the base	$R_b = A w_b \rho_b$
Resistance of the emitter	$R_e = \frac{R_\square \, d_f}{7 l_f}$
Resistance of the grid finger	$R_f = \frac{l_f \rho_m}{3 t_f w_f}$
Resistance of the collection bus	$R_{bc} = \frac{\rho_m}{3 t_f w_{bb}}$
Contact resistance: front contact	$R_{fc} = \frac{\sqrt{R_\square \, \rho_{fc}}}{l_f} \coth\left(w_f \sqrt{\frac{R_\square}{\rho_{fc}}}\right)$
Contact resistance: rear contact	$R_{bc} = \frac{\rho_m}{3 t_f w_{bb}}$

Chapter 3

Fabrication and Characterisation of c-Si Solar Cells

This chapter discusses the development of c-Si solar cells at Southampton University Microelectronic Centre (SUMC)[1]. This work originated from the requirement to obtain some experience of the problems of working in this field and to understand the requirements which would be placed upon the later advanced structure. This chapter is divided into four sections. Section 3.1 describes the device design and modelling. The fabrication process flow is discussed in Section 3.2. Section 3.3 presents the measurement techniques and results of the characterisations. The major results that will be presented in this section are the emitter doping profiles, current and voltage characteristics and spectral response of the devices. The final section concludes the major results obtained from the study.

3.1 Design Considerations and Modelling

Single crystalline silicon solar cells with the $n^+/p/p^+$ structure shown in Fig. 3.1(a) were developed in this study. This structure has an advantage over the simple p–n junction structure as the p/p^+ layer provides the back surface field (BSF), creating an acceptor gradient (see Fig. 3.1(b)). The purpose of the BSF is to reduce recombination losses at the back surface of standard p–n junction solar cells, resulting in the increase of open circuit voltage, the enhancement of long wavelength response and the improvement of back contact resistance. Two major parameters considered during

[1]The cleanroom was damaged by a serious fire on 30^{th} October 2005.

the device design are the thickness of emitter and the optical reflectance at the front surface.

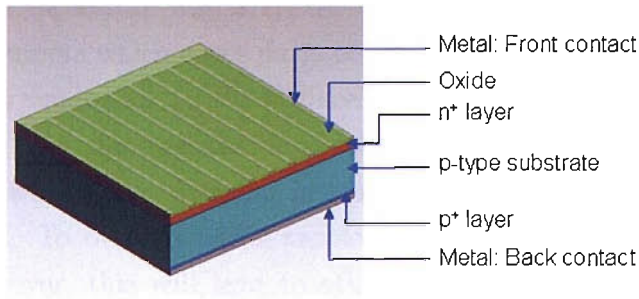

(a) The c-Si structure

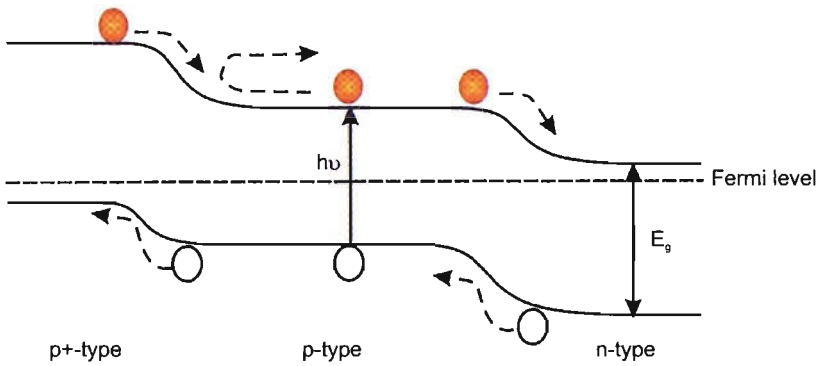

(b) The related energy band diagram

FIGURE 3.1: The structure of c-Si solar cell developed at SUMC.

3.1.1 Thickness of Emitter

One of the critical design aspects of a solar cell is the optimisation of the thickness of the emitter, i.e., the junction depth of the device. This is because the emitter thickness has a major influence on the device behaviour as follows:

- the collection probability of the generated carriers and
- the lateral series resistance in the emitter layer.

According to Eqs. 2.14 and 2.15, the electron and hole current densities decrease exponentially with increasing distance of the point of generation away from the edge of the junction depletion region. On the other hand, from Eq. 2.9, the generation rate of carriers in the semiconductor when illuminated by sunlight is highest at the surface

region ($x = 0$). Therefore to obtain the high collection probability of the generated carriers, the junction location should be as close to the surface as possible.

However, the minimisation of the junction depth will result in the enhancement of the ohmic loss. As can be seen in Fig. 2.17, the current extracted from the cell has to be collected at the contacts which cover parts of the front surface of the cell. The current generally flows perpendicular to the surface and then flows laterally to the contact region in the top layer, i.e., emitter layer of the device. Thus, the decrease of the emitter thickness will lead to a higher lateral series resistance and as a consequence higher ohmic loss. To overcome this problem, there is a need for heavy doping in the emitter. However, this will lead to other undesirable effects, such as bandgap narrowing[2] and Auger recombination. Due to these effects, care must be taken during the design in order to find a compromise between the collection probability and the ohmic loss.

In this study, the experiment was carried out to investigate the effect of emitter doping profile on the performance of the solar cell. Six different runs were carried out by varying diffusion conditions as shown in Table 3.1.

TABLE 3.1: The diffusion conditions for forming emitter layer

Condition	Diffusion Time (min)	Diffusion Temp (°C)
1	5	1000
2	10	1000
3	15	1000
4	20	1000
5	25	1000
6	30	1000

3.1.2 Optical Reflectance at Front Surface

A bare silicon wafer can reflect approximately 30%-40% of the incoming light as its refractive index is quite high (see Fig. 2.10). If unabsorbed, the light can not be used to generate electricity. Therefore, the silicon surface needs to be coated with an antireflection (AR) coating in order to minimise the reflection loss.

In this work, a thin layer of SiO_2 was used as an AR coating since it is a transparent material which has its refractive index appropriate to solar cells (see Table 2.1). In

[2]Bandgap narrowing or bandgap shrinkage refers to the mechanism in which the bandgap of semiconductors decrease at high impurities concentrations.

addition, the Si-SiO_2 interface has been proven to provide the lowest interface state density [41]. Thus, the SiO_2 can also be employed as a passivation layer.

The fraction of the light reflected from the Si-SiO_2 was modelled using the Eq. 2.83. The results derived for the normal incidence condition are shown in Fig. 3.2. The reflectance is lower when the surface is coated with the SiO_2. The minimum reflectance value also varies with the oxide thickness. Therefore, to minimise the loss due to reflectivity, the SiO_2 with the optimum thickness must be carefully chosen. It is noted from the plot that the bare Si wafer coated with 100 nm thick SiO_2 layer had the lowest total reflectance at the wavelength of approximately 600 nm. At this wavelength, the intensity of the solar spectrum is maximum. We, therefore, chose the 100 nm thick SiO_2 as the AR layer in our design. Table 3.2 summarises the reflectance of the silicon coated with SiO_2 of various thicknesses.

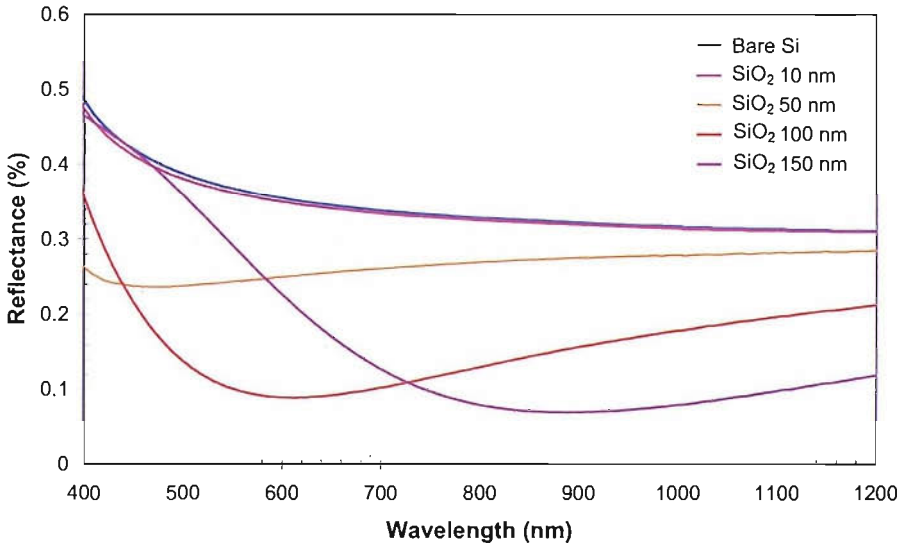

FIGURE 3.2: Percentage of light reflected from a bare silicon and silicon wafers coated with various thicknesses of SiO_2 layers.

TABLE 3.2: The reflectance between Si and SiO_2 interface

SiO_2 thickness (nm)	Minimum reflectance (%)	Total reflectance (%)
-	31.7 at 1000 ± 10 nm	37.8
10	31.5 at 1000 ± 10 nm	37.3
50	23.9 at 490 ± 10 nm	25.7
100	8.8 at 620 ± 10 nm	15.9
150	6.7 at 900 ± 10 nm	26.1

3.2 Fabrication of $n^+/p/p^+$ Silicon Solar Cells

The fabrication process flow of the solar cells with $n^+/p/p^+$ structure is shown in Fig. 3.3. The silicon wafers used in this study are float zone (FZ), p-type (100), single side polished with the resistivity of 1-3 Ω·cm (corresponding to doping concentration of 1.5×10^{16} - 4.7×10^{15} cm^{-3}). The wafers have a thickness of 416 μm and diameter of 100 mm.

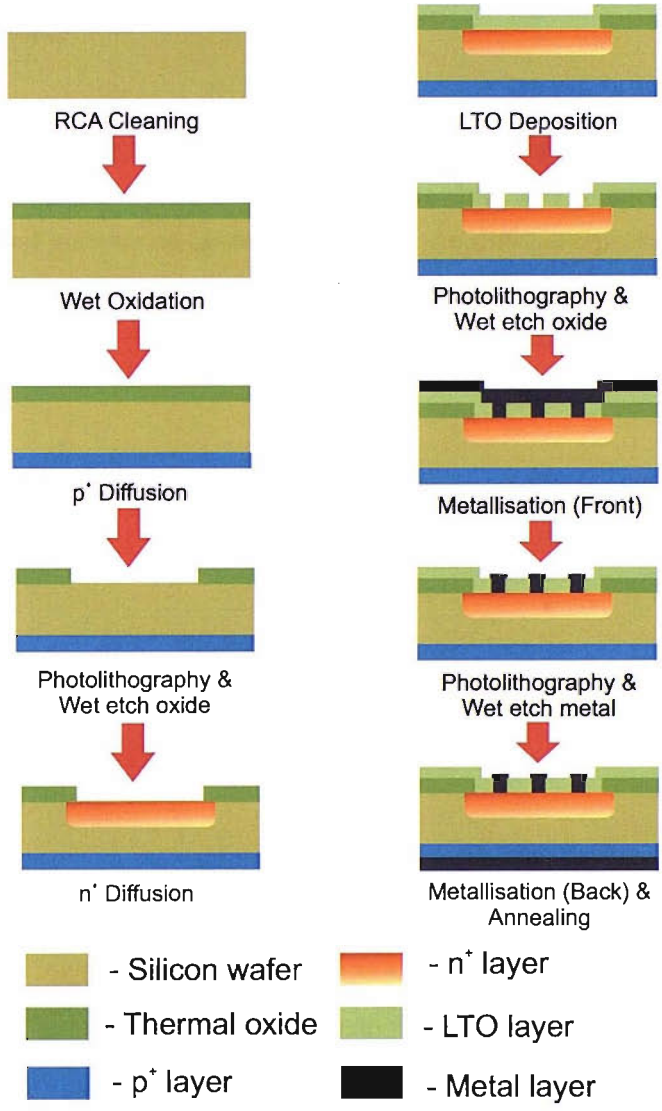

FIGURE 3.3: Process sequence for the fabrication of c-Si solar cells at SUMC.

The wafers were firstly cleaned using RCA[3] cleaning process to remove surface contaminations. The front surface was covered by a thermal oxide, 400 nm thick, in order to protect the front surface from unwanted impurities during the p^+ formation. The back surface of the substrate was then diffused with boron using 'Boron Plus', solid source tiles to create a p^+ layer back surface field (BSF). The boron was diffused at a temperature of 1050 °C for 30 minutes under a combination of gas ambients: nitrogen, wet oxygen and dry oxygen. After the Si wafers were unloaded from the furnace, the excess unreacted dopant glass (boron glass) was removed by dip etching in 20:1 HF. The sheet resistance of the p^+ layer measured from the four point probe measurement system was 30 Ohm/□.

The active area was defined to be 1 cm^2 by photolithography. An n^+ emitter layer was formed on the front surface by Phosphorus diffusion using 'Phosplus', solid source tiles at 1000 °C for 30 minutes. The conditions of the diffusion were varied as shown in Table 3.1. The sheet resistance corresponding to the diffusion process measured after the Phosphorus glass was removed is shown in Fig. 3.4.

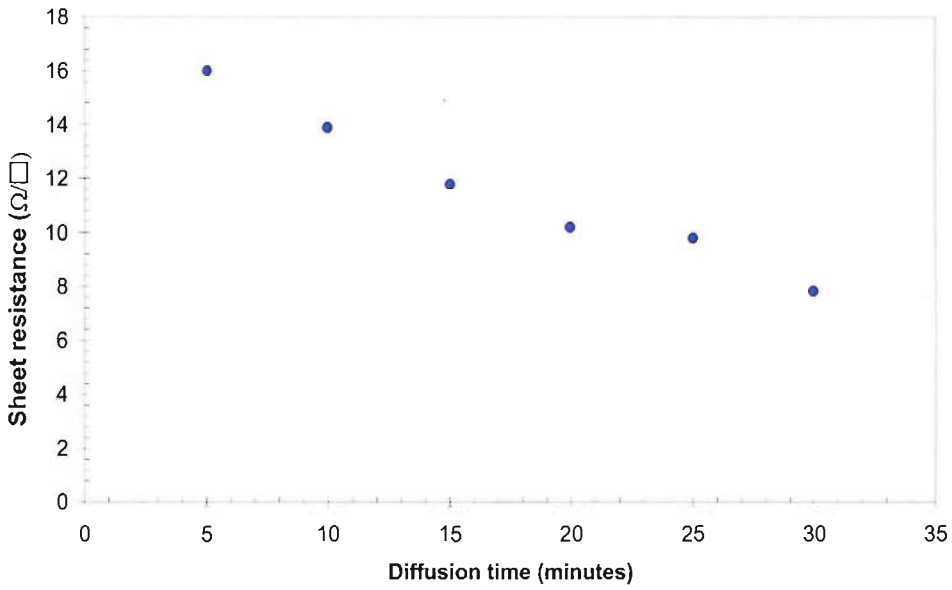

FIGURE 3.4: The relation between sheet resistance and diffusion time for temperature of 1000 °C.

Next, a thin layer of SiO_2 was deposited on the wafer front surface by low temperature oxide (LTO) deposition. This provides an antireflective layer with a minimum reflectance around 8.8% at a wavelength of 620 ± 10 nm and a total reflectance of

[3]The RCA clean is the industry standard for removing contaminants from wafers. This term is stand for Radio Corporation of America, the name of the company whose the process was first developed [42].

approximately 16% over the 400-1000 nm range. To form the n-type contact, windows were opened in the oxide using a photolithographic process. A sequence of Ti-Al layers was then evaporated onto the front to form a front grid contact pattern with a total thickness of 600 nm. The p-type contact was formed by evaporating 1000 nm of aluminium onto the rear of the wafer. The contacts were annealed in H_2/N_2 ambient at a temperature of 450 °C for 15 minutes in order to reduce the contact resistance between the metal and semiconductor.

3.3 Characterisation

3.3.1 Emitter Doping Profile

The emitter doping profiles of the fabricated devices were measured using Secondary Ion Mass Spectrometry (SIMS) and Spreading Resistance Profiling (SRP) techniques. The SIMS is a physical characterisation technique that counts all of dopant atoms, whereas the SRP is an electrical characterisation technique that measures only the electrically activated atoms [43]. In this study, these analyses were performed by Cascade Ltd. In the SIMS analysis, a beam of Cesium ions (Cs^+) with the energy of 14 keV was used to bombard the test sample. The sputtered secondary ions were then collected and analysed giving information of the dopant concentrations as shown in Fig. 3.5.

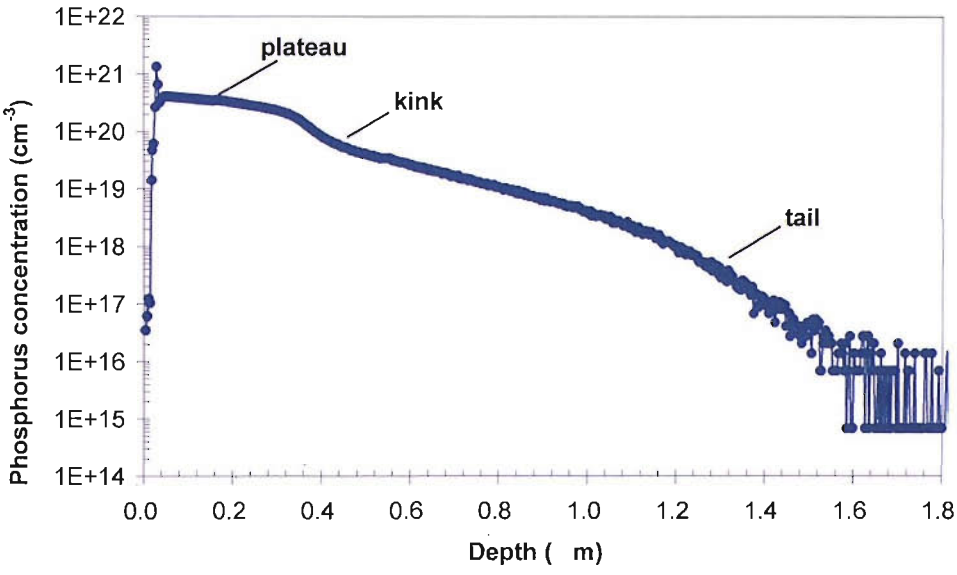

FIGURE 3.5: The emitter doping profile obtained from SIMS measurement.

It is seen that the SIMS profile shows the characteristic kink-and-tail shape. This anomalous profile has been researched extensively, and it is argued that a changeover between two different diffusion mechanisms is responsible for this characteristic [44–46]. In the high concentration region close to the surface, extrinsic diffusion occurs, dominated by the Frank-Turnbull-mechanism with a relatively low diffusion constant. In the low concentration region, much faster intrinsic diffusion takes place, governed by the kick-out-mechanisms [45]. Apart from this kink-and-tail feature, it was also noted that the flat plateau region appears close to the surface as the concentrations exceed $2\text{-}3\times10^{-20}$ cm^{-3}. This value is in good agreement with previously published values on the limit of electrically active Phosphorus in equilibrium with inactive dopants [47, 48]. This plateau region indicates that the solid solubility of phosphorus in silicon has reached its limit, resulting in the excess region of phosphorus. From the plot, it can be seen that the sensitivity of SIMS measurements was limited for detecting the dopant concentration below $\sim10^{17}$ cm^{-3}. As the substrate doping, estimated from its resistivity, is around 9.8×10^{15} cm^{-3}, it is not possible to identify the junction depth of the sample. It should be noted that the spike near the surface is a SIMS artefact, related to segregation of dopant during SIMS profiling [49].

Instead of the SIMS technique, the SRP technique was employed to measure the junction depth of the sample. The major reason is that the technique has the sensitivity down to doping level of 10^{14} cm^{-3} [43]. To investigate the junction depth by the SRP, the samples were bevelled at the optimum bevel angle for high resolution probing with the area available for profiling. The bevelling was carried out using a proprietary diamond compound which produces minimum surface damage. Raw Spreading Resistance data was acquired using a spreading resistance probe (ASR100C/2). The carrier density profiles were extracted from the resistivity profiles using the Thurbers method (ASTM standard F723) [50]. The SRP results of two samples – sample A (1000 °C, 5 minutes) and sample B (1000 °C, 30 minutes) are presented in Fig. 3.6. The junction depths of the samples can be determined from the minimum peak of the profiles. They were found to be 0.96 μm and 1.32 μm, respectively. As expected, the junction depth of sample B is higher than that of sample A. This is because sample B was diffused by the dopant atoms for a longer period of time. Considering the profile in detail, it was noticed that the concentrations of the dopant atoms at the surfaces are approximately the same. This feature implies that the vapour source was maintained at a constant level during the entire diffusion period. Another important feature of Fig. 3.6 is the steepness of the diffusion profiles at low concentrations ($C < 10^{17}$ cm^{-3}). This characteristic appears because the diffusion coefficient decreases as the concentration

decreases. The diffusion coefficient which is dependent of the dopant concentration (C) can be expressed in a simple form as [51]

$$D = D_s \left[\frac{C}{C_s}\right]^{\gamma} \tag{3.1}$$

where C_s is the surface concentration,

D is the diffusion coefficient,

D_s is the diffusion coefficient at the surface and

γ is a positive integer. It is equal to 2 for the Phosphorus diffusion [51].

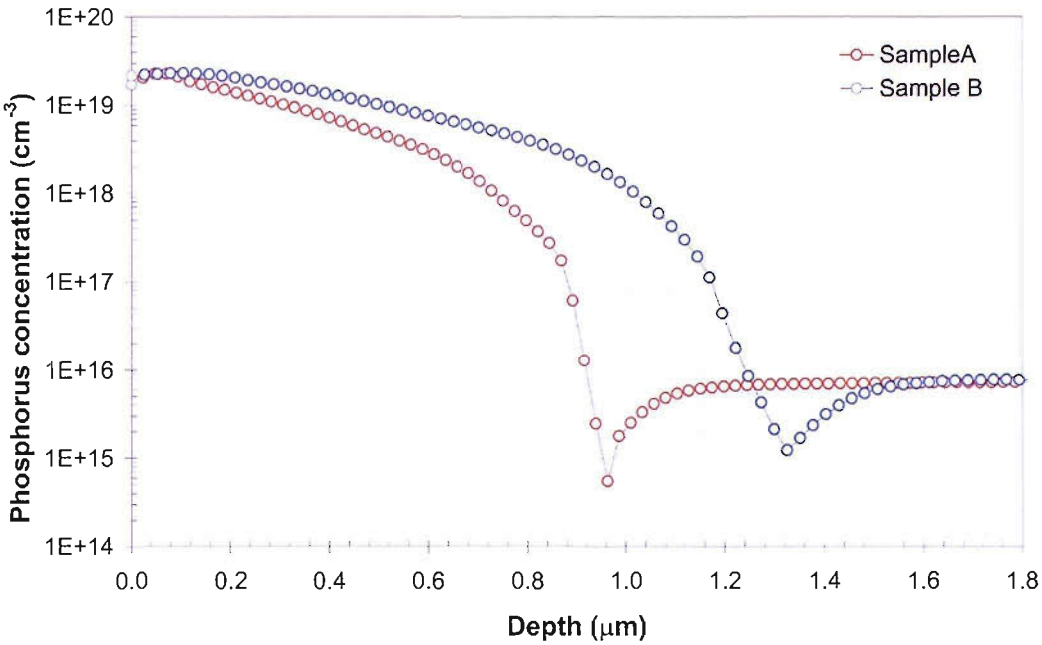

FIGURE 3.6: The emitter doping profile obtained from SRP measurement. Sample A: 5 minutes 1000 °C. Sample B: 30 minutes 1000 °C.

3.3.2 Current-Voltage Characteristics

The current-voltage (I-V) characteristics of fabricated solar cells were measured by the system shown in Fig. 3.7. The device was connected to HP4142B DC source/monitor via Kelvin connection (see Fig. 3.8). The setup separates the channels for voltage and current measurements, eliminating voltage-drop cross cables, connection and wiring, hence minimising measurement errors. Computer software controlling the HP4142B was developed as part of this work using HP-VEE 5.0. The HP4142B was programmed

to apply voltages to a solar cell, from -0.6 to +0.7 V in 0.01 V increments and sense the current from the device.

Two test conditions were used for I-V: no illumination (dark measurement) and 100 mW/cm^2 white-light standard illumination. The temperature of the cells, detected by a thermocouple placed in the immediate proximity of the measured cell, are 25 $\pm$0.1 °C and 26 $\pm$0.5 °C during the dark I-V and standard illumination I-V measurement. The standard illumination was achieved with a solar simulator, T.S. Space System Solar Simulator. In the system, a 300 W Xenon lamp was used as a light source as it can provide the spectrum approximating to the sunlight spectrum (see Fig. 3.9). The intensity of light was adjusted from the illuminator power supply. The intensity of the light source was calibrated to 100 mW/cm^2 with the help of a standard silicon solar cell of 2×2 cm^2 area. The device was calibrated at AM1.5–G condition by the National Renewable Energy Laboratory, USA.

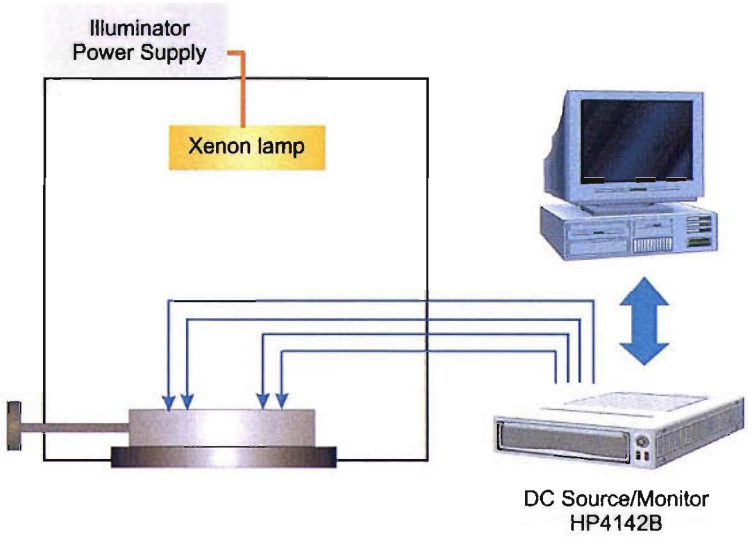

FIGURE 3.7: I-V measurement system. The system comprises a 300 W Xenon lamp, which can provide the spectrum approximating to the sunlight spectrum, an illuminating power supply for adjusting the intensity of the light source, a HP4142B DC source/monitor unit for the generation of DC biases for the device under test and for measurement of the device I–V characteristics and a computer to control and monitor the signal from the HP4142B unit.

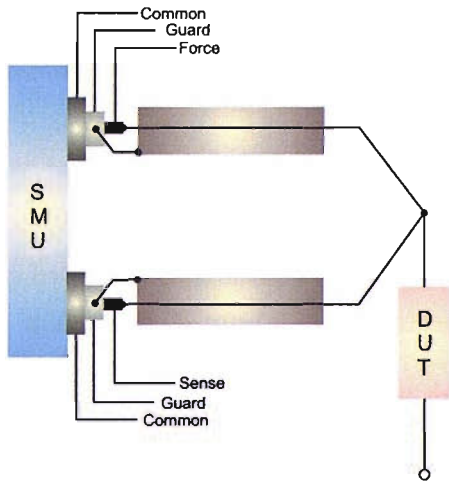

FIGURE 3.8: SMU Kelvin connection. The FORCE and SENSE cables are connected to two probes, which are contacted to the device under test (DUT), separately.

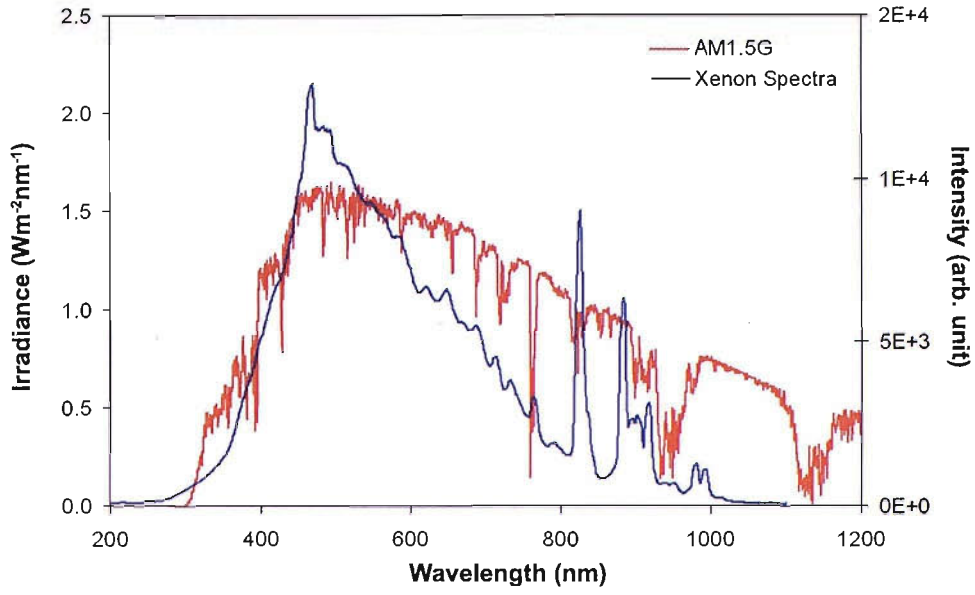

FIGURE 3.9: The spectrum of sunlight at AM1.5G and Xenon spectra.

Figures 3.10 and 3.11 show examples of I-V curves of solar cells under dark and illuminated conditions. These cells were prepared with different diffusion conditions as presented in Table 3.1. The finger spacing of the cells is 1 mm and the busbar consisted of 9 contact fingers with a spacing of 50 μm (~10% shading).

The important parameters, i.e., I_{sc}, V_{oc}, FF, R_s, R_{sh}, I_{01} and I_{02} were extracted from the illuminated I-V data, using the 'IVFIT' program[4]. The fitting results obtained from the program are presented in Table 3.3.

TABLE 3.3: The important parameters extracted from the I-V curves

Cell	I_{sc} (A)	V_{oc} (V)	FF	R_s (Ω)	R_{sh} (Ω)	I_{01} (A)	I_{02} (A)
C1	2.43×10^{-2}	0.591	0.60	1.43	125.45	7.35×10^{-13}	1.28×10^{-7}
C2	2.65×10^{-2}	0.553	0.46	1.36	45.70	8.99×10^{-14}	3.14×10^{-7}
C3	2.61×10^{-2}	0.555	0.52	1.14	66.89	6.02×10^{-14}	3.62×10^{-7}
C4	2.62×10^{-2}	0.552	0.48	1.49	50.33	7.53×10^{-14}	3.39×10^{-7}
C5	2.43×10^{-2}	0.585	0.61	1.17	156.04	1.73×10^{-14}	2.33×10^{-7}
C6	2.08×10^{-2}	0.547	0.43	4.80	53.81	1.07×10^{-13}	2.94×10^{-7}

Note that the performance of these cells is less than the theoretical limits as described in the previous chapter (see section 2.3.1). This can be observed from the non-ideal

[4]IVFIT is a free software that can be downloaded from `http://www.ecn.nl/en/zon/products-services/i-v-curve-fitting-program-ivfit/`. The program was developed by Burgers et.al [52] to fit the I-V curves both dark and illuminated conditions.

values of important cell parameters such as I_{sc}, V_{oc} and FF. The analysis also indicates that the lower I_{sc} of these cells are due to 1) high series resistances, 2) low shunt resistances and 3) high I_{01} and I_{02}. The high R_s arises from the resistance of the cell materials and also from the contacts as discussed in section 2.8.2.2. The low R_{sh} is mainly caused by the leakage current through the cell and around the edges of the device. The high values of I_{02} and I_{01} are due to the high recombination of the minority carriers within the cells which may be due to lattice defects, poor quality of surface passivation and low minority carrier lifetimes. These effects will be further analysed and discussed in more details in Chapter 4.

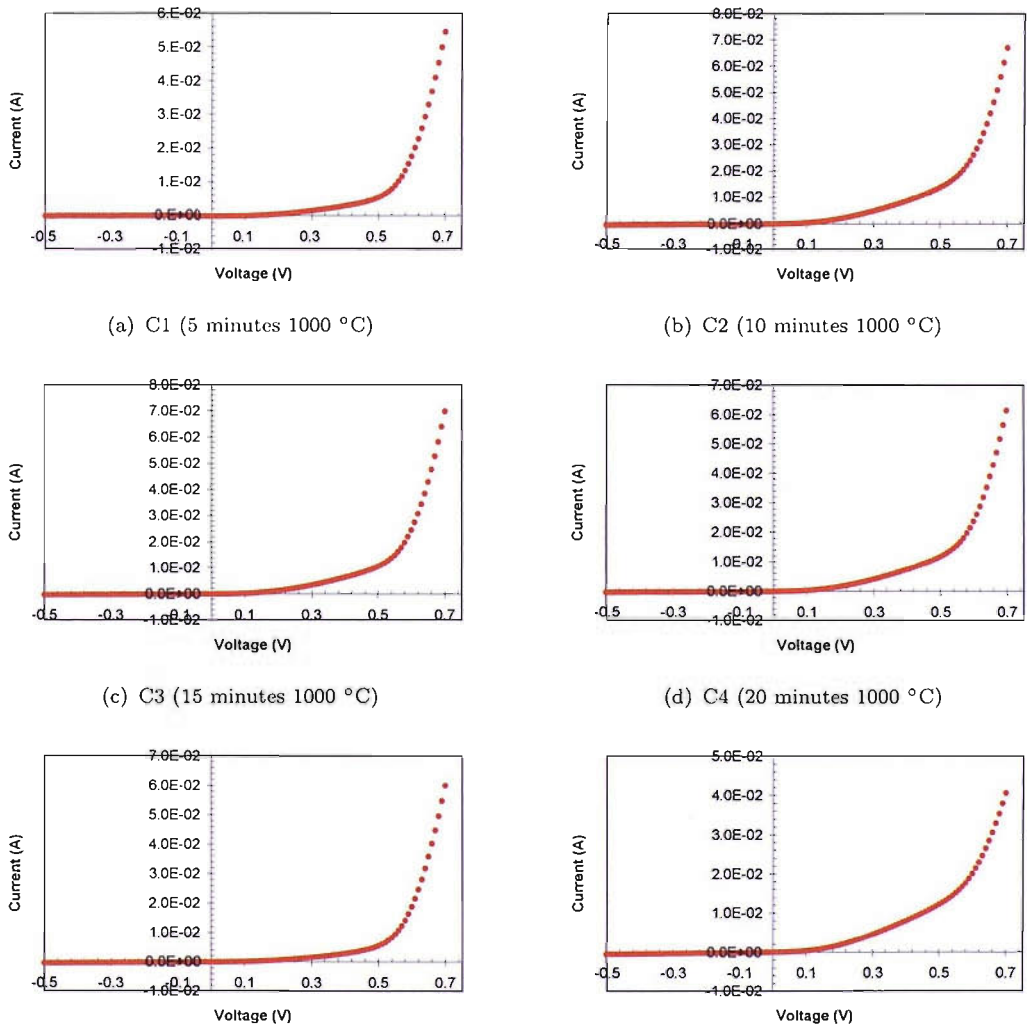

(a) C1 (5 minutes 1000 °C)

(b) C2 (10 minutes 1000 °C)

(c) C3 (15 minutes 1000 °C)

(d) C4 (20 minutes 1000 °C)

(e) C5 (25 minutes 1000 °C)

(f) C6 (30 minutes 1000 °C)

FIGURE 3.10: I-V characteristics (under dark condition) of six solar cells whose emitters were formed under different conditions.

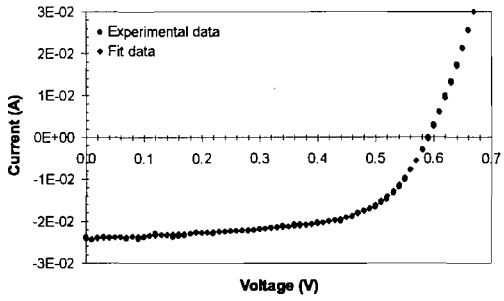

(a) C1 (5 minute 1000 °C)

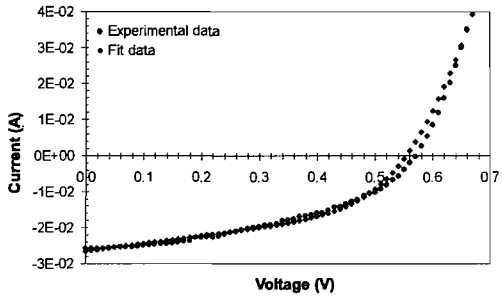

(b) C2 (10 minute 1000 °C)

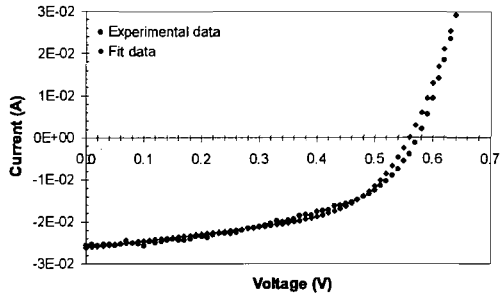

(c) C3 (15 minute 1000 °C)

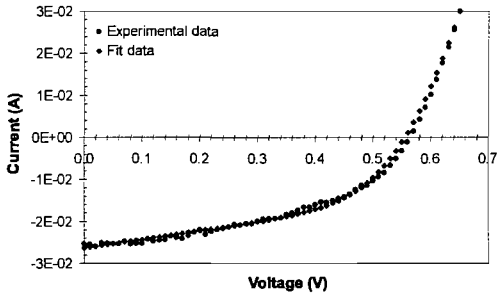

(d) C4 (20 minute 1000 °C)

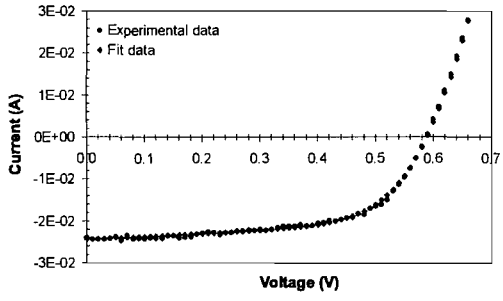

(e) C5 (25 minute 1000 °C)

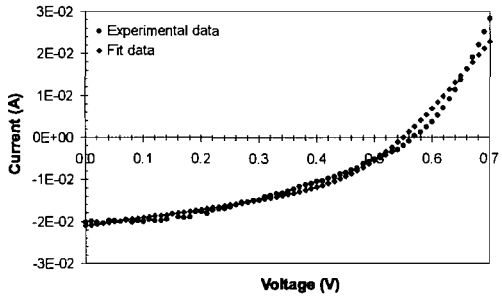

(f) C6 (30 minute 1000 °C)

FIGURE 3.11: I-V Characteristics (under light condition) of six solar cells whose emitters were formed under different conditions.

3.3.3 Spectral Response Measurements

In order to gain a deeper insight into the performance of the fabricated cells, the spectral responses were measured using the T.S. Space System Solar Simulator. The measurement setup is shown in Fig. 3.12. A Xenon lamp generates a white light passing through a filter wheel, which contains several bandpass filters (10 nm bandwidth) covering the range of 450-1100 nm in an interval of 50 nm. The HP4142B was programmed to apply a zero voltage to the device under test and recorded current (I_{sc}) continuously. The average short circuit currents, recorded by sampling continuously 100 points for each wavelength region, were used to determine the spectral response and quantum efficiencies. Under the same experimental conditions, the short circuit current of a reference sample was measured. Using this data and the measured data provided by NREL, the spectral response of the test devices can be determined using the relation [53]

$$SR^t_\lambda = \frac{J^t_{sc,\lambda}}{J^r_{sc,\lambda}} SR^r_\lambda \tag{3.2}$$

where SR^t_λ is the spectral response of the test device at wavelength $d\lambda$,
SR^r_λ is the spectral response of the reference device at wavelength $d\lambda$,
$J^t_{sc,\lambda}$ is the short circuit current density of the test device at wavelength $d\lambda$ and
$J^r_{sc,\lambda}$ is the short circuit current density of the reference device at wavelength $d\lambda$.

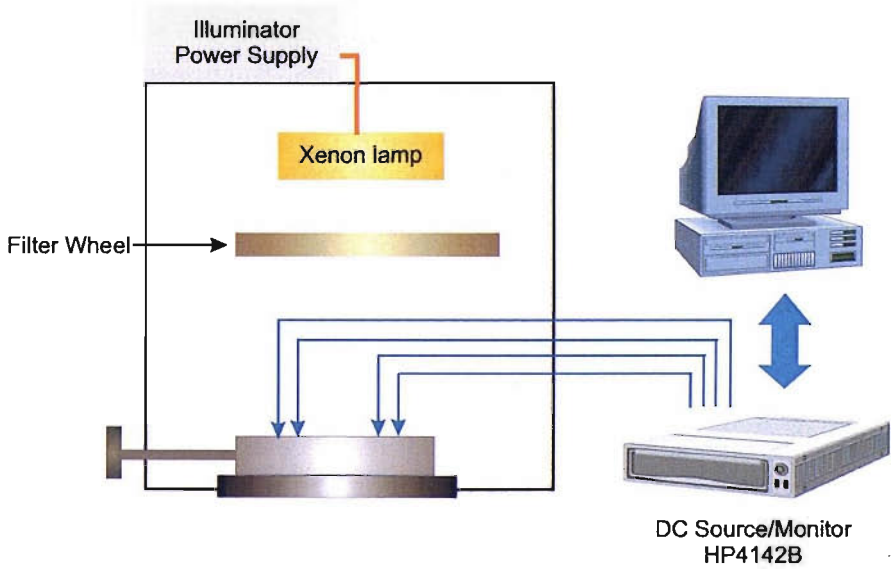

FIGURE 3.12: Spectral response measurement system.

Figure 3.13 shows the quantum efficiency of the solar cells whose emitters were formed under different diffusion conditions. For comparison, the quantum efficiency of a high efficiency c-Si solar cell (22%) fabricated by a The Fraunhofer Institute for Solar Energy Systems ISE is also presented[5]. The curves were normalised such that the maximum peak positions are equal to unity. It was found that the devices fabricated for the present study had low quantum efficiency both in the short wavelength region and long wavelength region. The low quantum efficiency of the cells in the blue region is possibly because the doping concentration of the emitter is very high and there exists a 'dead layer' close to the front surface (see Fig. 3.5). The performance of the cell, thus, degrades with heavy doping effects.

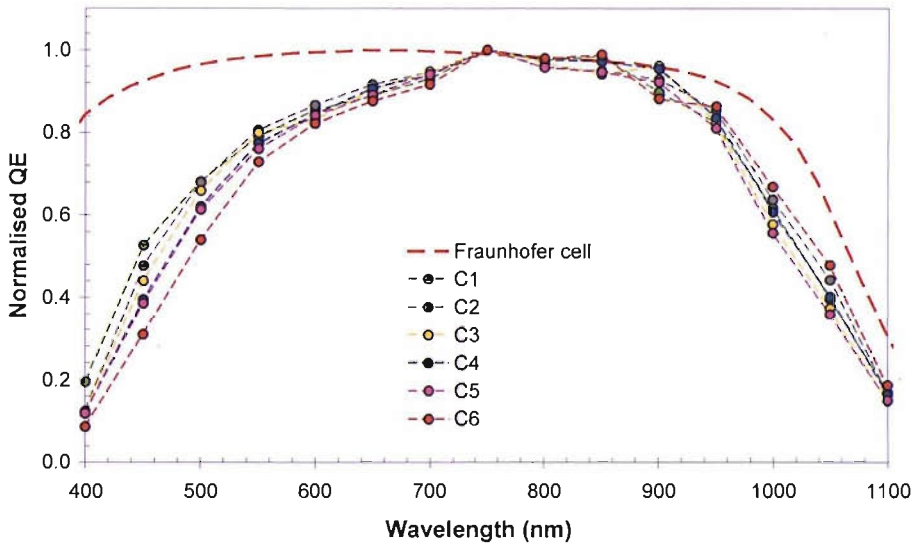

FIGURE 3.13: Quantum efficiency of solar cells fabricated at SUMC and Fraunhofer ISE. The C1 to C6 refers to the SUMC cells whose emitters were formed under different conditions. Sample C1: 5 minutes 1000 °C, sample C2: 10 minutes 1000 °C, sample C3: 15 minutes 1000 °C, sample C4: 20 minutes 1000 °C, sample C5: 25 minutes 1000 °C, sample C6: 30 minutes 1000 °C.

The low quantum efficiency of the solar cells in the longer wavelength region is probably due to the back surfaces of the devices not being passivated. Though the BSF was incorporated into the structure, the recombination velocity of carriers near the back surface may be still high, hence, resulting in the lower quantum efficiency. The quantum efficiency of the solar cell from separate parts of each region will be modelled and discussed in more detail in Chapter 4.

[5]The quantum efficiency of Fraunhofer cell was courtesy provided by Dr. Wilhelm Warta Fraunhofer Institute for Solar Energy Systems ISE.

Considering the curves in detail, it was found that the spectral response of the cells in the short wavelength region (~400-550 nm) was gradually increased with decreasing diffusion time. This is because the junctions of the devices were formed closer to the front surface, where the generation rate of carriers is highest.

3.3.4 Optical Reflectance Measurements

It is known from the previous section that the fabricated devices possess low electrical performance compared to the theoretical limits. One of the reasons is the reflection loss at the front surface. Thus, the aim of this section is to investigate the optical properties of the fabricated devices in particular the reflectance at the front surface.

In this study, the reflectance of a sample was measured using an integrating sphere measurement system. The measurement was performed as a courtesy by Vichai Maneemongkolkiat, School of Electrical and Computer Engineering, Georgia Institute of Technology. The system uses an integrating sphere[6] to measure the total (diffuse and specular) reflectance [54]. The general experiment setup for the measurement is shown in Fig. 3.14. A spectrophotometer is used to produce a monochromatic light for the integrating sphere. The light is guided to the entrance port of the integrating sphere and is focused upon the sample. The incident flux is reflected by the sample and undergoes multiple reflections inside the sphere. The total hemispherical reflectance, both the diffuse and specular components, is collected by a photodetector.

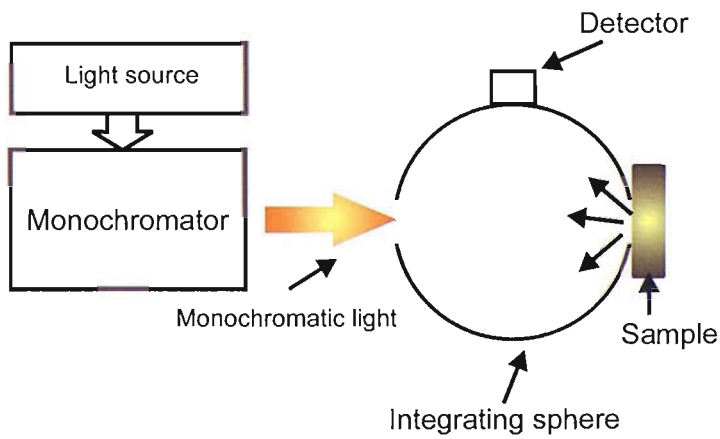

FIGURE 3.14: Schematic diagram of reflectance measurement using integrating sphere.

[6]Integrating sphere is an optical device whose inner surface is coated with a diffusely reflecting material.

Figure 3.15 shows the results obtained from the measurement. As expected, a reflectance peak is observed at a wavelength of approximately 370 nm corresponding to strong direct absorption of silicon[7]. The reflectances gradually decrease with increasing wavelength to values approximately 33%. However, at a wavelength value of approximately 1000 nm, the measured reflectance begins to rise up to a maximum of approximately 60%. The reasons for the enhancement in reflectance at longer wavelengths are due to:

1. the very low absorbing capabilities of the silicon and
2. the total internal reflections due to the presence of a back reflector.

Compare this result with the modelled reflectance of bare silicon discussed in section 3.1.2 (see Fig. 3.2), we found that the reflectance obtained from this study is lower. This expected feature implies that the thin layer of the SiO_2 (100 nm) coated on the front surface of the cell can reduce the reflection loss. However, comparing this plot to the modelled result of 100 nm thick SiO_2 coated Si, it is seen that the plots do not very well agree. The reflectance obtained in this study was higher. The disagreement in the visible region is probably due to the thickness of SiO_2 having deviated from 100 nm.

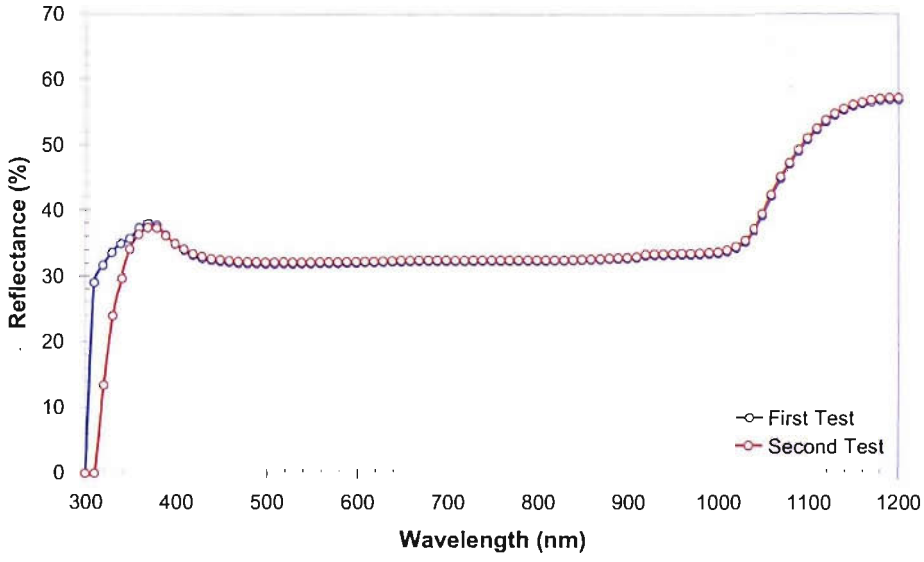

FIGURE 3.15: Reflectance of a c-Si solar cell obtained from integrating sphere.

To validate the assumption, the thickness of SiO_2 was measured by ellipsometry. Ellipsometry is a non-destructive optical technique which allows to study the optical properties of materials or the thickness of thin films. The main effect taking place is

[7]At this point the refractive index of the silicon is highest (see Fig. 2.10) and has its value of approximately 6.9.

the reflection of linearly polarized light at a surface. By measuring the changes in the polarisation state of the reflected light, we obtain information related to the physical properties of the layer. The relationship is nonlinear and, therefore, a numerical method is used to determine the optical properties and the thickness of the film from ellipsometric data [55].

In this study, a UVISEL spectroscopic phase modulated ellipsometer from Jobin-Yvon was used to measure the thickness of SiO_2 layer. A schematic diagram of the system is illustrated in the Fig. 3.16. The collimated light from an arc lamp is passed through a linear polariser and photoelastic modulator (PEM) to produce light of known controlled polarisation. This light interacts with the system under study and its polarisation is modified. The modified state of polarisation at the output of the system is respectively passed through an analyser, monochromator and photomultiplier (PMT) detector for further analysis. The thickness of the SiO_2 was found to be approximately 48 nm.

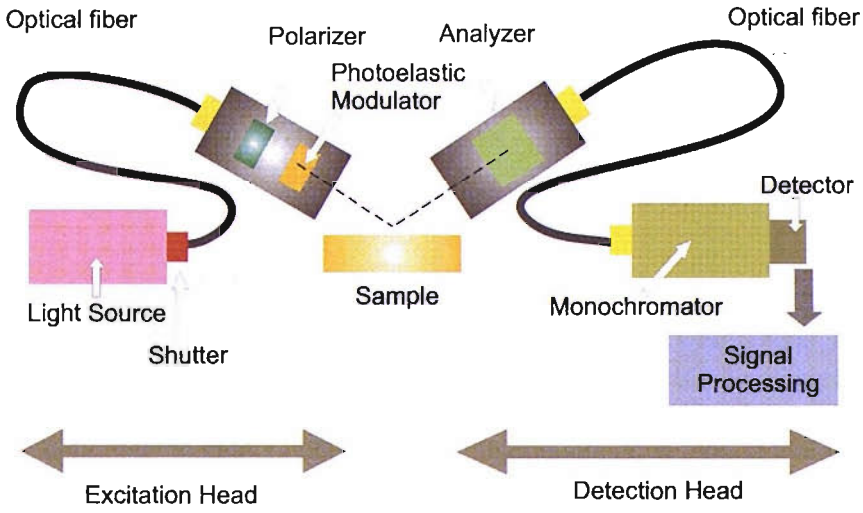

FIGURE 3.16: Schematic diagram of UVISEL spectroscopic phase modulated ellipsometer from Jobin-Yvon.

Although, this result confirms the assumption which was made previously, it is surprising to know that the thickness of the SiO_2 is reduced to approximately half of the oxide deposited on the front surface. Based on the detailed analysis of the designed processes, it is found that the reduction of the oxide thickness is probably due to partial etching away of the oxide during the pre-metallisation process.

Another important feature, which was noticed when compared the experimental reflectance with the theoretical curve, is the disagreement of the data near the infrared region. The disagreement can be readily explained by the fact that the optical model used to obtain the reflectance in section 3.1.2 does not include the internal reflection

due to the presence of a back reflector. To include this effect, the optical model has been extended. In the consideration, the cell surfaces are assumed completely flat and no randomisation is considered. The schematic diagram which includes the optical path of rays is illustrated in Fig. 3.17. Light incident onto the cell is partially reflected at front surface with reflectance R_{fe}. The rays pass into the device and are partially absorbed within the material. The unabsorbed rays are reflected at the back surface of the device which has its reflectance equal to R_b and hence are re-directed towards the cell front surface. As a result of this, light which is not absorbed during the first passage through the cell will have additional opportunities for absorption. The reflected rays, generally the light with wavelength in the near infrared region, are absorbed weakly inside the cell. Thus, they will reach the internal front surface whose reflectance is equal to R_{fi}. These rays, again, can be reflected and undergo similarity mechanisms. The reflectance R which includes the possibility of internal reflections within the device is given by [56]

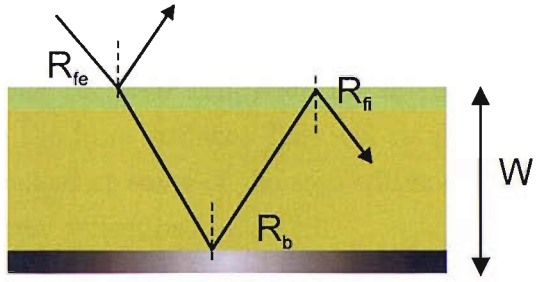

FIGURE 3.17: The schematic diagram of a solar cell with total thickness of W. The optical path of rays illustrate the reflection of light at the front surface with reflectance R_{fe}, the reflection of light at the back surface with reflectance R_b and the reflection of light at the internal front surface with reflectance R_{fi}.

$$R = \frac{R_b(1 - R_{fe})(1 - R_{fi})e^{-2\alpha W}}{1 - R_b R_{fi} e^{-2\alpha W}} + R_{fe} \tag{3.3}$$

where R_{fe} is the external front surface reflectance,

R_{fi} is the internal front surface reflectance,

R_b is the reflectance at the back surface of the device and

W is the thickness of the cell.

Figure 3.18 compares the experimental reflectance and modelled reflectance obtained from Eq. 3.3. It was found that a better fit to the data near the silicon bandgap could only be achieved using different values of external and internal front surface reflectance. This can easily be explained in terms of small variations in the orientation

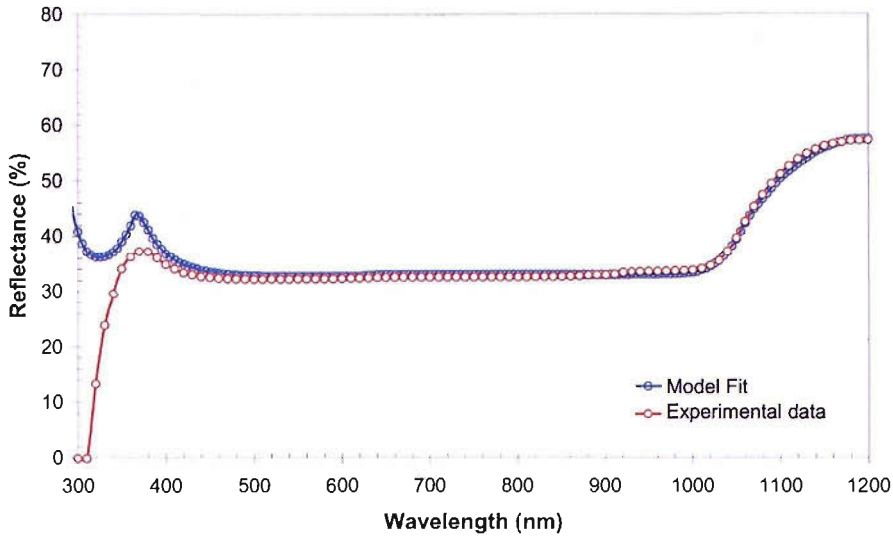

FIGURE 3.18: The reflectance spectrum from experimental and modelled results. The parameters R_b, R_{fe} in Eq. 3.3 are adjusted to achieve a least squares fit to the experimental data. A model result is well fitted with the experimental result when $R_b = 0.75$ and $R_{fi} = 0.69$

of the back contact along the solar cell, resulting in small variations in the angle of internal incidence onto the front surface. This will result in a marked increase in the internal reflection coefficient as some of the rays will now fall outside the escape cone and undergo total internal reflection.

3.4 Conclusions

c-Si solar cells with $n^+/p/p^+$ structure were successfully designed and fabricated at Southampton University Microelectronics Center. Special attention was paid to the emitter layer because it is the major part that can absorb a large fraction of sunlight. Six different runs were carried out by varying diffusion conditions to prepare the emitter layers with different doping profiles and also junction depths. The 100 nm thick SiO_2 layer was used as an AR coating for the design. This is because it can provide lowest reflection loss at the wavelength of approximately 600 nm, which is the region where the intensity of the solar spectrum is maximum.

The doping profiles of the emitters were characterised using Secondary Ion Mass Spectrometry and Spreading Resistance Profiling techniques. The SIMS study revealed the presence of a heavily doped region or 'dead layer' near the front surface of the device. The SPR results indicated that the junction depth of the devices whose emitters were

formed at 1000 °C for 5 minutes and 1000 °C for 30 minutes, were in the range of 0.96 μm and 1.32 μm, respectively.

The electrical performance of the devices were characterised through the I-V curves and spectral response curves. The optical performance were also characterised by using integrating sphere measurement system and also ellipsometry. The I-V results revealed that the fabricated cells have poor electrical characteristics. This is due to the devices have high series resistances R_s, low shunt resistances R_{sh} and also high leakage currents I_0. The high R_s arises from the resistance of the cell materials and also from the contacts. The low R_{sh} of the cells are mainly caused by the leakage current through the cell and around the edges of the devices. The high values of I_0 are due to the high recombination of the minority carriers within the cells which may be due to lattice defects, poor quality of surface passivation and low minority carrier lifetimes.

The measurement of the spectral response indicated that the devices have low quantum efficiency both in the short wavelength and long wavelength region. The main factor which reduces the efficiency of the cells in the blue region is the heavy doping of Phosphorous dopant at the front surface of the cells. The low quantum efficiency of the solar cells in the longer wavelength region is probably due to the back surfaces of the devices not being passivated.

The reflectance at the front surface of the device was approximately 33% within the range 400-1000 nm. At a wavelength value of approximately 1000 nm the measured reflectance begins to rise again up to the maximum of approximately 60%. This enhancement is because the absorbing capability of the silicon is very low in this region and light can be totally internal reflected due to the presence of a back reflector.

The thickness of the SiO_2, which is used as the AR coating, was also measured using ellipsometry. The result indicated that the thickness of the SiO_2 is approximately 48 nm. The thickness is reduced to approximately half of the oxide deposited on the front surface. Analysis of the designed processes in detail, it is found that this reduction of the oxide thickness is probably due to partial etching away of the oxide during the pre-metallisation process.

From the results obtained from this study, it is obvious that further work is needed in order to develop the c-Si devices with better performance. The diffusion process should be modified to obtain a proper doping profile within the emitter, i.e., without the kink and excess Phosphorus region. The thickness of SiO_2 layer deposited on the

front surface should be increased to take into account of the partial etching away of the oxide during the pre-metallisation process.

Chapter 4

Modelling and Analysis of Solar Cell Performance

The analysis of solar cells in terms of material and microscopic device parameters is the key to realise the solar cell performance and efficiency. The cell performance can be evaluated using two measurement techniques: the I-V curve and the spectral response. The I-V characteristic gives the fundamental parameters of the cell, i.e., short circuit current, open circuit voltage, fill factor and the cell efficiency. It also gives information regarding the losses due to the internal resistances such as shunt and series resistances. On the other hand, the spectral response provides information on the physical properties of the solar cell. It indicates how the cell respond to the incoming photon flux in each device region. The spectral response also contains the information related to the quality of the solar cells.

The spectral response or equivalently, the quantum efficiency is typically presented as a function of wavelength. However, Sinkkonen et.al [57] and Donolato [58] discussed an alternative approach by considering the quantum efficiency as a function of the absorption coefficient or distance (Eq. 4.1). This approach can provide important parameters of solar cells; for instance, diffusion length, junction depth, surface recombination velocity, etc.

According to Eq. 4.1, it is seen that a monochromatic light incident onto an infinitely thick cell is absorbed and attenuated by a factor of $\exp(-\alpha(\lambda)x)$. The response of the cell at any x position is related to the collection efficiency of charge carriers $\eta_c(x)$. To obtain the quantum efficiency of the device, the collection efficiency is needed.

$$IQE(\alpha) = \alpha \int_0^\infty exp(-\alpha x)\eta_c(x)dx \tag{4.1}$$

In this chapter, we developed a method to determine the collection efficiencies of minority carriers within emitter and base [56]. The results were used to obtain the IQE of the device. The IQE was fitted to the experimental data obtained from the previous chapter, providing the internal parameters of the fabricated solar cell. Such information can be used to evaluate the quality of the cell regarding to the fabrication process.

4.1 Theoretical Model

The collection efficiency of minority carriers within a non–uniform emitter can be calculated from the transport equations (Eqs. 2.2 and 2.4). To simplify the analysis, we considered charge carrier transport in only one direction along the x axis. In addition, the low-level injection assumption was employed in the analysis. Equations 2.2 and 2.4 can be expressed in the simple forms as

$$J_p = q\mu_p pE - qD_p\frac{dp}{dx} \tag{4.2}$$

$$\frac{1}{q}\frac{dJ_p}{dx} = G - \frac{1}{\tau_p}(p - p_0) \tag{4.3}$$

A more convenient form of Eqs. 4.2 and 4.3 can be obtained by introducing the normalised excess minority-carrier concentration $u(x)$ [59]

$$u(x) = \frac{p(x) - p_0(x)}{p_0(x)} \tag{4.4}$$

The transport equation for the minority carriers in the dark ($G = 0$) can then be written as

$$-\frac{d}{dx}[D_p p_0 \frac{du}{dx}] + \frac{D_p p_0}{L_p^2}u = 0 \tag{4.5}$$

where D_p is the hole diffusion coefficient

$$D_p = \frac{kT}{q}\mu_p \tag{4.6}$$

L_p is the diffusion length

$$L_p = \sqrt{D_p \tau_p} \tag{4.7}$$

and τ_p is the hole lifetime.

Before discussing the methodology used to derive the solution of Eq. 4.5, it is essential to refer to the reciprocity theorem proposed by Markvart [60]. The theorem states that the collection efficiency η_c is the solution of Eq. 4.5 when the boundary condition at the junction edge is $\eta_c = 1$ and at the surface is

$$qDp_0 \frac{d\eta_c}{dx} = -J_{0S}\eta_c \tag{4.8}$$

where $J_{0S} = qSp_0$ and S is the surface recombination velocity (SRV).

In this calculation, the parameter $p_0(x)$ was modified to take account of band gap narrowing [59]:

$$p_0(x) = \frac{n_{ie}^2}{N_D} = \frac{n_{i0}^2}{N_{Deff}} \tag{4.9}$$

where n_{ie} and n_{i0} are the intrinsic carrier concentration and effective intrinsic concentration, respectively

$$n_{ie}^2(x) = n_{i0}^2 exp(\frac{\Delta E_g}{kT}) \tag{4.10}$$

N_D and N_{Deff} are the doping concentration and effective doping concentration and ΔE_g is the apparent bandgap narrowing [61]

$$\Delta E_g = 14 \times 10^{-3} \times \left[ln \left(\frac{N_D}{1.4 \times 10^{17}} \right) \right]. \tag{4.11}$$

The Auger recombination, which occurs at high doping densities, is included through an appropriate term in the minority-carrier lifetime [61].

$$\tau_p = [50 + (2 \times 10^{-13} \times N_D) + (2.2 \times 10^{-31} \times N_D^2)]^{-1} \tag{4.12}$$

The dependence of mobility on electric field is given as [61]

$$\mu_p = 155 + \frac{315}{1 + (N_D/10^{17})^{0.9}} \tag{4.13}$$

The determination of u or η_c for the emitter must, in general, be carried out by numerical quadrature on account of the non–uniform doping and heavy doping effects. To separate the effect of surface from bulk recombination, it is convenient to follow del Alamo and Swanson [59] and define the 'forward' and 'reverse' solutions u_f and u_r of Eq. 4.5 with the following boundary conditions:

$$\begin{aligned} u_f(0) &= 0; \qquad & u_f(W_e) &= 1 \\ u_r(0) &= 1; \qquad & u_r(W_e) &= 0 \end{aligned} \tag{4.14}$$

where $x = 0$ and $x = W_e$ corresponding to the surface of the emitter and the junction edge, respectively.

The general solution can be expressed as

$$u(x) = u_f(W)u_f(x) + u_r(0)u_r(x) \tag{4.15}$$

The collection efficiency in the emitter, which satisfies the correct boundary conditions, is given by Eq. 4.16.

$$\eta_c(x)(Emitter) = u_f(x) + \frac{\alpha_r J_{0r}}{J_{0r} + J_{0Se}} u_r(x) \tag{4.16}$$

where J_{0Se} refers to surface saturation current density

$$J_{0Se} = \frac{q n_{i0}^2 S_e}{N_{Deff}(W)} \tag{4.17}$$

$$J_{0r} = qD_p p_0 \frac{du_r}{dx}|_{x=0} \qquad \alpha_r J_{0r} = qD_p p_0 \frac{du_r}{dx}|_{x=W} \tag{4.18}$$

S_e is the surface recombination velocity at the front surface and α_r is the probability of the carrier injected at one edge of the region reaching the other end without recombination.

For the p–type base region, the determination of the collection efficiency $\eta_c(x)$(Base) can be obtained analytically because the doping concentration within the base region is assumed to be uniform. The presence of the back surface field can be allowed for the value of the surface recombination velocity S_b at the back surface. Thus the collection efficiency equation becomes:

$$\eta_c(x)(Base) = cosh(x/L_n) - \frac{tanh(W_b/L_n) + S_bL_n/D_n}{1 + (S_bL_n/D_n)tanh(W_b/L_n)} sinh(x/L_n) \tag{4.19}$$

where W_b is the base width, x is the distance measured from the junction edge and the subscripts of L_n and D_n refer to the appropriate quantities for electrons in the p–type base. In the present analysis, the EQE was determined from

$$EQE = \int_0^W \eta_c(x)g(x)dx \tag{4.20}$$

where $\eta_c(x)$ are the collection efficiencies of minority carriers in the emitter, base and depletion regions. Note that the collection efficiency within the depletion region was assumed to be unity.
$g(x)$ is the generation function

$$g(x) = \frac{\alpha T}{1 - R_bR_{fi}e^{-2\alpha W}} \left\{e^{-\alpha x} + R_be^{-2\alpha W}e^{\alpha x}\right\} \tag{4.21}$$

where R_{fe} is the external front surface reflectance,
R_{fi} is the internal front surface reflectance,
R_b is the reflectance at the back surface of the device,
W is the thickness of the cell and
α is the absorption coefficient of silicon.

The IQE of the device was determined from Eq. 2.53 (see Chapter 2). The EQE was derived from Eq. 4.20. The reflectance R, which includes the possibility of internal reflections within the device, was obtained from Eq. 3.3.

4.2 Modelling Procedures

The procedures to model the quantum efficiency of a solar cell can be summarised in the form of a diagram as shown in Fig. 4.1. The first stage of the calculation is to compute the collection efficiency: η_c(Base) and η_c(Emitter). These parameters and the η_c(Depletion) are used to calculate the EQE using Eq. 4.20. The EQE is then used to determine the IQE using Eq. 2.53.

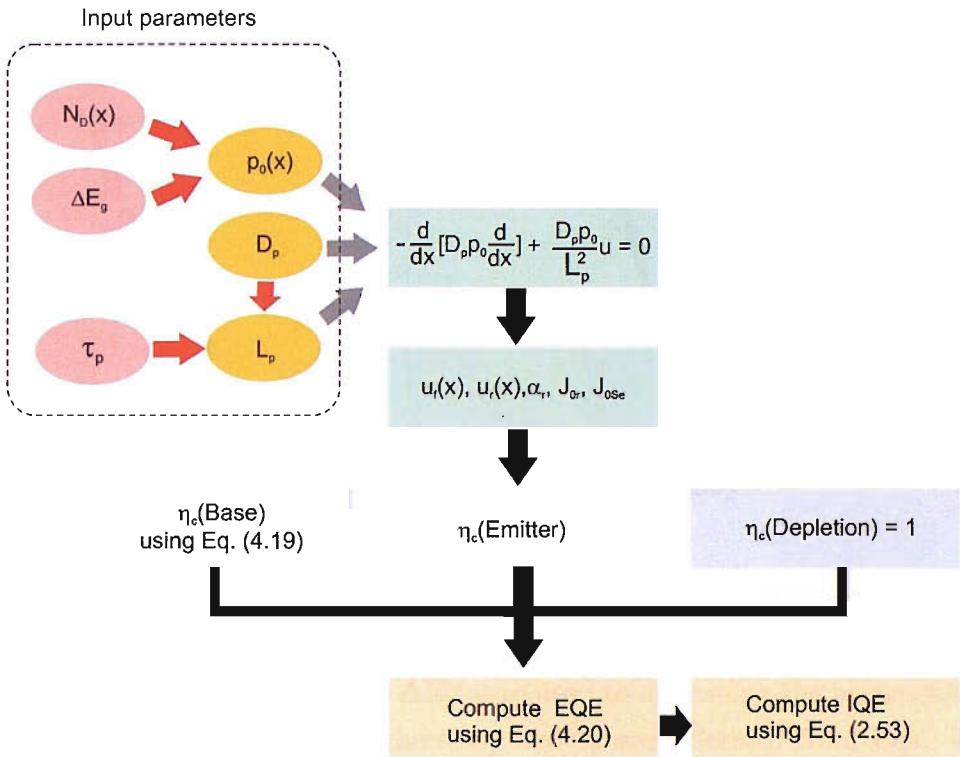

FIGURE 4.1: A schematic diagram of procedures to model the quantum efficiency of a solar cell. The emitter doping profile $N_D(x)$ and bandgap narrowing ΔE_g are used to determine $p_0(x)$. The hole diffusion length L_p are derived from the parameters τ_p and D_p. These parameters are input into transport equation. The equation is solved numerically to obtain the parameters $u_f(x)$, $u_r(x)$, α_r, J_{0r}, J_{0Se} and collection efficiency of emitter η_c(Emitter). The collection efficiency η_c(Base) is determinied from Eq. 4.19. The η_c(Base), η_c(Emitter) and η_c(Depletion) are used to obtain external quantum efficiency EQE using Eq. 4.20. The IQE is obtained from EQE using Eq. 2.53

To determine η_c(Emitter), the emitter doping profile (N_D) is needed for the calculation. The profile was obtained by fitting a polynomial equation to the SRP data obtained in section 3.3.1. The goodness of the fit profile was justified by comparing the polynomial profile with the data points and considering the square of the correlation coefficient

R^2 of the point being fitted. The doping profile obtained from the fitting and the experimental profile were plotted together as shown in Figure 4.2. The result shows a good agreement of both profiles with $R^2 > 0.99$. Thus, the polynomial function obtained from this process was considered to be a representative of the experimental SRP profile.

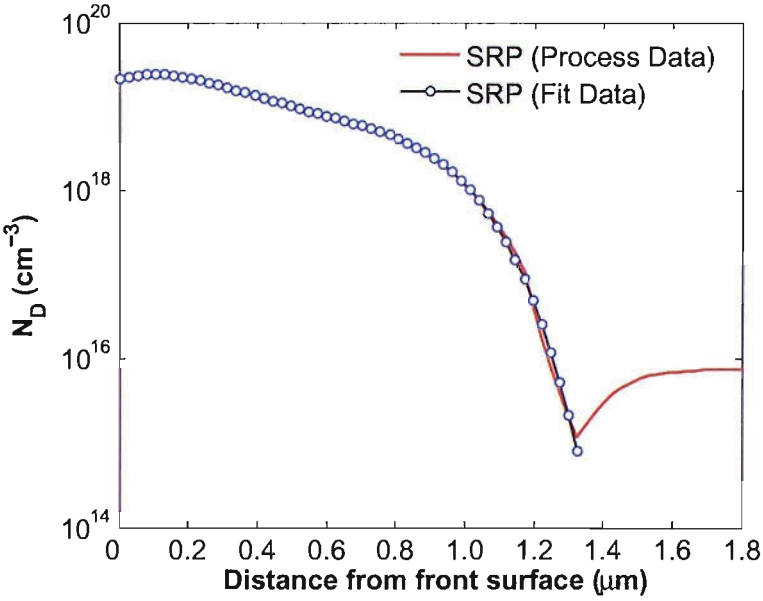

FIGURE 4.2: Doping profiles obtained from SRP measurement and polynomial fit.

The doping profile function and the ΔE_g were used to determine the parameter $p_0(x)$. L_p was computed from Eq. 4.7, where D_p and τ_p were derived from Eqs. 4.6 and 4.12. The parameters p_0(x), L_p and D_p were used as the input for Eq. 4.5. The equation was solved numerically using a MATLAB program (Ver 7.0.1). The parameters $u_f(x)$, $u_r(x)$, α_r, J_{0r} and J_{0Se} obtained from the computation, were used to compute the collection efficiency of minority carriers within the emitter using Eq. 4.16. The collection efficiency of minority carriers within the base region was computed from Eq. 4.19. The collection efficiencies obtained from the calculations were used to determine the EQE from Eq. 4.20 and IQE from Eq. 2.53. The IQE obtained from the model from each region of the cell was fitted with the experimental data to extract important parameters of the device, for example, front and back surface recombination velocities, minority carrier diffusion lengths and a junction depth.

4.3 Results and Discussions

Figure 4.3 shows the modelled result which presents the collection efficiency within the emitter as a function of the distance from the front surface and the surface recombination velocity. The plot indicates that the collection efficiency increases towards the junction boundary and has a value close to unity at the junction edge. The plot also suggests that the collection efficiency depends strongly on the surface recombination velocity (SRV) at the front surface. The collection efficiency drops dramatically as the SRV becomes higher than 10^3 cm/s.

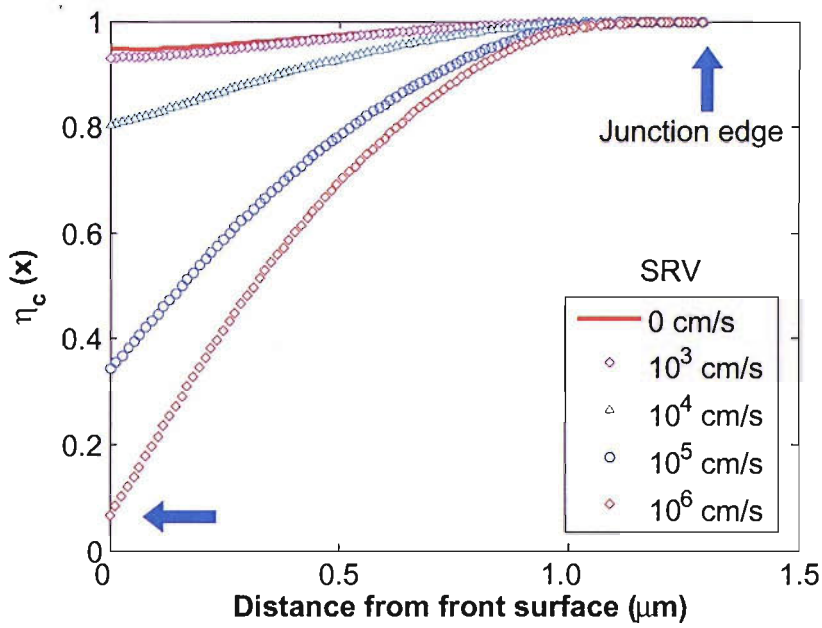

FIGURE 4.3: The minority carrier collection efficiency within the emitter, calculated from the SRP profile for different surface recombination velocity (SRV). The arrow indicates the curve for $S = 10^6$ cm/s as used for the curve fitting for the present solar cell.

The doping concentration in the base region was assumed to be uniform and from the SRP data presented in Fig. 4.2, it is equal to 8×10^{15} cm^{-3}. The collection efficiency calculated from Eq. 4.19 for different values of the surface recombination velocity S_b is shown in Fig. 4.4. As can be seen from the plot, the collection efficiency increases towards the junction boundary and it reaches the highest value at the junction edge. The collection efficiency at the back surface decreases from 0.63 to 0.33 as the S_b increases from 0 to 10^3 cm/s.

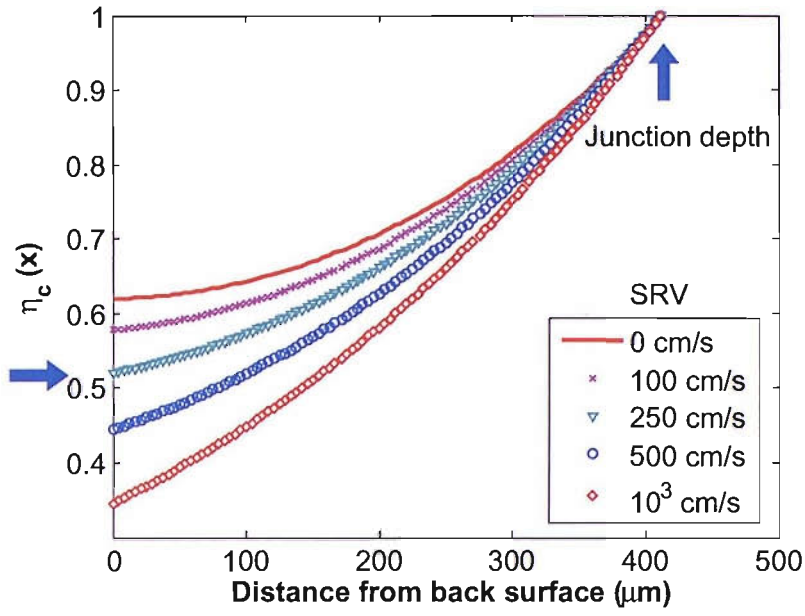

FIGURE 4.4: The minority carrier collection efficiency within the base. ($L = 396$ μm) calculated for different surface recombination velocity (SRV). The arrow indicates the curve for $S = 250$ cm/s as used for the curve fitting for the present solar cell.

Figure 4.5 shows a comparison of the experimental IQE (tested by NREL under AM1.5-G condition at an ambient temperature of 25 °C) with the results calculated in the present model and PC1D (Ver. 5.3). The cell parameters summarised in table 4.1 were chosen for the simulation for the present model and PC1D. The results obtained from the present model are in good agreement with the simulated result obtained from PC1D. A slight disagreement is probably due to the differences in the optical models. The model developed in this work takes into account internal reflection but does not allow for light trapping effects which are included in PC1D [62]. Unlike PC1D, the procedure discussed in this work makes it possible to separate contributions not only from indicated regions of the cell, but also from the separate parts of each region through the collection efficiency. The fitted parameters also suggested that the device has a high front surface recombination velocity and low back surface recombination velocity. These results revealed that the technological process for passivating the front layer still need to be further developed in order to enhance the collection efficiency from the emitter. The BSF structure effectively minimises the surface recombination velocity at the back surface of the devices.

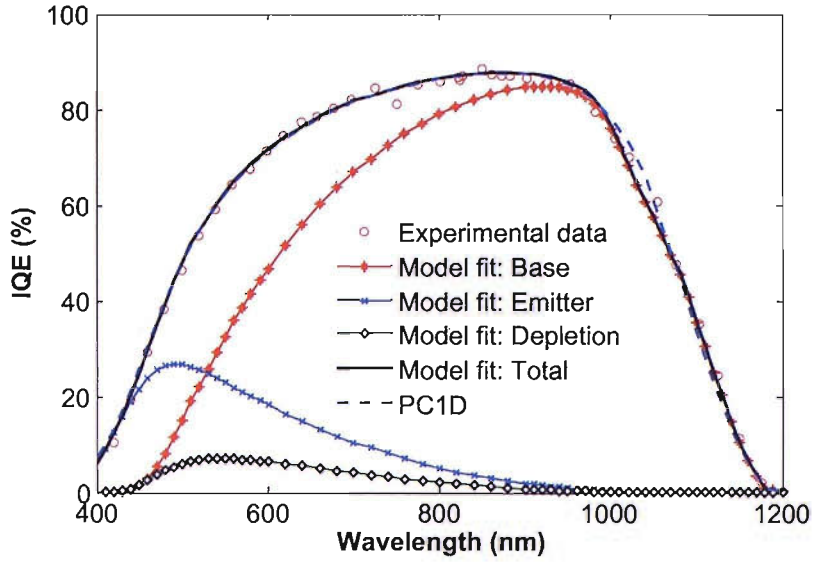

FIGURE 4.5: Comparison of internal quantum efficiency obtained from the model, PC1D and experimental data.

TABLE 4.1: The cell parameters chosen for the simulations

Parameters	Value	Unit
Emitter surface concentration	2×10^{19}	cm^{-3}
Base doping concentration	8×10^{15}	cm^{-3}
Junction depth	1.35	μm
Front SRV	10^6	cm/s
Back SRV	250	cm/s
Electron diffusion length	747	μm
R_b	75	%
R_{fi}	69	%

4.4 Conclusions

The performance of the p–n junction solar cell was investigated in terms of collection efficiency in each region. The collection efficiency of the emitter was derived by considering the diffusion equation for minority carriers and a reciprocity relationship of the charge collection and the dark carrier distribution. The collection efficiency of the base was derived analytically.

The internal quantum efficiency obtained from the model was fitted with the experimental data in order to extract important cell parameters. These parameters include front and back surface recombination velocities, the minority carrier diffusion lengths and the junction depth.

The fitted results revealed that the good response from the base region is due to an adequate diffusion length and a very good back surface field which leads to very low effective surface recombination velocity at the back surface. The poor response of the cell at short wavelengths is due to a high front surface recombination velocity. To improve the performance of the devices, a good surface passivation is required.

Part II

Fluorescent Collector

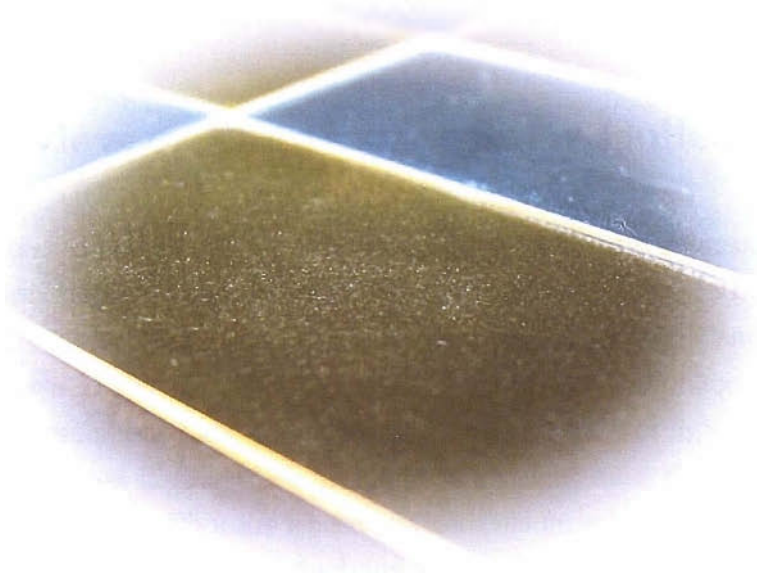

Chapter 5

Introduction to Fluorescent Solar Collectors

The intention of this chapter is to present a review of the literature related to fluorescent solar collectors, providing an overview of the status of the research in this field. The chapter is divided into three sections. Section 5.1 describes the basic concept of the fluorescent solar collector and its principle of operation. Section 5.2 presents a review of early work related to fluorescent solar collectors. Section 5.3 provides some theoretical background related to the emission and propagation of fluorescence within the fluorescent collector.

5.1 Overview of Fluorescent Solar Collectors

A fluorescent solar collector (FSC), also known as a fluorescent solar concentrator, is an optical device that can concentrate diffuse and direct sunlight and convert it into electricity. The conventional design of FSCs consists of a solar cell and a fluorescent collector[1] as shown in Fig. 5.1. Its operation relies on four major mechanisms: light absorption, light emission, light propagation and conversion of light into electricity. The absorption process begins when the light is incident onto the large area of the fluorescent collector (FC). Photons whose wavelengths lie within the absorption band of the fluorescent materials are absorbed and subsequently re-emitted at longer wavelengths. A large fraction of the emitted light is trapped within the FC because the refractive index of the FC is higher than that of the surrounding medium. The trapped

[1]The fluorescent collector is a transparent plastic or glass plate doped with fluorescent materials.

light is then delivered to the edges of the FC via total internal reflection and converted to electricity by a solar cell.

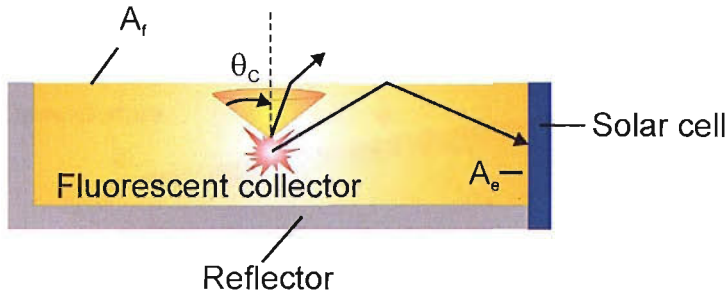

FIGURE 5.1: A cross-sectional view of a fluorescent solar collector. Two rays presented in the figure correspond to light emitted with angle $\theta < \theta_c$ and $\theta > \theta_c$.

The ability to concentrate light by the FSC is defined as the ratio between the front area and the edge area of the FC as given in Eq. 5.1 [63].

$$G = \frac{A_f}{A_e} \tag{5.1}$$

where A_f and A_e are the areas of the front face and the edge of the FC, respectively. G is a factor which indicates the brightness of light at the edge of the FC, generally known as the geometric gain. Assuming that there is no loss inside the FC plate, the light emitted from the edge would be brighter than the collected sunlight by a factor of G. As a result, a solar cell which is coupled to the edge of the FC can attain higher power incident and yield a higher electrical output.

5.2 Review of Fluorescent Solar Collectors

The background of the research in this field can be traced back to around the mid 1970s when Weber and Lambe [10] and Goetzberger and Greubel [11] independently proposed a novel concept of using a luminescent medium together with total internal reflection to concentrate light to high-efficiency solar cells.

The system which was called luminescent solar collector by Weber and Lambe [10] was composed of a planar collector coupled at one edge with a solar cell as shown in Fig. 5.2. Besides this novel concept, the authors also proposed a model to predict the probability that the absorbed photons will be emitted at the edge. This quantity,

which was called collection efficiency by the authors, is given by

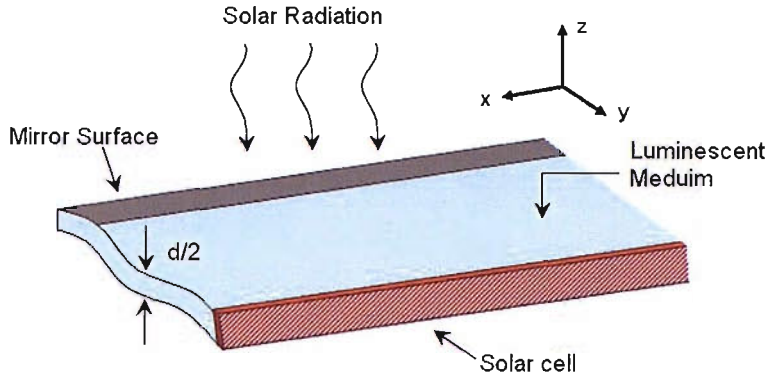

FIGURE 5.2: Schematic of a luminescent solar collector as proposed by Weber and Lambe. The structure was considered to have infinite length in the x direction. A perfectly reflecting mirror was introduced at $y = 0$ and solar cell at $y = L$ [10].

$$Q_{C,Web} = (2\pi L)^{-1} \int_0^L dy \int_0^{\pi} d\phi \int_{\theta_c}^{\pi/2} sin\theta d\theta \left\{ \left[exp\frac{-\alpha_e(L-y)}{sin\theta sin\phi} \right] + exp\left[\frac{-\alpha_e(L+y)}{sin\theta sin\phi} \right] \right\} \times \left\{ 2 - \left| r_s(\theta,\phi)^2 \right| - \left| r_p(\theta,\phi)^2 \right| \right\} \tag{5.2}$$

where $Q_{C,Web}$ is the collection efficiency of the system shown in Fig. 5.2,

θ and ϕ are the spherical polar angles defining the direction of emission,

θ_c is the critical angle for total internal reflection,

α_e is the attenuation coefficient at the emission wavelength,

$r_{s,p}(\theta,\phi)$ is the amplitude of Fresnel reflection.

Note that Eq. 5.2 was derived by assuming that a perfect mirror was used at $y = 0$. The fraction of light emitted into angles $0 < \theta < \theta_c$ and $\pi > \theta > \pi\text{-}\theta_c$, which would be collected at $y = L$, was also neglected.

On the other hand, a fluorescent solar concentrator system proposed by Gotzberger and Greubel [11] is illustrated in Fig. 5.3. A stack of fluorescent collector plates was arranged in such a way that the top plate absorbs the shortest wavelength radiation, whereas the lower plates absorb longer wavelengths.

The advantages of this structure are that

(1) the solar spectrum can be subdivided into different energy fractions and converted by solar cells with different bandgaps and
(2) about half of the radiation emitted within the critical cone can be recovered by the adjacent plates.

The maximum conversion efficiency for stacking four collector plates with four different solar cells, i.e. Si, Ge, GaAs and GaP in series, under AM1 spectrum calculated by the authors was estimated to be 32%.

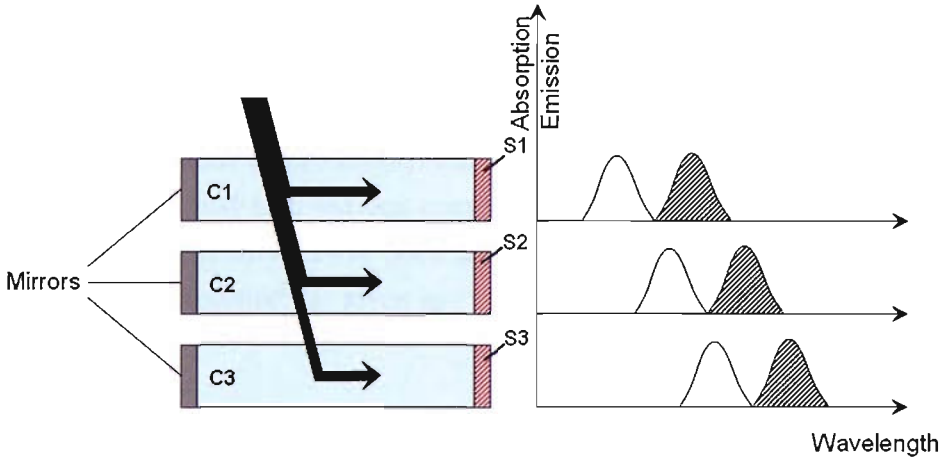

FIGURE 5.3: Schematic of a three-stack fluorescent solar collector. Each collector is coupled to a solar cell whose bandgap matches to the fluorescent wavelengths. The fluorescent collectors are stacked in such a way that the sunlight falls first on material having the largest bandgap. Photons not absorb in the first plate are transmitted to the second and the third plates, which then absorb the remaining portion of photons with lower energy [11].

After the idea was proposed, the research in this field received great attention and the principal operations of FSCs have been investigated experimentally and theoretically.

The very first practical works were those of Levitt *et al.* [64], Swartz *et al.* [65] and Rapp *et al.* [66]. Levitt *et al.* studied the performance of two fluorescent solar collectors that were made of

(1) ED2[2] neodymium-doped laser glass and a silicon solar cell (1.2 mm × 100 mm × 100 mm) and
(2) Rhodamine 6G (Rh6G) doped polymethylmethacrylate (PMMA) and a silicon solar cell (3 mm × 100 mm × 500 mm).

[2]ED2 is a special grade of glass that provides superior refractive properties when compared to standard optical glass. The term ED stands for extra-low dispersion.

The authors observed the photon flux gains from both systems. Under monochromatic illumination, the gains were found to be 5.9 for the glass and 6.3 for the plastic collectors.

Swartz *et al.* [65] reported experimental results based on using a mixture of dyes to enhance the photon flux gain within the fluorescent collector. The donor dyes were used to absorb the solar spectrum and transfer energy to an acceptor dye whose energy of emission can be matched to the maximum efficiency wavelength of the solar cell. The dyes employed for the multiple-dye planar fluorescent collector were Rh6G and Coumarin 6 (Cou6) in PMMA. The absorption efficiency of the multiple-dye system was higher than that of the single-dye system (Rh6G in PMMA) by a factor of 2.

The theoretical model of Weber and Lambe was further developed by Batchelder *et al.* [67] to take into account the re-absorption of fluorescent light. In this treatment, the fluorescence was divided into various components, $Q^{(1)}$, $Q^{(2)}$, $Q^{(3)}$, ... depending on how many times the photons have been absorbed. The fraction $Q^{(1)}$, which is called first generation fluorescence[3], is given as

$$\begin{aligned} Q^{(1)} &= \phi_f (2\pi L)^{-1} \int_0^{\infty} f(\bar{\nu}) d\bar{\nu} \int_0^{L} dy \int_0^{\pi} d\phi \int_{\theta_c}^{\pi/2} \sin(\theta) d\theta \\ &\times \left\{ \exp\left(\frac{[-\alpha(\bar{\nu})(L-y)]}{\sin\theta \sin\phi} \right) + \exp\left(\frac{[-\alpha(\bar{\nu})(L+y)]}{\sin\theta \sin\phi} \right) \right\} \end{aligned} \tag{5.3}$$

Note that the expression is similar to 5.2 except that the dye quantum efficiency ϕ_f and normalised fluorescent spectrum $\int_0^{\infty} f(\bar{\nu}) d\bar{\nu}$ are included in the expression. In addition, the Fresnel reflection term is neglected in Eq. 5.3.

To determine the fraction of fluorescence emitted from higher generations, the authors introduced 2 parameters: R – the average probability that luminescence outside the critical cones will be self-absorbed over a path length L and $\overline{R}$ – the average probability that luminescence inside the critical cones will be self-absorbed. These parameters are related to the n^{th} order generation fluorescence as follows:

$$Q^{(n)} = (1-P)(1-R)[\overline{R}P + (1-P)R]^{n-1} \phi_f^n \tag{5.4}$$

where P is the probability that the emission light will escape out of the surface. It can be computed using Eq. 5.5.

[3]The term 'first generation fluorescence' refers to the fluorescence spectra that are emitted without any re-absorption effect.

$$P = 1 - \cos(\theta_c) = 1 - \sqrt{1 - 1/n^2} \tag{5.5}$$

By summing all $Q^{(n)}$ in geometric series, the total collection efficiency of the system which includes all components from higher generation emissions is given by

$$\begin{aligned} Q_{C,Bat} &= Q^{(1)} + Q^{(2)} + Q^{(3)} + ... \\ &= \frac{\phi_f(1-R)(1-P)}{1-\phi_f[\bar{R}P+R(1-P)]} = \frac{Q^{(1)}}{1-\phi_f[\bar{R}P+R(1-P)]} \end{aligned} \tag{5.6}$$

Besides the model work, Batchelder *et al.* also studied practical aspects of the FSC. The devices were developed from various organic laser dyes [68]. The maximum efficiency of the collector, which is the total electrical power output divided by the total sunlight power incident on the plate, was reported to be 3.2% for a thin-film fluorescent collector plate containing three organic dyes.

Witter *et al.*[69] experimentally tested the idea of a stack fluorescent collector, which was initially proposed by Goetzberger *et al.* [11]. It was reported that the total efficiency of a stack of three sheet fluorescent collectors, which were coupled to Si solar cells, was 2.8%. The authors also reported the further improvement in system performance of the stack structure [70]. By coupling two fluorescent sheets to Si and GaAs cells, the total efficiency of the system reached a maximum of 4%.

Reisfeld and Neuman [71] investigated a practical arrangement of several combinations of organic and inorganic doped glass layers. A system efficiency of about 3.5% to 4.5% was reported for the case of three doped glass layers for CdS, GaAs and Si cells.

In addition to the above attempts, the FSC subject had been researched by various groups [63, 72–74]. However, it is surprising to see that a real improvement of the FSC performance has not yet been obtained or reported. This is mainly due to several problems underlying the development of the FC. These are:

- less absorption of photon flux - only a certain spectrum of sunlight can be absorbed by the dye,
- self-absorption, also known as re-absorption - the re-absorption of the emitted photons due to an overlap of the absorption and emission spectra,
- quenching effect - there is an interaction between two or more fluorescent materials which results in a decrease in the fluorescent intensity,
- escape cone losses - the fluorescence emitted within the critical angle is not

trapped within the collector and

- degradation - the decrease in efficiency of the fluorescent plate due to the instability of the dye after exposure to sunlight.

The above loss processes resulted in the reduction in the FSC performance and subsequently the overall efficiency of the system. For this reason, together with the limitations of dye molecules available during that time, the research in this field had drawn less attention and gained less momentum.

In recent years, the technological development of fluorescent dyes has been significantly improved. Dyes with large stoke shift, high photostability and high quantum yield have become more available, e.g., Lumogen F from BASF company [12] and Alexa Dyes from Molecular Probes Inc. [13]. Some new advanced materials, e.g., quantum dots (QDs) [14] and photonic band-stop filters[4](see Fig. 5.4), e.g., hot mirror[5] [15] and Rugate filter[6] [76] have been introduced to overcome some major loss machanisms. Therefore, the concept of FSC has been stimulated and is gaining increasing attention again.

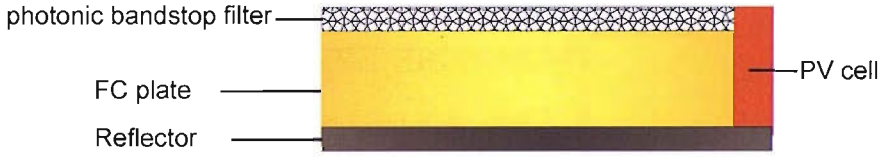

FIGURE 5.4: The low critical cone loss FSC.

To date, several issues ralated to fluorescent solar collectors have been extensively researched. For example, the quantum dot idea has been pursued by the Imperial research group. A theoretical model was also developed to predict the efficiency of their systems [17, 77].

Sloof *et al.* [20] revisited the FSC concept by constructing the fluorescent solar collector based on two different dyes – Macrolex Fluorescence Red G from the Bayer company and S-13[7] from the University of Munich. The current gain was reported to be 1.5.

[4]The photonic band-stop filter is a specialised filter designed to reflect light in the emission range of the dye but transmit the light in the absorption region. Therefore a larger amount of light is trapped inside the collector and guided to the solar cell at the edge.

[5]Hot mirror is a multilayer dielectric mirror that reflects infrared and transmits visible light. It is useful in a variety of applications where heat build-up can damage components or adversely affect spectral characteristics of the illumination source [75].

[6]A Rugate filter is a multilayer reflector with a continuously varying refractive index profile. It can serve as a band reflection filter for the emitted light which leaves the fluorescent concentrator in the loss cone of total internal reflection [76].

[7]S-13 is a fluorescent dye which has a quantum yield of ~100%.

Sheldon *et al.* [22] pursued the concept that was first proposed by Swartz *et al.* [65]. The authors recently showed that the efficiency of the FSC can be enhanced through the use of three organic dyes – BODIPY 494/505, BODIPY 535/558 and BODIPY 564/591, provided by their collaborative partner (Molecular Probes Inc).

Markvart [78] and Rau *et al.* [16] independently developed a theoretical model to predict the efficiency limit of fluorescent collectors. Markvart's analytical model was formulated based on the Shockley-Queisser detailed balance method [32]. Based on the calculation, the maximum efficiency of about 90% would be possible. This efficiency was derived by assuming that the front surface of the collector is covered with a selective reflector that can perfectly prevent the escape of fluorescent light through the front surface. On the contrary, Rau *et al.* [16] analysed fundamental efficiency limits of the FC by using Monte Carlo ray-tracing simulation. The structure under consideration was a collector in which solar cells covered a fraction of its rear surface. The efficiency limits of an FC with and without photonic band-stop (PBS) filter were investigated. The maximum efficiency of the system which included the PBS was reported to be 23.9% when a fraction 10^{-2} of the FC's bottom was covered by solar cells (Fig. 5.5).

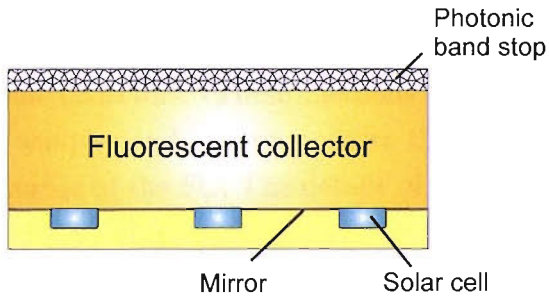

FIGURE 5.5: Schematic drawing of a fluorescent collector with a solar cells at its bottom.

Besides these models, the performance of FCs can also be modelled by employing more advanced computational analysis, such as Monte Carlo simulation [79, 80], or ray tracing technique [21, 81–83]. Although these approaches allow us to model the performance of the FC in a more realistic way, the difficulties of developing algorithms and also lengthy computations are their two major drawbacks that have to be carefully evaluated if these approaches are to be pursued.

A review of available literature suggests that a real breakthrough in efficiency has not yet been achieved. The performance of the FSC is still quite low due to the poor performance of the FC. To understand in detail the underlying problems of the development of the FC, our group has revisited the concept by developing models

and optical characterisation techniques for evaluating the performance of fluorescent collectors.

Two major approaches were pursued during the research. The first approach related to the determination of the re-absorption loss through the fluorescence spectrum measured at the edge of the FC and also the first generation fluorescence spectrum. To our knowledge, the method for obtaining the first generation fluorescence spectrum of the FC plate has never been reported or studied. Therefore, it is interesting to establish a technique that one can use to derive this spectrum and also use it to determine the re-absorption loss. The details of this work can be found in section 8.2.2.

Another approach that was pursued during the research was to develop an analytical model which allows us to consider the re-absorption probability and also the collection efficiency of FC plates (see sections 6.2 and 6.3). Our model is different from the others in that it takes into account

1) the effect of non-ideal reflection at the interface and
2) the effect of non-perfect coupling between the fluorescent collector and the solar cell.

In addition to the above work, we also developed methods for fabricating and characterising the fluorescent collectors. These methods were developed as part of this project to prepare the samples and also to measure the parameters that can be used to evaluate the performance of the FC. The details of these methods can be found in chapter 7.

5.3 Theoretical Background of Fluorescent Solar Collector

This section provides some theoretical background related to the operation of the fluorescent solar collectors. The two major mechanisms that are described in this section are light emission and light propagation. The absorption of light and the conversion of light to electricity were already described in Chapter 2.

5.3.1 Light Emission

The light absorbed by the fluorescent molecules is emitted at longer wavelengths. The emission of photons varies depending on the transition states of the excited molecules.

The emission processes can be simply explained using a Jablonski diagram depicted in Fig. 5.6 [35]. The processes are divided into five steps.

① Photon absorption: The absorption of the photons results in a transition of the molecules from the singlet electronic states S_0 to the first excited states S_1,
② Fluorescence emission: The emission of photons due to the downward transition from S_1 to S_0,
③ Internal conversion: This is the non-radiative process whereby molecules in an excited state may return to the ground state without the emission of a photon, converting all the excitation energy into heat,
④ Intersystem crossing: The molecule changes over from one of the system of singlet states S_1 to triplet state T_1 in which two electron spins are parallel,
⑤ Phosphorescence emission: The transition of the molecules from the triplet electronic states T_1 to the ground electronic state S_0.

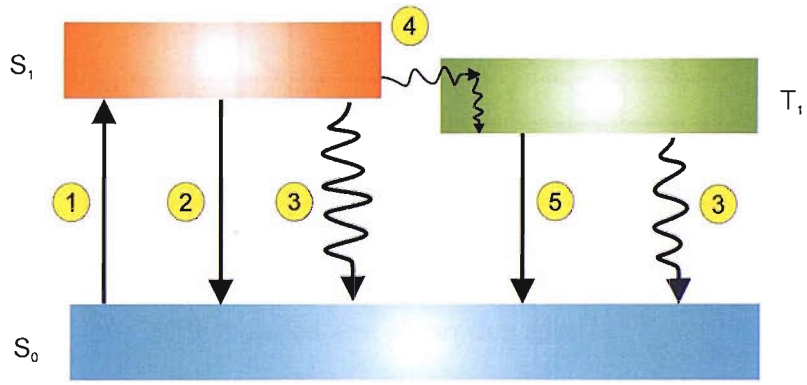

FIGURE 5.6: Jablonski diagram showing the absorption and the emission processes of fluorescence and phosphorescence. The number ①-⑤ are referred to Photon Absorption, Fluorescent Emission, Internal Conversion, Intersystem Crossing and Phosphorescence Emission, respectively.

Figure 5.7 shows an example of the absorption and emission spectra that correspond to the transitions between two electronic states of the molecules S_0 and S_1. The peaks in the spectrum correspond to the vibrational energy levels ($S_{00}..S_{1n}$). The emission spectrum is the mirror image of the absorption spectrum. This situation frequently arises in organic luminescence.

In general, the characteristics of the fluorescent light are influenced by several parameters, including fluorescence quantum yield, Stokes shift, re-absorption mechanism and quenching. Therefore, it is necessary to consider these parameters to gain a better knowledge of the light emission.

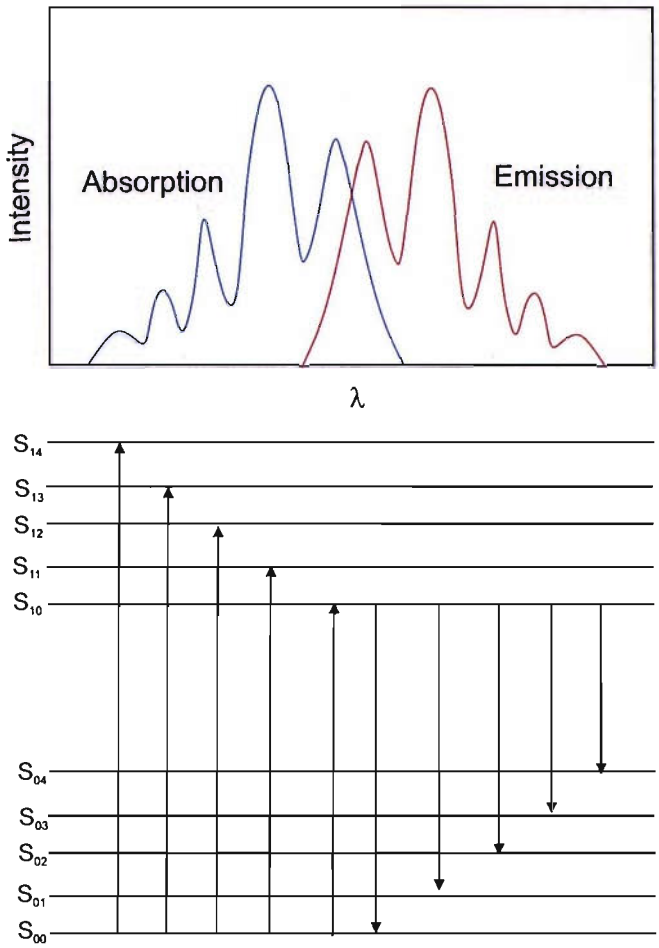

FIGURE 5.7: Vibrational levels of S_1 and S_0 showing origins of vibrational structure in emission and absorption spectra.

5.3.1.1 Fluorescence Quantum Yield

The fluorescence quantum yield ϕ_f is a parameter which gives the efficiency of the fluorescence process. It is defined as the ratio of the number of fluorescence photons emitted N_{ems} to the number of photons absorbed N_{abs}.

$$\phi_f = \frac{N_{ems}}{N_{abs}} \tag{5.7}$$

This parameter is related to the fluorescence intensity per absorbed photon [35], which can be written as

$$\phi_f = \int_0^\infty F(\lambda) d\lambda \tag{5.8}$$

where $F(\lambda)$ is the fluorescence intensity per absorbed photon

$$F(\lambda) = \frac{I_F(\lambda)}{kI_A(\lambda)} \tag{5.9}$$

$I_F(\lambda)$ is the fluorescence intensity,
$I_A(\lambda)$ is the absorbed intensity and
k is a constant factor. It depends on the optical configuration of observation and the setup of the instruments.

The measurement of these three parameters in practice is somewhat difficult as it involves correction for various effects associated with the instruments and experimental setup. Therefore, to determine the quantum yield, a comparative method is commonly employed in practice.

In the comparative method, the fluorescence quantum yield is measured by comparing with a standard material whose absolute efficiency has been established under careful experiment conditions. The optical density of the test sample is normally kept below 0.05 to avoid inner filter effects. The quantum yield can be calculated using Eq. 5.10 [84]

$$\phi_f = \Phi_{fR} \frac{I}{I_R} \frac{OD_R}{OD} \frac{n^2}{n_R^2} \tag{5.10}$$

where ϕ_f is the fluorescence quantum yield,
I is the integrated intensity,
OD is the optical density,
n is the refractive index,
R, as a subscript, refers to the reference fluorophore with known quantum yield.

5.3.1.2 Stokes Shift

The Stokes shift is the difference between the maximum peaks of the fluorescence and the absorption spectra (see Fig. 5.8). It is always expressed as a wavenumber $\Delta\nu$

$$\Delta\nu = \nu_a - \nu_f \tag{5.11}$$

where ν_a and ν_f correspond to the wavenumbers at $\lambda_a(\text{max})$ and $\lambda_f(\text{max})$, respectively.

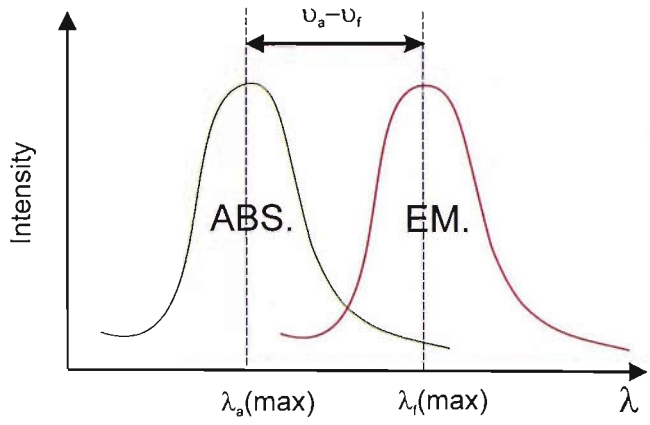

FIGURE 5.8: Definition of the Stoke shift.

5.3.1.3 Energy Transfer Between Organic Molecules

When a molecule A is in the vicinity of an excited molecule D*, the energy transfer of electronic excitation energy from the donor molecule D* to acceptor molecule A can occur. The process may be represented as

$$D^* + A \longrightarrow D + A^* \tag{5.12}$$

The transfer processes generally occur in two ways – radiative transfer and non-radiative transfer. The former process generally refers to the process which involves the emission of a photon by the donor molecule and subsequent re-absorption by the acceptor molecule (see Fig. 5.9(a)), whereas the latter is a process which does not involve the appearance of a photon (Fig. 5.9(b)). The interaction can take on two forms depending on the distance between donor and acceptor molecules.

- Electron exchange interaction, also known as Dexter transfer and
- Dipole-dipole interaction (Fluorescence resonance energy transfer (FRET) or Förster transfer).

The Dexter transfer is a short-range (6-15 Å) interaction process where excitons diffuse from donor to acceptor sites via intermolecular electron exchange [85]. The Förster transfer is a long-range interaction process which can occur mainly through dipole-dipole interaction. The distance between the donor and acceptor molecules is typically within the range of 50-100 Å[86].

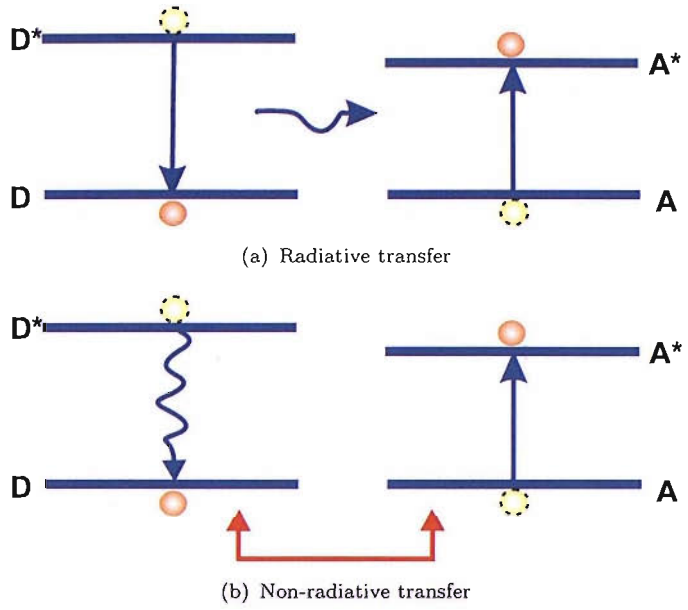

FIGURE 5.9: Radiative and non-radiative transfers.

5.3.1.4 Re-absorption Mechanism

Re-absorption refers to the process whereby the emission light is re-absorbed by the fluorescence dye molecules. This mechanism is a radiative process. It generally occurs due to the spectral overlap between the absorption and fluorescence bands. This effect results in the distortion in shape of measured fluorescence spectra, as shown in Fig. 5.10. The effect leads to an artificial red shift of the short-wavelength edge, it is sometimes called a red-shift effect [14, 87]. It should be noted that, the fluorescent material should have a large Stokes shift to avoid or minimise this effect.

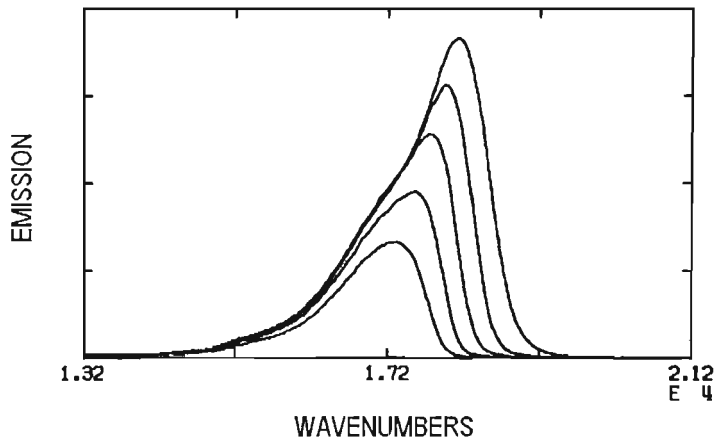

FIGURE 5.10: The distortion of fluorescence spectra due to re-absorption. Original source [88].

5.3.1.5 Quenching

Quenching is a process whereby excited molecules do not radiate because of the presence of quencher molecules. This mechanism often occurs in a substances with high concentration. The effect results in the decrease of intensity of the emission light and also the fluorescence quantum yield [35].

5.3.2 Light Propagation

When the fluorescent light is emitted, either it will be re-absorbed by the absorbing species or it will be delivered to the edge of the FC. The light propagation within the FC is based on total internal reflection mechanism described in section 2.6.

In this section, we consider the fraction of light trapped inside the FC in 2 cases: re-absorption is very small and can be neglected and re-absorption loss is non-negligible.

Case I: FC with no re-absorption loss

To determine the fraction of light trapped inside the FC with no re-absorption loss, we assume that

1. the FC is a homogeneous layer and has the refractive index n_{FC} larger than unity,
2. the FC is surrounded by air ($n_{air} = 1$) and
3. the light emitted from luminescence species is perfectly isotropic.

The critical angle θ_c related to the refractive index of the FC can be derived using Eq. 5.13.

$$\theta_c = sin^{-1}\left(\frac{1}{n_{FC}}\right) \tag{5.13}$$

The fraction of photons inside the critical cone p is given by

$$p = \frac{A}{4\pi r^2} \tag{5.14}$$

where A is the area that subtends the cone of light escaping from the top and bottom surfaces of the film.

$$A = 2\pi r^2(1 - cos\theta_c) \tag{5.15}$$

Substitute Eq. 5.15 into 5.14, we obtain

$$p = \frac{(1 - cos\theta_c)}{2} \tag{5.16}$$

The fraction of photons inside the critical cone from both faces is given by

$$P = 2p = 1 - cos\theta_c \tag{5.17}$$

Hence, the fraction of rays trapped inside the collector is

$$f_{trap} = 1 - P = cos\theta_c \tag{5.18}$$

Assuming $n_{FC} = 1.50$, we obtain $\theta_c \approx 42°$, $f_{trap} \approx 74.5\%$ and $P \approx 25.5\%$.

Case II: FC with re-absorption mechanism

To determine the fraction of light trapped inside the FC when the re-absorption loss is non-negligible, the previous assumptions are considered. We also assume further that the average re-absorption probability of fluorescence emitted outside the critical cone is equal to R and the average re-absorption probability of fluorescence emitted inside the critical cone is equal to $\overline{R}$. The fraction of rays trapped inside the FC which includes these re-absorption probabilities f_{trap2} is

$$f_{trap2} = (1 - P)(1 - R) + P\overline{R} \tag{5.19}$$

5.3.3 Fresnel Reflections Inside the Critical Angle

In reality, the fluorescence emitted at angles less than the critical angle is not able to escape from the FC plate completely due to the difference between the refractive index of the FC and its surrounding. A portion of light that arrives the interface with angle less than θ_c can be partially reflected and undergoes total internal reflection. The reflections of fluorescent light inside the critical cone can simply be calculated

using the Fresnel equations (see Eq. 3.3). By assuming $n_{air} = 1$ and $n_{FC} = 1.50$, the reflectance at the interface can be obtained as shown in Fig. 5.11. It is seen that when the light is incident at the interface with angles larger than the critical angle (~42°), the reflectance is equal to unity. This means the fluorescent light is totally reflected back into the FC. As the angle becomes less than 42°, the reflectance drops dramatically and its value becomes constant (approximately 4%). To calculate a more accurate f_{trap}, the reflection inside the critical cone, Eqs. 5.18 and 5.19 can be re-written as

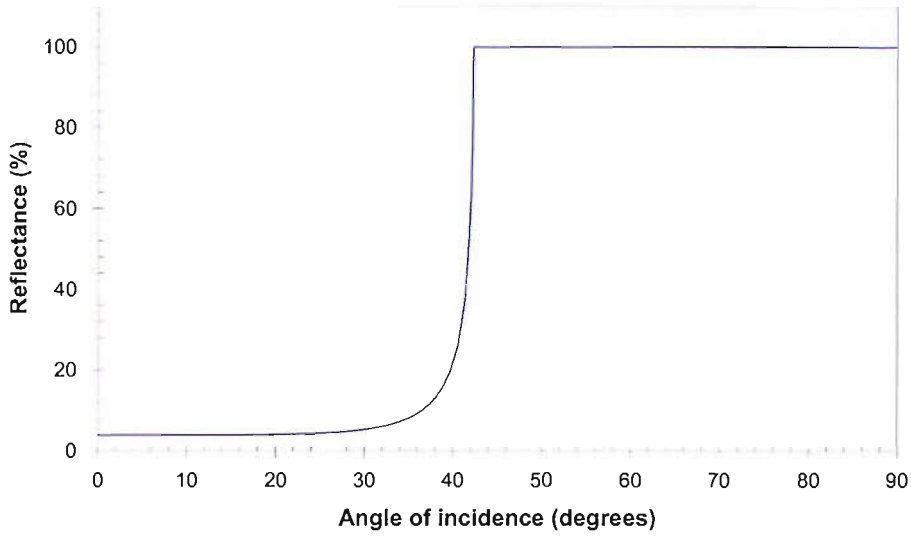

FIGURE 5.11: The reflectance of light inside a fluorescent collector.

$$f_{trap3} = 1 - P + f_{add} \tag{5.20}$$

$$f_{trap3} = (1 - P)(1 - R) + P\overline{R} + f_{add} \tag{5.21}$$

where f_{add} is the total fraction of the photons inside the critical cone that undergoes Fresnel reflection. It can be expressed as [89]

$$f_{add} = PF_R \tag{5.22}$$

P is the fraction of photons inside the critical cone and F_R is the fraction of photons within the critical cone which are Fresnel reflected. The photons transport within

the fluorescent collector can be summarised through the diagram as shown in Fig. 5.12.

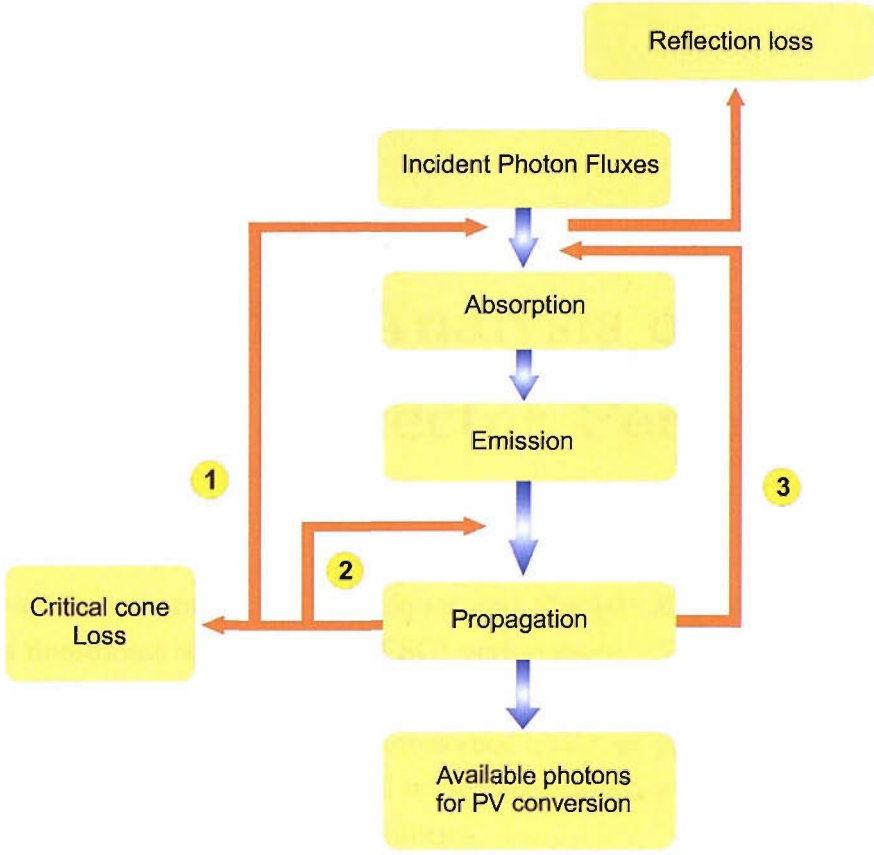

FIGURE 5.12: Diagram of elementary processes in a fluorescent collector. Process ① refers to re-absorption of fluorescence emitted inside the critical cone. Process ② refers to the Fresnel reflections inside the critical angle. Process ③ refers to re-absorption of fluorescence emitted outside the critical cone.

Chapter 6

Techniques for Analysis of Fluorescent Collector Performance

In this chapter, we present the techniques and theoretical models for quantitative analysis of fluorescent solar collector (FSC) performance. The major parameters considered here include: the ability to absorb light by the fluorescent collector (absorption efficiency), the ability to emit light (fluorescence quantum yield), the ability to transport light to the edge where a solar cell is located (collection efficiency), the efficiency of the FC and the re-absorption probabilities.

6.1 Absorption Efficiency

The absorption efficiency of the fluorescent collector Q_A is defined as the ratio of the number of the photons absorbed within the FC to the number of the photons incident onto the front-face of the FC.

$$Q_A = \frac{\Phi_{abs}}{\Phi_{in}} \tag{6.1}$$

where Φ_{in} is the total number of photons which is incident onto the front-face of the FC

$$\Phi_{in} = \int_{\lambda_1}^{\lambda_2} \Phi(\lambda) d\lambda \tag{6.2}$$

and Φ_{abs} is the number of the photons that can be absorbed by the collector. It can be obtained using Eq. 2.59.

Substituting Eqs. 2.59 and 6.2 in Eq. 6.1, we obtain

$$Q_A = \frac{\int_{\lambda_1}^{\lambda_2}(1 - R(\lambda))\Phi(\lambda)\left[1 - 10^{-\alpha(\lambda)d}\right] d\lambda}{\int_{\lambda_1}^{\lambda_2}\Phi(\lambda)d\lambda} \tag{6.3}$$

It should be recalled that $R(\lambda)$ is the reflectance of the front face of the FC and d is the absorbing path length.

6.2 Collection Efficiency

The next key parameter that is needed to determine the performance of a fluorescent collector is the collection efficiency Q_C. This parameter is defined as the probability that the absorbed photons will be emitted at the edge. In an ideal case, i.e., for the FC with no re-absorption or transport losses, the Q_C is equal to the fraction of photons emitted inside the critical cone P. In the practical situation, there are several loss mechanisms involve during the photon transport. Thus, it results in the decrease of the Q_C.

To determine the collection efficiency of the FC, the analytical models discussed in section 5.2 (see Eqs. 5.2 and 5.6) can be employed. These models, however, were formulated by assuming that one edge of the fluorescent collector is perfectly coupled to a solar cell. An ideal mirrored surface is also assumed for the edge opposite the device. The models do not take into account the actual circumstances, e.g., when the coupling interface is not perfect or the quality of the mirror is less than ideal. These conditions can have a major influence on the collection efficiency. Therefore, we have developed a more rigorous model to take into account of these effects. The model, which is called 'Two Photon Fluxes' model (TPF), allows us to compute the collection efficiency more realistically compared to the Weber and Lambe and Batchelder *et al.* models.

To evaluate the Q_C, a typical structure of FSC shown in Fig. 5.1 is considered. For simplicity of analysis, we assume

i) The incident light is uniformly absorbed within the collector,
ii) The light emitted from luminescent species is assumed to be perfectly isotropic,

iii) The probability that photons emitted outside critical cone will be re-absorbed before arriving at the edge of the collector R is

$$R = \int_0^\infty f_1(\lambda) r(\lambda) d\lambda \tag{6.4}$$

where $r(\lambda)$ is the probability that photons emitted outside the escape cone will be re-absorbed within wavelength $d\lambda$ and $f_1(\lambda)$ is the normalised first generation fluorescence which satisfies the following normalisation condition

$$\int_0^\infty f_1(\lambda) d\lambda = 1 \tag{6.5}$$

iv) The probability that photons emitted inside the escape cone will be re-absorbed is small and can be neglected.

In order to derive Q_C, let us now consider the key parameters listed as follows:

- total number of emitted photons,
- number of photons emitted at the edge,
- fluorescence collection efficiency.

6.2.1 Total number of emitted photons

To calculate the total number of photons emitted after Φ_{in} photons are absorbed per unit time (with a fraction Q_A), we consider the probability of transition of a molecule between two energy levels: excited level (B) and ground state level (A) (see Fig. 6.1).

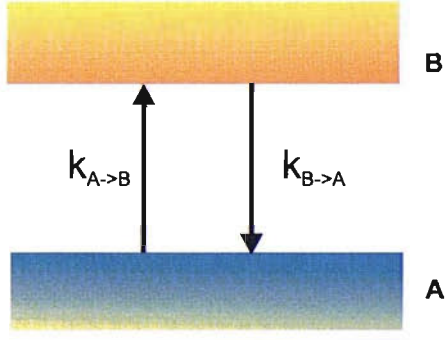

FIGURE 6.1: Two energy levels. A and B represent ground state level and excited state level, respectively.

Let us denote N^* is the number of molecules in the excited level, ϕ_f is the fluorescence quantum yield and τ_{rad}, τ_{nrad} and τ_{tot} are the radiative, non-radiative and total lifetime, respectively. The numbers of transitions between the two states per unit time within the collectors are

$$k_{A\to B} = \Phi_{in} Q_A + \frac{1}{\tau_{rad}} N^* R(1-P) \tag{6.6}$$

$$k_{B\to A} = \frac{1}{\tau_{tot}} N^* \tag{6.7}$$

The first term on the right-hand side of Eq. 6.6 represents the number of externally incident photons which are absorbed. The second term gives the number of photons which have been emitted within the collector and are re-absorbed along their paths to the edge of the collector.

The principle of the detailed balance requires that the rates of transition between two states A and B satisfy

$$k_{A\to B} = k_{B\to A} \tag{6.8}$$

Thus

$$\Phi_{in} Q_A + \frac{1}{\tau_{rad}} N^* R(1-P) = \frac{1}{\tau_{tot}} N^* \tag{6.9}$$

Since

$$\tau_{tot} = \phi_f \tau_{rad} \tag{6.10}$$

Eq. 6.9 becomes

$$\frac{1}{\tau_{tot}} N^* = \frac{\Phi_{in} Q_A}{1 - \phi_f R(1-P)} \tag{6.11}$$

The total number of photons emitted within wavelength $d\lambda$ is

$$\frac{N^*}{\tau_{tot}} f_1(\lambda) d\lambda \tag{6.12}$$

6.2.2 The number of photons emitted at the edge

The number of photons emitted at the edge of the collector within wavelength $d\lambda$, $f_e(\lambda)$, can be obtained by taking into account in Eq. 6.12 the escape cone loss (1-P) and self-absorption loss 1-$r(\lambda)$,

$$f_e(\lambda)d\lambda = (1-P)[1-r(\lambda)]\frac{N^*}{\tau_{tot}}f_1(\lambda)d\lambda \tag{6.13}$$

From Eq. 6.11, we can re-write Eq. 6.13 in terms of absorbed photons as

$$f_e(\lambda) = \Phi_{in}Q_A\frac{(1-P)[1-r(\lambda)]}{1-\phi_f R(1-P)}f_1(\lambda)d\lambda \tag{6.14}$$

Equation 6.14 shows that the photons emitted outside the escape cone, which will be reabsorbed within wavelength $d\lambda$, can be found from the ratio of two quantities - $\widetilde{f_e}(\lambda)$ and $f_1(\lambda)$.

$$1-r(\lambda) = \frac{\widetilde{f_e}(\lambda)}{f_1(\lambda)} \tag{6.15}$$

where $\widetilde{f_e}$ is the fluorescence signal emitted at the edge per total amount of absorbed photons

$$\widetilde{f_e} = \kappa\frac{f_e}{\Phi_{in}Q_A} \tag{6.16}$$

and

$$\kappa = \frac{1-\phi_f R(1-P)}{1-P} \tag{6.17}$$

6.2.3 Fluorescence collection efficiency

Equation 6.14 can be presented in a simpler form as

$$f_e(\lambda) = \Phi_{in}Q_A\chi(\lambda)f_1(\lambda) \tag{6.18}$$

where $\chi(\lambda)$ is 'fluorescent collection efficiency', which is defined as the probability that a photon of externally incident light absorbed within the collector is emitted at the edge of the fluorescent collector.

$$\chi(\lambda) = \frac{(1-P)[1-r(\lambda)]}{1-\phi_f R(1-P)} \tag{6.19}$$

Note that in the case of $R = 0$, the parameter $\chi(\lambda)$ is given by

$$\chi(\lambda) = (1-P)[1-r(\lambda)] \tag{6.20}$$

Figure 6.2 presents, as an example, the plot of absorbance, emission spectra and the corresponding factor χ. It is clearly seen that $\chi(\lambda)$ is approximately equal to zero within the region where the absorption and emission spectra strongly overlap. The value tends to increase at the longer wavelength region where the re-absorption process has less influence and finally reaches its maximum limit within the region where the re-absorption process is absent.

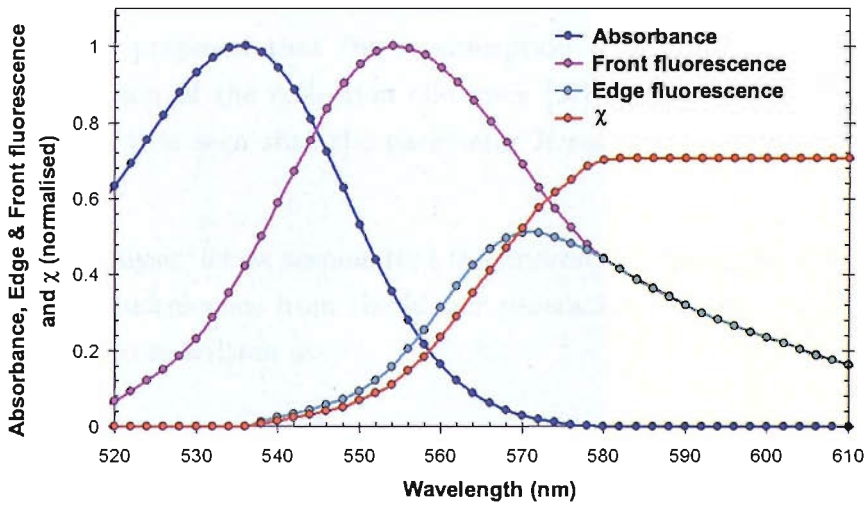

FIGURE 6.2: Dependence of $\chi(\lambda)$ on normalised absorbance and fluorescence spectra.

6.2.4 Collection Efficiency

The collection efficiency Q_C which is defined as the probability that the absorbed photons will be emitted at the edge, is given as

$$Q_C = \int_0^\infty \chi(\lambda) f_1(\lambda) d\lambda \tag{6.21}$$

Substitute $\chi(\lambda)$ from Eq. 6.19 to 6.21, we obtain

$$Q_C = \int_0^\infty \frac{(1-P)[1-r(\lambda)]}{1-\phi_f R(1-P)} f_1(\lambda) d\lambda \tag{6.22}$$

6.3 Re-absorption Probability

The re-absorption probability is a parameter that is used to quantitatively evaluate the re-absorption loss of the fluorescent light. In this section, we consider two possible methods that may be employed to obtain this parameter.

6.3.1 Method I: Re-absorption Probability Through Collection Efficiency

Batchelder *et al.* proposed that the re-absorption probability can be determined through a calculation of the collection efficiency [67]. According to the expression shown in Eq. 5.4, it is seen that the parameter R can be obtained if the collection efficiency is known.

To simplify the analysis, let us assume that the fluorescence quantum yield ϕ_f is equal to unity and the fluorescence from the higher generation emission can be neglected. Equation 5.4 can be re-written as

$$Q^1 = (1-P)(1-R) \tag{6.23}$$

where the parameter Q^1 is equal to the $Q_{C,Web}$ (see Eq. 5.2).

The re-absorption probability can now be derived from

$$R = 1 - \frac{Q_{C,Web}}{(1-P)} \tag{6.24}$$

Note that the accuracy of R derived from Eq. 6.24 depends entirely on the accuracy of $Q_{C,Web}$. As already described in section 5.2, $Q_{C,Web}$ was formulated by assuming that

there are no reflection losses at the interfaces. In addition, the fluorescent collector was assumed to be perfectly coupled to a solar cell. The model does not take into account the actual circumstances, i.e., when the coupling interfaces are not perfect or the quality of the reflector is less than ideal. As these conditions can influence the correction efficiency and subsequently the re-absorption probability, it is essential to formulate a model that takes into account these effects.

In this section, we develop a model to determine Q_C in a more realistic way. The model was modified from Weber and Lambe's expression which takes into account:

1) the effect of non-ideal reflection at the interface and
2) the effect of non-perfect coupling between the fluorescent collector and the solar cell.

The structure of the FSC considered in the model is shown in Fig. 6.3. The non-perfect coupling between the fluorescent collector and the solar cell is considered to be due to the presence of an air gap at the interface. The reflectivity of the mirror or reflector is assumed to be less than 1.

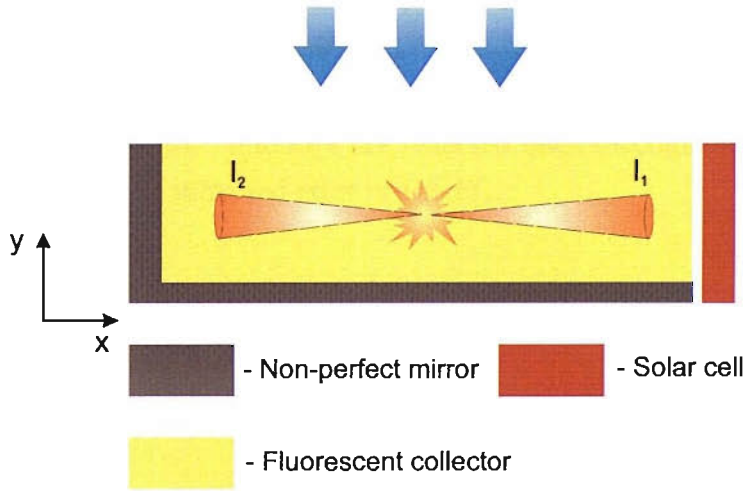

FIGURE 6.3: Cones of rays that can escape from the FC. I_1 presents a cone of rays propagating towards a solar cell and I_2 presents a cone of ray propagating away the device.

Due to the presence of the air gap between the fluorescent collector and the solar cell, the amount of light that emerges from the edge of the fluorescent collector corresponds to only a fraction of rays bounded within the critical cone, whose half-angle equals to

$$\theta_C = sin^{-1}\left(\frac{n_0}{n_{FC}}\right) \tag{6.25}$$

where n_0 is the refractive index of air,

n_{FC} is the refractive index of the collector.

The cones of rays propagating along the x-axis are divided into two parts. The first part is the cone of rays propagating towards the detector and the second part is the cone of rays propagating in the opposite direction.

The fraction of rays re-absorbed within the collector is given by

$$R = 1 - \frac{I_1 + R_f I_2}{(1 + R_f)(1 - P)} \tag{6.26}$$

where R is the re-absorption probability,

R_f is the reflectance of the reflective materials which are coupled to the edges of FC,

I_1 is the fraction of luminescent light inside a critical cone θ_C propagating towards the detector (see Fig. 6.3),

$$I_1 = \frac{1}{\alpha L} \int_0^{\theta_C} \left(1 - exp\left(\frac{-\alpha L}{cos(\theta)}\right)\right) cos(\theta) sin(\theta) d\theta \tag{6.27}$$

I_2 is the fraction of luminescent light inside a critical cone θ_C propagating away from the detector. The rays are reflected back through the detector when they reach the mirrored edge of the FC.

$$I_2 = \frac{1}{\alpha L} \int_0^{\theta_C} \left(exp\left(\frac{-\alpha L}{cos(\theta)}\right) - exp\left(-2\frac{\alpha L}{cos(\theta)}\right)\right) cos(\theta) sin(\theta) d\theta \tag{6.28}$$

α is absorption coefficient and L is the width of the FC.

6.3.2 Method II: Re-absorption Probability Through Fluorescence Spectra

An alternative method that can be used to determine the re-absorption probability is by computing the ratio of the fluorescence spectra observed at the edge and the front-face of the fluorescent collector. This method was first proposed by Abdel *et al.* [90] but it has not been widely cited. One possible reason is that the authors did not provide the detailed analysis of how the re-absorption loss can be derived from the front-face fluorescence and the edge fluorescence spectra.

Since this method is able to determine the re-absorption probability without the need to know the collection efficiency, it has been revisited by our research group. Based on the detailed analysis presented in section 6.2, we have found that the re-absorption probability can be obtained from the ratio of two quantities: the fluorescence signal emitted at the edge per total amount of absorbed photons and the first generaton fluorescence (see Eq. 6.15). This equation suggests that the re-absorption probability can be obtained only if the first generation fluorescence and the edge fluorescence spectra are known.

As mentioned in section 5.2, the term first generation fluorescence refers to the fluorescence spectra emitted without any re-absorption effect. To obtain such spectra in practice, the concentration of the tested sample must be very low in order to minimise the number of the absorbing molecules. In addition, the front-face detection arrangement should be employed in order to minimise the re-absorption mechanism [35, 91, 92]. The reason is that the front-face arrangement allows us to measure the fluorescence signal which is emitted from the sample with minimum optical path length. Therefore, the detected spectra experience less self-absorption processes.

6.4 Efficiency of Fluorescent Collector

The efficiency of the fluorescent collector can be found based on the following equation:

$$\eta_{FC} = \phi_f Q_A Q_c \tag{6.29}$$

where η_{FC} is efficiency of fluorescent collector,
Q_A is absorption efficiency,
Q_C is collection efficiency and
ϕ_f is fluorescent quantum yield.

The photon flux gain at the edge of the FC can be computed using Eq. 6.30 [65].

$$\Phi_G = G\eta_{FC} \tag{6.30}$$

where G is geometric gain of the FC.

6.5 Electrical Output of FSC

When the FC plate is coupled to a solar cell, it will result in the enhancement of the cell output current. The current generated from the cell, when the FC is illuminated with photons at wavelength $d\lambda_{ex}$, is related directly to the photon fluxes available at the edge of the FC plate.

$$I_f(\lambda_{ex}) = q \int [1 - R_{PV-FC}(\lambda_{em})] IQE(\lambda_{em}) f_e(\lambda_{em}) d\lambda_{em} \tag{6.31}$$

where q is electronic charge,

$I_f(\lambda_{ex})$ is the current generated from the cell when the device is illuminated with wavelength $d\lambda_{ex}$,

$R_{PV-FC}(\lambda_{em})$ is the reflectance at PV-FC interface at wavelength $d\lambda_{em}$

$f_e(\lambda_{em})$ is the number of fluorescent photons arriving at the PV-FC interface,

IQE(λ_{em}) is the internal quantum efficiency of the solar cell at wavelength $d\lambda_{em}$.

According to Eqs. 6.18 and 6.21, we can express Eq. 6.31 in the other form as

$$I_f(\lambda_{ex}) = qA_f\Phi(\lambda_{ex})[1-R_{A-FC}(\lambda_{ex})]\left(1 - 10^{-\alpha(\lambda_{ex})d}\right)\phi_f Q_C[1-R_{PV-FC}(\lambda_{em})]IQE(\lambda_{em}) \tag{6.32}$$

where A_f is the front-face area of the collector,

$\Phi(\lambda_{ex})$ is the photon fluxes at wavelength $d\lambda$ that incident onto the collector,

$R_{A-FC}(\lambda_{ex})$ is the reflectance at the air-FC interface,

$IQE(\lambda_{em})$ is the internal quantum efficiency over the emission wavelength,

$R_{PV-FC}(\lambda_{em})$ is the reflectance at PV-FC interface over the emission wavelength,

ϕ_f is fluorescent quantum yield. This term is added into the expressions due to the need to take into account of the non-ideal emission.

Chapter 7

Development of Fluorescent Collectors and Characterisation Tools

The fluorescent collector can be prepared using several methods. One of the methods commonly used is to dissolve fluorescent molecules in a polymer matrix material[1]. Such polymer materials are, for example, polyimide, polystyrene, epoxy resin and polymethylmethacrylate (PMMA) [93]. To make a thick plate of the fluorescent collector, these polymer solutions are usually placed into a mould and polymerized under UV light or under high temperature [20, 94]. Alternatively, the polymer solution can be spun-coated onto a glass substrate in order to create a thin film of the fluorescent collector [23, 95]. This method requires less fluorescent material compared to the first approach. The thickness of the fluorescent collector can be simply varied by changing the thickness of the glass substrate.

In this chapter, we present in detail the method that was developed to fabricate fluorescent collectors. The fabrication gives the flexibility to control the conditions of our study. In addition, we discuss details of the measurement systems developed to characterise the optical properties of the FCs including the absorbance and the fluorescence measurements.

The chapter is divided into three sections. The first section describes the structure and also the properties of materials that were used to develop the fluorescent collectors. Section two provides the methods for fabricating the samples. Section three explains the details of the characterisation techniques.

[1]The matrix material is a rigid material used to support the fluorescent molecules or ions.

7.1 Structure of Fluorescent Collectors

Figure 7.1 illustrates the structure of the FCs developed in this work. The FC comprises of three major components: a fluorescent material, a matrix material and a substrate.

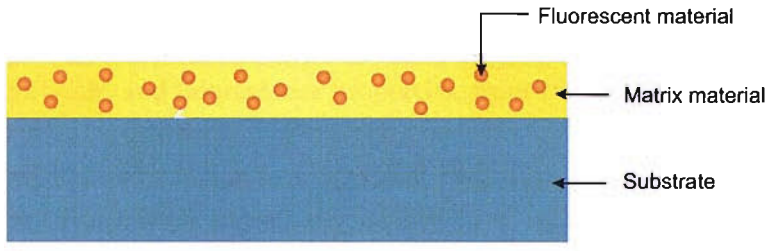

FIGURE 7.1: The structure of fluorescent collector.

7.1.1 Fluorescent Material

The fluorescent material used in this study is Rhodamine 6G (Rh6G), also known as Rhodamine 590 chloride. The Rh6G was chosen because of its high fluorescence quantum yield of 95%, a reasonably good photostability, low cost and solubility in organic solvents [96–99]. It was purchased from Acros with original purity around 99% and was used as received without further purification. In ethanol, it exhibits an absorption peak at 530 nm and a fluorescence peak at 552 nm. The chemical structure of Rh6G and its important absorbance and fluorescence properties are shown in Fig. 7.2.

It is important to note that the data presented in the figure is provided as a guideline only. In practice, the presented values may vary depending on the solvent and matrix material under study.

7.1.2 Matrix Material

We consider Methyl Methacrylate (MMA), a chemical compound known for the production of transparent plastic [100], as a matrix material because of four major reasons:

(1) It shows the best optical transparency in the visible spectral range [101],
(2) The optical loss due to reflection at the polymer/air interface is quite low (less than 4%) [102, 103],

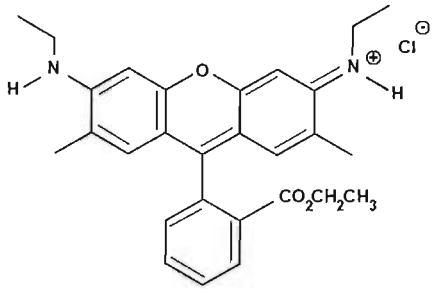

Absorption and Fluorescence Properties	
Maximum absorbance	530 nm
Maximum fluorescence	552 nm
Fluorescence quantum yield	0.95
Molar absorption coefficient	116,000 $L \cdot mol^{-1} \cdot cm^{-1}$

FIGURE 7.2: The chemical structure of Rh6G ($C_{28}H_{31}CLN_2O_3$) and its important absorbance and fluorescence properties, from PhotochemCAD [96].

(3) It has excellent resistance to ultraviolet radiation and weathering [104, 105],

(4) It does not react with water.

In order to prepare a matrix material of MMA, Tensol 12, a colourless liquid acrylic solvent cement by BOSTIK FINDLEY, was employed. This product is often used to produce a clear bond in cast acrylic sheets. However, in this study, the product was used to perform as a matrix material since it comprises MMA as the major constituent (around 60-100 %). It also contains Dichloromethane (DCM, CH_2Cl_2), which is a good solvent for the Rh6G.

7.1.3 Substrate

Glass microscope slides (Menzel-Gläser, Germany) were used as a substrate as they are cheap and compatible with the spin coating process. Additionally, glass has a higher refractive index than the surrounding material (n_{glass} (1.52) $> n_{air}$) and so it helps to confine and guide the fluorescent light that emerges from the film.

7.1.4 Reflector

Two types of reflectors were used to construct the FC. The one underneath the FC plate (back mirror) is a 25.4×25.4 mm^2 aluminium mirror from Thorlabs. This mirror has the reflectance > 85% within the region 400-700 nm.

The reflectors which were located close to the edges of the FC were Aluminium foil coated glass slides. These reflectors were used since they can be easily made to have their contact dimension match to the area of the FC edge. In addition, the reflectance of the Al foil was found to be quite high[2] (> 80% within the region 350–800 nm).

[2]The reflectance of the aluminium foil was measured by Dr. Robert Greef using an ellipsometer.

7.2 Sample Preparation

The samples were prepared by spin coating an Rh6G solution onto square glass (2.6×2.6 cm^2 glass slide, 1 mm thick).

The substrates were prepared by cutting the glass slides into 26×26 mm^2 squares. The slides were subsequently polished using an automatic grinding wheel with SiC paper. The polishing was performed to obtain a parallel and smooth surface. The glasses were then cleaned using the following steps:

(i) ultrasonic clean in a Decon 90 (2%) solution for 20 minutes,
(ii) rinse with deionized (DI) water,
(iii) rinse with acetone in order to remove oils and organic residues.

The spincoat solution was prepared by diluting Rh6G with Dichloromethane (DCM, Laboratory Reagent Grade, Fisher Scientific) before mixing with Tensol 12 (RS) in an ultrasonic bath for 3 minutes. The mixture ratio was fixed at 6:2(w/v), 6 g of MMA per 2 ml of Rh6G in DCM solution. The prepared spincoat solution was dispensed onto the glass slide and spun at a constant speed of 3.4 krpm for 1 minute. The uniformity and thickness of the films were tested by a profilometer (Form Taylsurf- 120 L, Rank Taylor Hobson Limited), Leicester, England). The instrument has a diamond tip of 2 μm and a laser interferometer pick-up unit to measure the displacement with a resolution of 20 nm [106].

To inspect the quality of the prepared films, three different positions of five samples were chosen randomly and tested. The film within the chosen area was partly removed in order to create a step prior the scanning. The probe was set to scan across the film-glass step with the total distance around 1 cm. The results show that the surface of the films produced in this way was quite smooth and uniform. The thickness of the films was 9 ± 1 μm.

7.3 Characterisation Techniques

This section describes two major techniques that were used to characterise the optical properties of the prepared samples. These are the absorbance and fluorescence measurements. The absorbance measurement is very useful in quantification of the amount of absorbing molecules. It can also provide the absorption spectrum of the

samples. The fluorescent measurement is another method used to measure the emission characteristics of the fluorescent molecules. The fluorescence spectra obtained from the measurements can also be used to extract valuable data about the nature and efficiencies of various processes such as fluorescence quantum yield and collection efficiency.

Figure 7.3 shows the diagram of the system used to measure the absorbance and fluorescence spectra of the samples. The system consists of three major parts: an excitation light source, measurement modules for absorbance and fluorescence measurements (Setups I to IV) and a spectrometer.

A Xenon lamp (75 W) and monochromatic light emitting diodes (LED, LUXEON STAR 3 W) were used as the excitation light. The light was guided to illuminate a test sample which was mounted in the measurement module. The output light from a sample was measured using a spectrometer system (Bentham).

The Bentham spectrometer system is composed of a grating monochromator (TM300), a photomultiplier tube (PMT: Hamamatsu type R446) and a data acquisition and control unit. The monochromator is for wavelength selection. The PMT is used to detect and amplify the optical signal. The data acquisition and control unit is connected to a personal computer to control the monochromator and convert the output signal of the PMT into digital data.

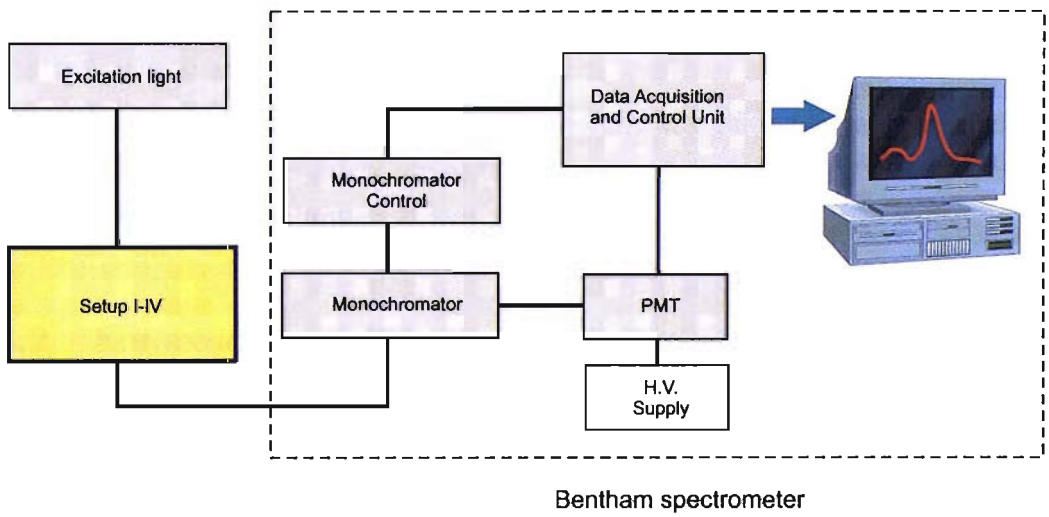

FIGURE 7.3: Schematic of the apparatus for absorbance and fluorescence measurement. The setup I-IV corresponds to the optical arrangements for the absorbance and fluorescence measurements.

7.3.1 Absorbance Measurement

The absorbance of the sample $A(\lambda)$ can be determined using the Beer-Lambert law as shown in Eq. 7.1.

$$A(\lambda) = log\frac{I_r}{I_i} \tag{7.1}$$

where I_r is the intensity of the light transmitted through a reference sample, a glass slide coated with an undoped Tensol 12 film, and I_i is the intensity of the light transmitted through a test sample.

A schematic diagram of the system (Setup I), which is used to measure these light intensities, is depicted in Fig. 7.4.

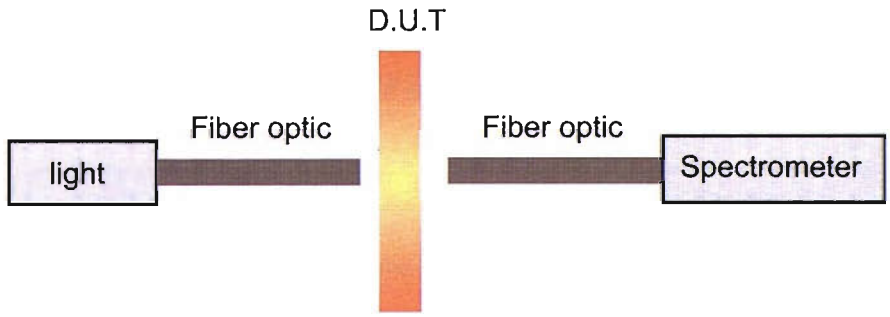

FIGURE 7.4: Setup I – the optical arrangement for absorbance measurement. D.U.T is a device under test, which is a reference or test sample.

A Xenon lamp was used as a light source. The light was guided to a device under test (D.U.T), which is either a reference or test sample, via an optical fibre. The intensity of the light transmitted through the sample was guided to the spectrometer.

7.3.2 Fluorescence Measurement

To measure the fluorescence spectra, the sample is illuminated with a continuous beam of monochromatic light and the intensity of the emission spectra is recorded. Three different arrangements (Setup II-IV) were used to detect the fluorescence light emitted from the test samples:

1. Front–face fluorescence detection
2. Edge fluorescence detection
3. Right angle fluorescence detection.

The first and second arrangements were used to measure the fluorescence spectra emitted from the front surface and from the edges of the samples, respectively. The third arrangement was used to measure the fluorescence spectra of the fluorescent materials in 1 cm pathlength cuvettes. These spectra were characterised to determine the re-absorption loss of the sample, which will be discussed in Chapter 8.

7.3.2.1 Front–face fluorescence detection

Figure 7.5 shows the setup of the front–face fluorescence measurement. A Xenon lamp with 480 nm band pass filter (10 nm bandwidth) was used as the excitation source. The light was guided to illuminate the front surface of the sample through an optical fiber and a combination of lenses. The incident beam was fixed at 30° relative to the substrate. The fluorescence light emitted from the sample was detected using another optical fiber. The fiber was set up to detect the emission light normal to the front surface. This arrangement enables us to measure the fluorescence signal which is emitted from the sample with minimum optical path length, to minimise the self-absorption.

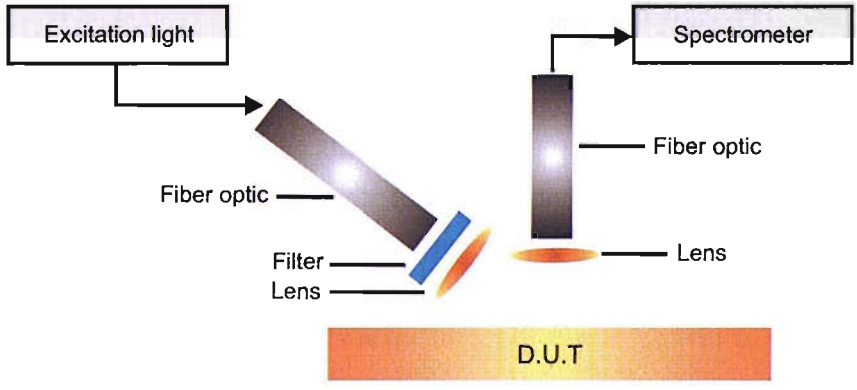

FIGURE 7.5: Setup II – Setup for Front Fluorescent Detection.

7.3.2.2 Edge fluorescence detection

Figure 7.6 illustrates the experimental setup used to measure fluorescence light emitted from the edges of the fluorescent collectors. The excitation light, which is a high power LED with excitation peak at a wavelength of 465 nm, was positioned to provide a strong intensity and also uniform illumination over the whole area of the sample. A combination of lenses was used to focus the light emitted from the edge of the sample into the optical fibre, which was connected to the Bentham spectrometer.

Note that the remaining edges and the area underneath of the samples were covered by Al-reflectors to enhance the absorption path length and also to minimise the loss of fluorescent light at the interfaces (see section 8.3 for more details.).

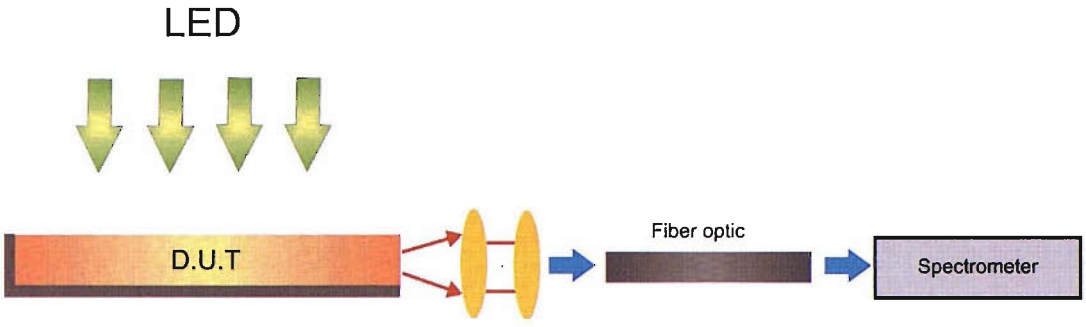

FIGURE 7.6: Setup III – Setup for Edge Fluorescent Detection.

7.3.2.3 Right angle fluorescence detection

In addition to the above two techniques, the right angle detection was also employed to detect the fluorescence signal from the samples. This arrangement was considered because it is the most common geometry used for fluorescence detection [107]. It also allows us the measure the emission signal of the spincoat solutions used to prepare the fluorescent collectors. Figure 7.7 illustrates the system used to measure the fluorescence spectra of the spincoat materials that were placed in 1 cm path length optical glass cuvettes. A Xenon lamp was used as the excitation source. It was guided through an optical fibre connected to a 1 cm path length Cuvette holder. The guided light was then passed through a narrow bandwidth filter (10 nm BW) which was located close the cuvette to provide a well defined spectrum with a maximum peak at 480 nm. The emitted light was detected and guided to the spectrometer via another optical fiber which was coupled to the cuvette holder at a 90° angle relative to the direction of the exciting light beam.

7.4 Conclusion

In this chapter, we presented the method that was developed to prepare the fluorescent collectors. The structure of the collector comprises of three major components: a fluorescent material, a matrix material and a glass substrate. The samples were prepared

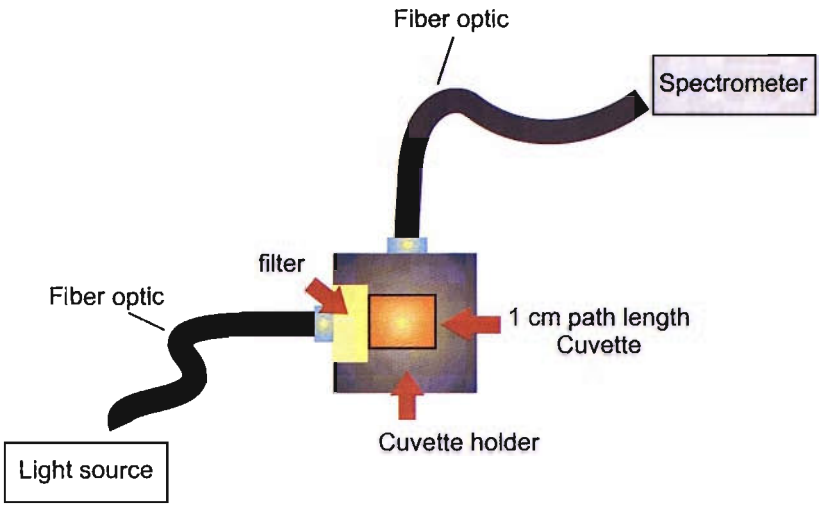

FIGURE 7.7: Setup IV – Setup for right angle detection.

by spin-coating a solution of polymeric material onto glass substrates. By fixing the rotating speed of the spin coater at 3.4 krpm, we can obtain a smooth and uniform coated surface. The thicknesses of the films tested by a profilometer was within the range of approximately 9 μm.

The optical characterisation systems employed to measure the absorbance and fluorescence spectra are described. To obtain the absorbance spectra, the intensities of the Xenon light transmitted through a test sample and a reference sample were measured. The absorbance spectra were obtained from these intensities by using the Beer-Lambert law.

The fluorescence spectra can be characterised using three different arrangements. The first and the second arrangements were used to measure the fluorescent signal emitted from the front surface and from the edge of the FC, respectively. The third arrangement was used to measure the fluorescent signal emitted from the right angle of 1 cm path length cuvette.

Chapter 8

Results and Discussion

This chapter presents the experimental results of the optical characterisation of the fluorescent collectors. The absorbance and fluorescence spectra were analysed using the techniques described in Chapter 6 to study the photon transport losses occuring within the FCs. The major parameters obtained from the analysis are the absorption efficiency, the collection efficiency, the fluorescence quantum yield, the re-absorption probability and the efficiency of the fluorescent collectors.

8.1 Absorbance of Rh6G film

The absorbance spectra of the FCs prepared from various concentrations of spincoat solutions of Rh6G (from 1.51×10^{-4} to 1.58×10^{-3} M) are given in Fig. 8.1. It shows that the collectors absorb light in the visible region, from approximately 440 to 570 nm. The absorption band consists of a major peak at 536 nm with a weak shoulder on the higher energy side (~500 nm). The peak absorbance of the sample prepared from the low and high concentration spincoat solutions are 0.07 and 0.58, respectively.

Note that the shape of the Rh6G spectra is quite similar in different media e.g. water and ethanol [108]. The peak absorbance and the shoulder correspond to the absorption from the S_0 level to the S_1 state and its vibronic sub-bands [35, 109].

The absorption efficiencies Q_A of these samples were computed using Eq. 6.3. The calculated results were plotted with the concentrations of the Rh6G spincoat solution as shown in Fig. 8.2. It shows that the absorption efficiency tends to increase as the concentration increases. The absorption efficiency of these samples was in the range of 16% to 66%. It is crucial to note that the absorption efficiency is quite sensitive to

the upper and lower limits of the wavelength chosen during the integration. In this analysis, we are interested in the absorption efficiency in the region where the dye can strongly absorb the light. Thus, these limits were defined as the wavelengths where the absorbance is less than 10% of its peak value.

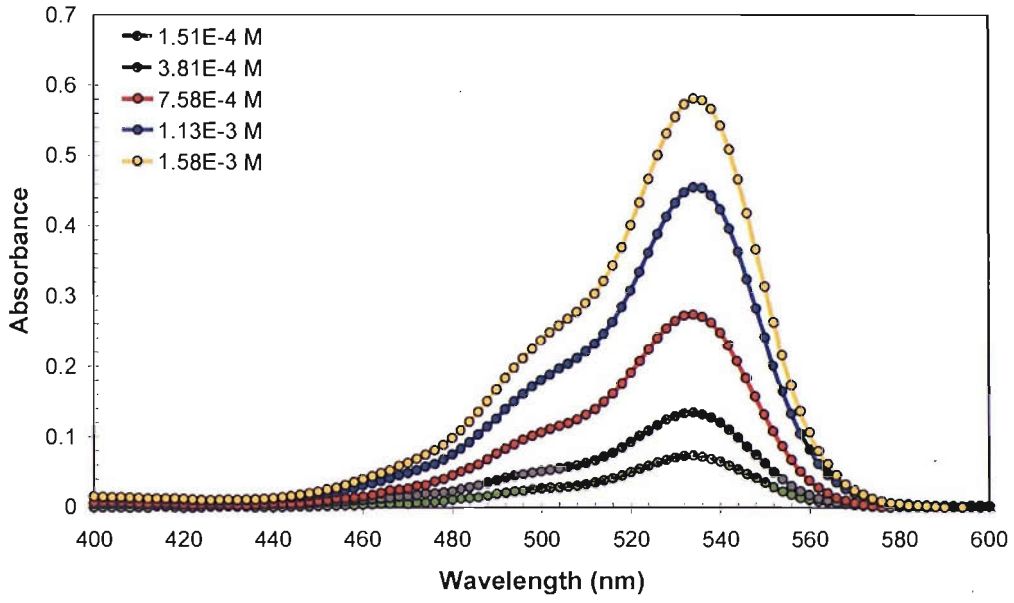

FIGURE 8.1: The absorbance spectra of Rh6G films at various concentrations.

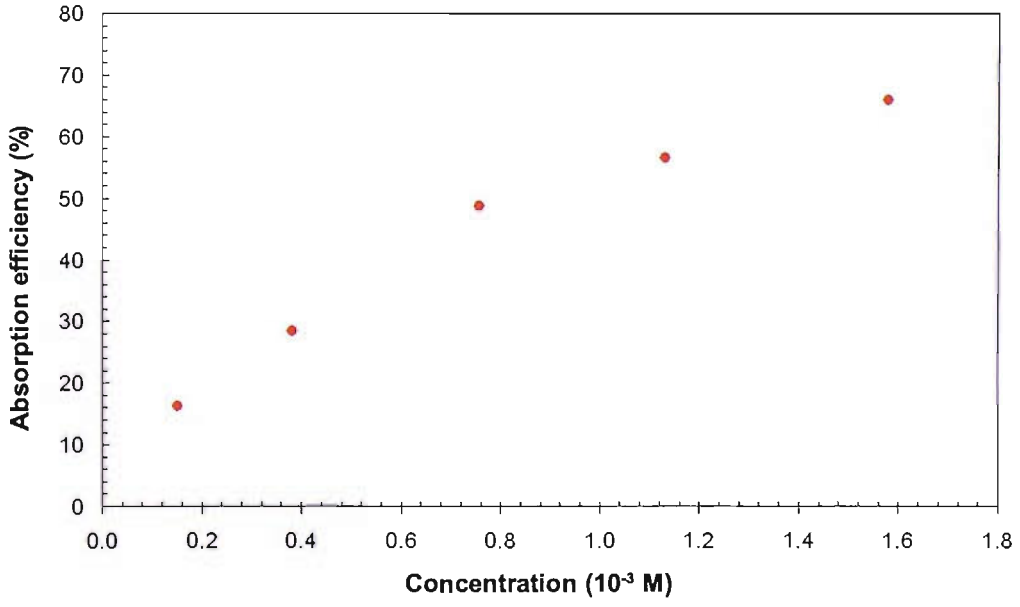

FIGURE 8.2: The dependence of absorption efficiency on concentration of spincoat solution.

8.2 Fluorescence Study of Rh6G films

This section discusses two major results that were obtained from the fluorescence measurements: edge fluorescence spectra and first generation fluorescence spectra. These results were characterised with the following purposes:

1. to determine the spectral features of the fluorescent light emitted from the samples, prepared from different dye concentration,
2. to determine the fluorescence spectra that are emitted without any re-absorption effect or also known as first generation fluorescence spectra,
3. to determine the re-absorption losses at each wavelength ($r(\lambda)$).

It should be recalled that $r(\lambda)$ can be determined by comparing the first generation fluorescence spectra with the emission spectra measured at the edge of the collectors (see Eq. 6.15).

8.2.1 Determination of the edge-emitted fluorescence spectra

Figure 8.3 shows the fluorescence spectra emitted from the edges of the FCs as described in the previous section. The results were obtained using the setup shown in Fig. 7.6. The plot indicates that the photons, which were guided to the edges of the collectors, were within the range of 530-670 nm. Because of the re-absorption mechanism, the fluorescent signal tends to shift to the longer wavelength region as the concentration increases. This characteristic is similar to those reported in [68, 72, 110–112]. The red-shift of the signal corresponding to the re-absorption process of the sample will be further analysed and discussed in more detail in section 8.5.2.

8.2.2 Determination of the first-generation fluorescence spectra

Two approaches were investigated to characterise the first generation fluorescence spectra. The first approach is the measurement of fluorescence spectra emitted from the front surface of the samples. In order to minimise the re-absorption loss, the measurements were performed with low absorbance samples (peak absorbance is between 0.04 and 0.28).

Figure 8.4 shows the fluorescence spectra observed from the front surface of the samples. The spectra were measured using the arrangement shown in Fig. 7.5. Again,

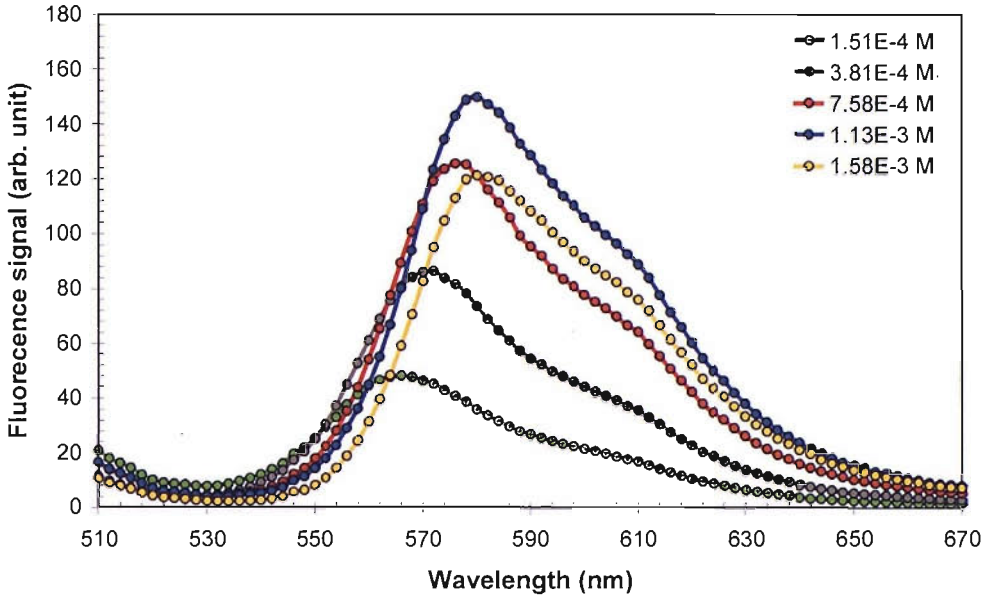

FIGURE 8.3: The fluorescence emission spectra at various concentrations, detected at the sample edge.

the results exhibit a red-shift of the fluorescence spectra as the absorbance increases. Although this characteristic was similar to that presented in Fig. 8.3, it is essential to point out that a smaller red-shift, approximately 10 nm, was observed in the present arrangement. In addition, it was also found that the shift of the spectra is no longer observed when the absorbance of the sample is less than 0.07. This key feature suggests that the spectra detected from the front surface of the samples, which have absorbance less than 0.07, are not affected by the re-absorption mechanism. Hence, such spectra were considered as the first generation fluorescence of the fluorescent collectors developed in this work.

Another approach used to determine the first generation fluorescence spectra was the measurement of fluorescence light emitted from the low concentration spincoat material in a 1 cm path length cuvette. This approach was employed as it allows measurement of the fluorescence spectra of the sample with a well defined dimension. It also offers the potential to measure the fluorescence signal of very low concentration samples.

In this study, this method was used to determine the emission signal of the sample prepared with the concentration of 5.2×10^{-7} M. The right angle detection (see Fig. 7.7) was used to measure the fluorescence spectra. The spectra were recorded when the solution was freshly prepared and when it was left to dry at room temperature for one week (due to solvent evaporation). The latter condition was chosen as it is believed that the composition of the dried spincoat material was similar to that of the

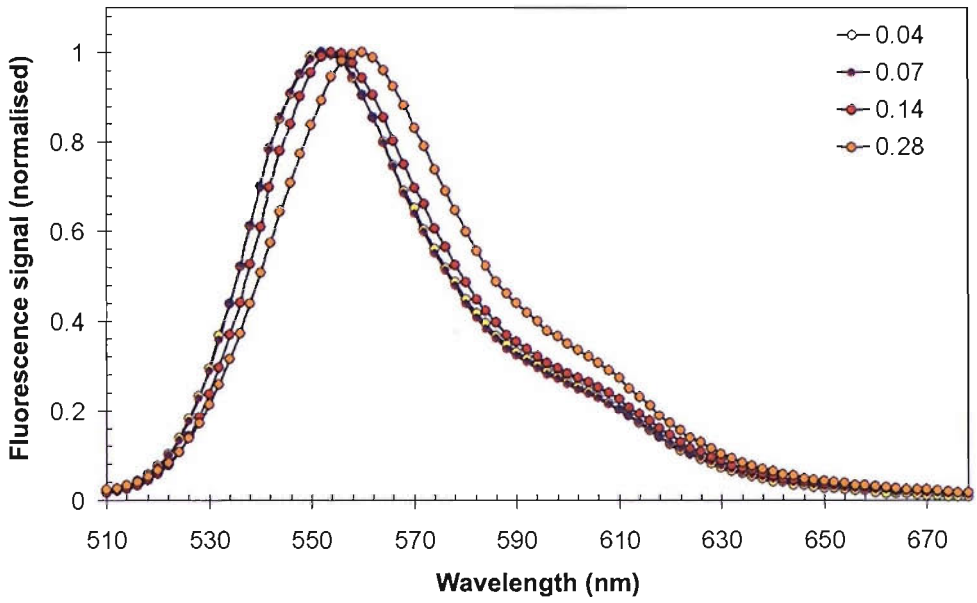

FIGURE 8.4: Fluorescence spectra detected from the front surface of fluorescent collectors. The spectra were normalised to unity at their peaks.

spin coat film. The thicker block of the material can provide a stronger fluorescence signal, which enables the measurement to be made.

Figure 8.5 compares the fluorescence spectra of the spincoat material in a solid block to that in solution. It is clearly seen that the fluorescence spectra is shifted to the longer wavelength region as the sample dries. The reason of this shifting can be explained in terms of the change in solvent nature or composition, called solvatochromic shift [35, 107].

It may seem logical to conclude that this shift results from a re-absorption mechanism arising from the increase in molecule concentration due to solvent evaporation. However, the absorbances of the spincoat material in both solid and liquid form are quite low (see Fig. 8.6) and so re-absorption loss is unlikely to be the cause of this shifting. Another interesting feature of the plot is the shift of the absorbance peak to the longer wavelength region, which is consistent to that observed in the emission spectra. Hence, this characteristic confirms that the composition of the sample was altered when it dried.

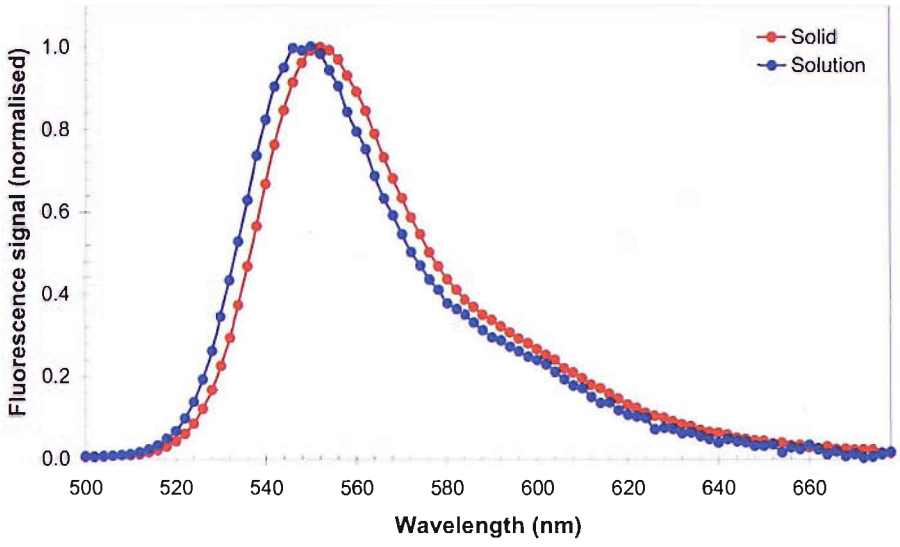

FIGURE 8.5: Fluorescence spectra of the spincoat solution and the solid block of the spincoat material

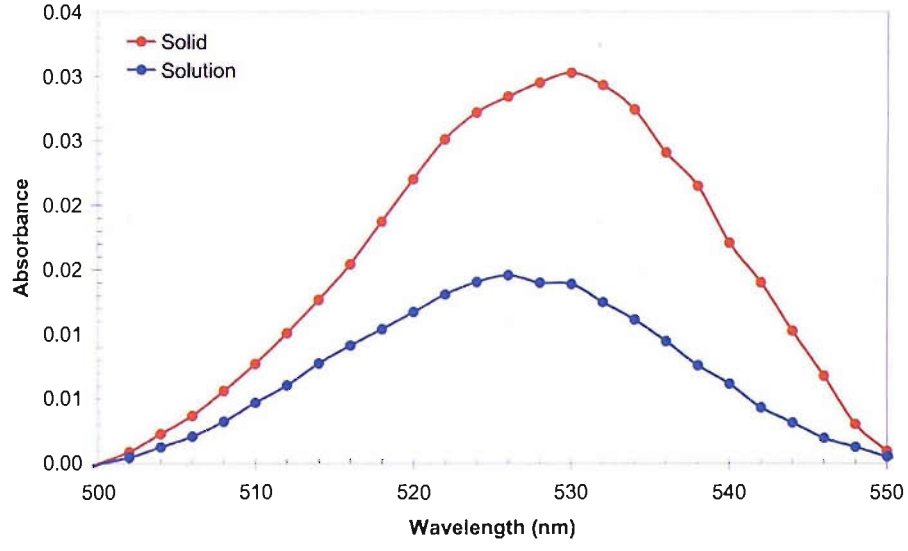

FIGURE 8.6: Absorbance of the spincoat material in two forms: solution and solid block.

To further investigate the influence of the concentration of spincoat solution on the shifting of the emission signal, the spincoat solution at concentration of 2×10^{-6} M was also tested when freshly prepared. This concentration is approximated to be higher than that of the dried spincoat material investigated previously[1].

Figure 8.7 compares the fluorescence spectra of the spincoat solutions with different concentrations. It is seen that the emission signals almost agree in shape. Therefore, this result confirms that the shift of the spectra shown in Fig. 8.5 is not caused by the increase of the concentration but the solvatochromic shift.

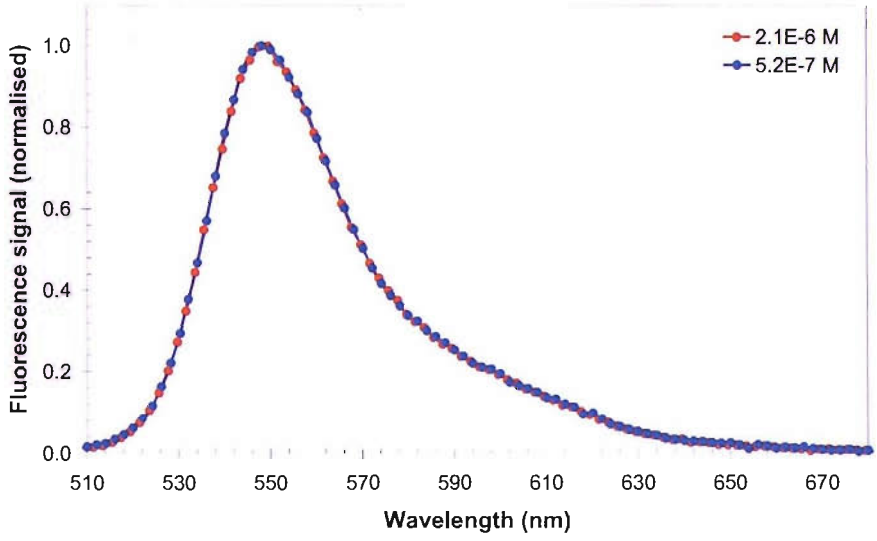

FIGURE 8.7: Fluorescence spectra of the spincoat solutions with different concentrations.

To examine whether the first generation fluorescence obtained from the two approaches are in good agreement, the fluorescence spectra of the sample with concentration of 1.51E-4 M was compared to that of the solid block of the spincoat material (see Fig. 8.8). The plot indicates that the emission spectra of the block sample and the film do not entirely agree. The difference is probably due to the composition of the spincoat material being not completely solid when the measurement was taken.

[1]The concentration of the dried spincoat material is approximated to be 1.7×10^{-6} M. This concentration was calculated by considering the volume of dried spincoat material is around 1/3 of the fresh solution.

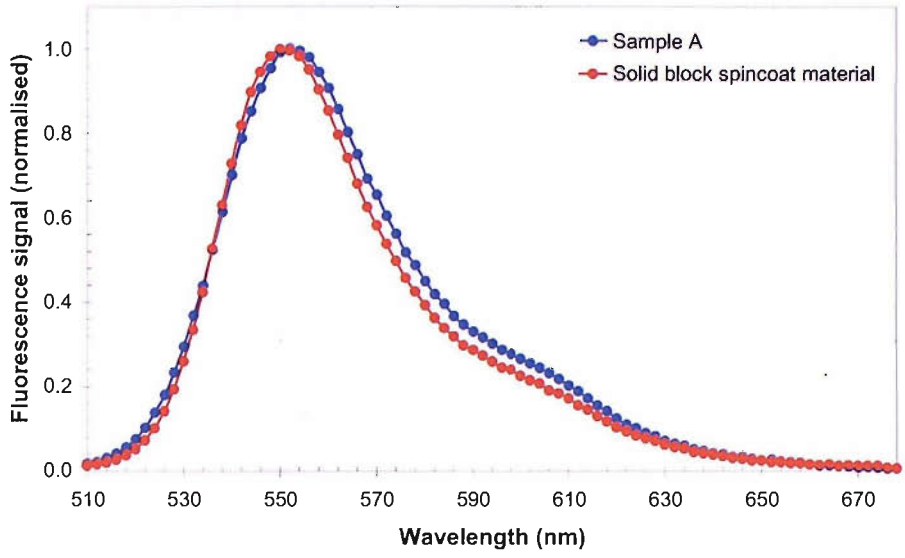

FIGURE 8.8: Fluorescence spectra of the Rh6G film on glass slide and the solid block of the spincoat material in glass cuvette.

8.3 The role of reflectors in fluorescent collector performance

Figure 8.9 illustrates the arrangements, which were set up to determine the role of Al-reflectors on the performance of the FC. The fluorescence signals measured at the edge of the FC are presented in Fig. 8.10. It was observed that the Al-reflector plays a major role in the fluorescence spectra detected from the edge of the FC. The fluorescent intensity was lowest without any reflectors (configuration E). By introducing the Al-reflector underneath the FC (configuration D), the intensity of the observed spectra is doubled. This is because the absorbing path length is enhanced to be twice the FC thickness. Adding more Al-reflectors to the remaining edges (configurations A-C) also helped maximise the intensity of the fluorescence signal.

Comparing configuration C and D, it is seen that the fluorescent intensity obtained from configuration C is approximately 1.4 times higher than that of configuration D. The increase of the fluorescence signal is because the fluorescence that can escape on this side was directed back to the detector. It was also noticed that the peak intensity was slightly shifted toward the longer wavelength as the reflector was introduced. This shifting arises from the increase in the re-absorption probability due to an increase in the optical path length of the rays.

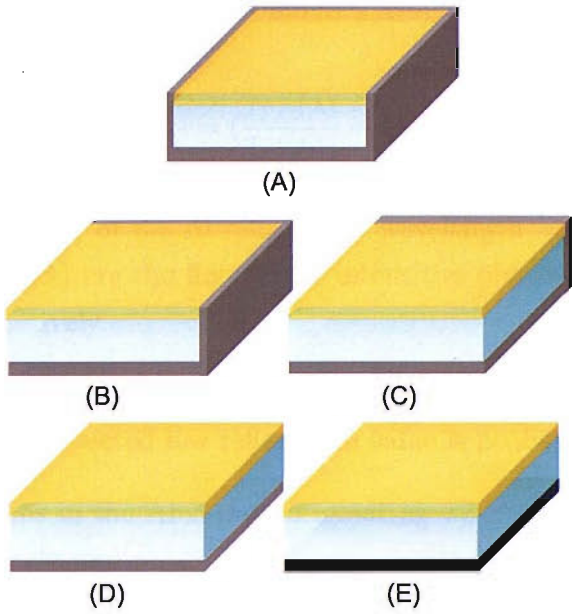

FIGURE 8.9: Various arrangements set up to determine the role of reflectors. Configuration A–the bottom side and three edges of the FC are coupled to reflectors. Configuration B–the bottom side and two edges of the FC are coupled to reflectors. Configuration C–the bottom side and one edge of the FC are coupled to reflectors. Configuration D–only the bottom side is coupled to a reflector. Configuration E–the bottom side is coupled to a blackened material.

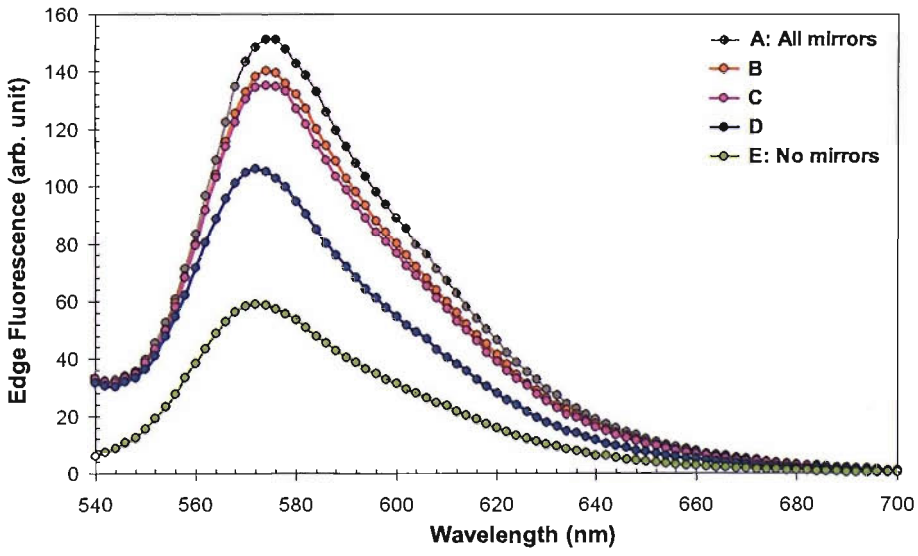

FIGURE 8.10: The edge fluorescence spectra of FCs shown in Figure 8.9. Curves A-E correspond to the configurations A-E, respectively

To obtain the reflectance of the Al-reflector used in this study, the fluorescent intensity of configurations C and D were further analysed using Eq. 8.1.

$$R_{Al}(\lambda) = (\frac{I_{F,C}(\lambda)}{I_{F,D}(\lambda)} - 1) \times 100 \tag{8.1}$$

where $R_{Al}(\lambda)$ is reflectance of the Al-reflector at wavelength λ and
$I_{F,C}(\lambda)$ and $I_{F,D}(\lambda)$ are the fluorescent intensities obtained from configurations C and D, respectively.

Based on the computation, we found that the reflector is approximately 40% reflective (see Fig. 8.11). The unexpected low reflectance value is probably due to:

1. the imperfections in the Al-surface originating when the Al-foil was stuck onto the glass substrate and
2. the non-uniformity of the edge area.

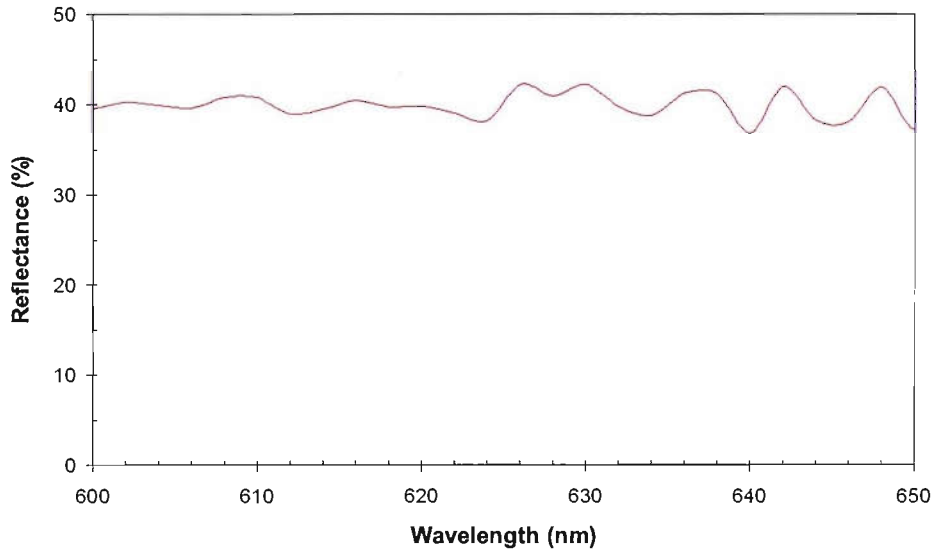

FIGURE 8.11: The reflectance of the Al-reflector placed at the edge of the FC.

In addition, it was noticed that the Al-reflector that was placed at the edge of the FC as shown in configuration B can slightly enhance the fluorescent intensity. The increase of the fluorescence signal is, however, clearly observed when another reflector was added (configuration A). The increase of the measured signal is probably because the fraction of rays that can be Fresnel-reflected inside the critical cone can be reflected back to the detector after multiple reflections. This process can be simply illustrated in Fig. 8.12.

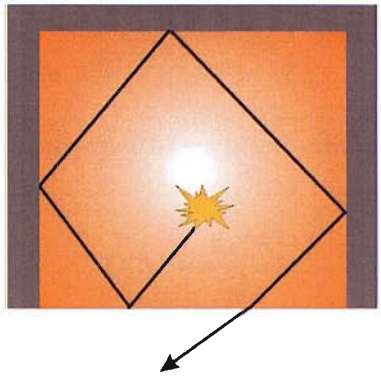

FIGURE 8.12: The path length of rays that are Fresnel-reflected inside the critical cone.

The role of reflectors in the edge fluorescent intensity is summarised in Figure 8.13. The results were obtained by integrating the fluorescent intensity from 600 nm to 700 nm. The maximum integrated value was normalised to unity.

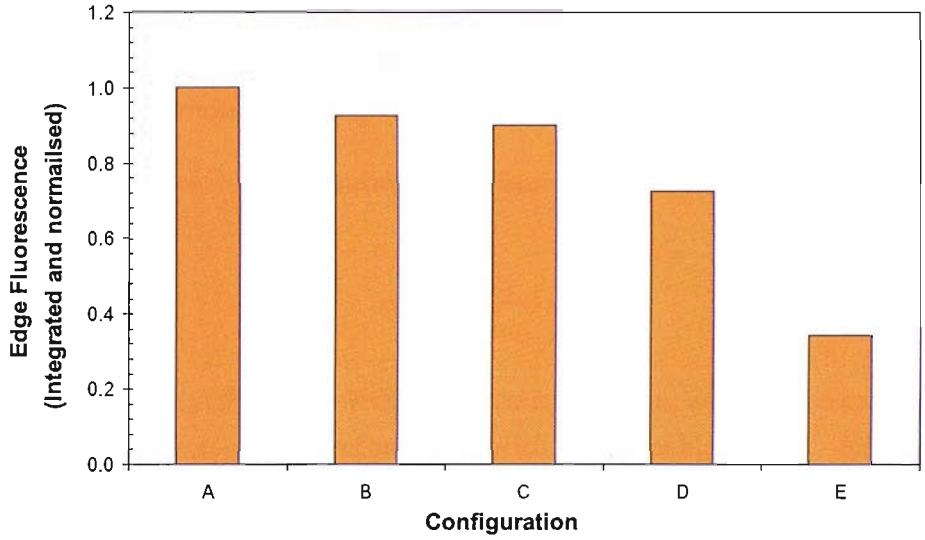

FIGURE 8.13: The edge fluorescent intensity (integrated and normalised) of the collectors in various configurations.

8.4 Analysis of Fluorescence Quantum Yield

The fluorescence quantum yield can be determined by comparing the test sample to a standard sample with known ϕ_f. Both samples need to be measured under the same conditions in order to obtain accurate results. However, such a method has not been used due to the lack of standard samples which are suitable for this purpose. Therefore, in this study, we employed an alternative method to determine the parameter ϕ_f.

Such a method employs the following procedures to calculate the fluorescence quantum yield of the Rh6G-based samples.

1. Calculate a fluorescent intensity per absorption efficiency $D(\lambda)$ using Eq. 8.2

$$D(\lambda) = \frac{I_F(\lambda)}{Q_A} \tag{8.2}$$

where $I_F(\lambda)$ is the fluorescent intensity and
Q_A is the absorption efficiency[2].

2. Compute the D_{int} from the $D(\lambda)$

$$D_{int} = \int_{\lambda_c}^{\infty} D(\lambda) d\lambda \tag{8.3}$$

where λ_c is the wavelength of the emission light at which the overlap between the absorbance and emission spectra is diminished.

3. Compute the fluorescence quantum yield from the following expression

$$\phi_f = \frac{D_{int}}{D_{int0}} \phi_{f0} \tag{8.4}$$

where D_{int0} is the D_{int} of sample with lowest concentration, ϕ_f is fluorescence quantum yield and ϕ_{f0} is fluorescence quantum yield with no quenching effect. In this analysis ϕ_{f0} was assumed to be 93%, which is equivalent to the yield of low concentration Rh6G in PMMA reported in [113].

Figure 8.14 shows the spectra of the fluorescent intensity per absorption efficiency of the Rh6G-based samples. The plot shows the red-shift of the spectra as the concentration increases. The overall shape of all curves tends to be the same at long wavelengths except for the samples with concentrations of 1.13×10^{-3} M and 1.58×10^{-3} M. In the short wavelength region, the shape is distorted. The distortion of the shape appears to be larger as the concentration increases. This is because the emission of the molecules can be re-absorbed more. This dependence of re-absorption losses on concentration will be discussed in detail in section 8.5.2.

[2]In this analysis the $I_F(\lambda)$ data was taken from Fig. 8.3 and the Q_A data was obtained from section 8.1.

The fluorescence quantum yield of the sample, computed from Eq. 8.4, is shown in Fig. 8.15. The plot shows a rapid falling off in the quantum yield when the concentration is higher than 7.6×10^{-4} M. The decrease in ϕ_f is because the dye molecules have a greater chance of being re-absorbed and interacting with each other as the concentration increases. The absorbing molecules can transfer their excitation energy to other molecules rather than emitting light. This effect is understood in terms of the concentration quenching effect which is generally observed in samples with high concentrations [114, 115].

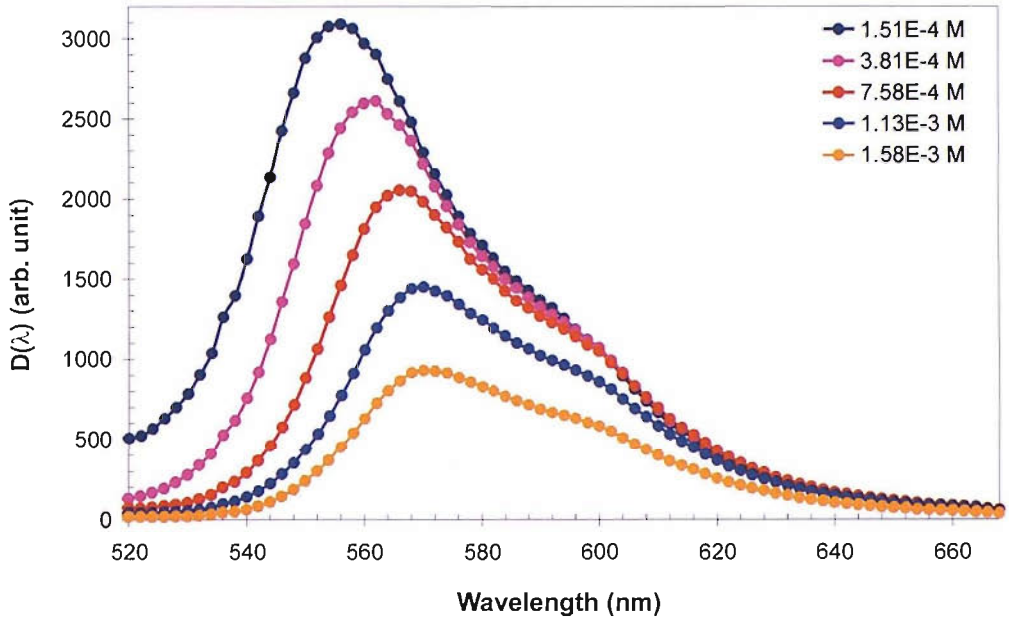

FIGURE 8.14: The dependence of fluorescent intensity per absorption efficiency ($D(\lambda)$) on wavelength of samples with various concentrations.

8.5 Collection Efficiency

The method employed to determine the collection efficiency Q_C was discussed in detail in section 6.2. The collection efficiency is defined as the probability of the absorbed photons being emitted at the edge, which can be expressed as shown in Eq. 6.22.

$$Q_C = \int_0^\infty \frac{(1-P)[1-r(\lambda)]}{1-\phi_f R(1-P)} f_1(\lambda) d\lambda \tag{6.22}$$

where ϕ_f is the fluorescence quantum yield,

$f_1(\lambda)$ is the first generation fluorescence spectra,

P is the probability that the fluorescence light will escape out of the surface,

$r(\lambda)$ is the re-absorption probability at wavelength $d\lambda$ and
R is the total re-absorption probability.

In order to calculate the Q_C, it is clearly seen that we first need to determine the parameters P, $f_1(\lambda)$, ϕ_f, $r(\lambda)$ and R. In section 8.2.2 and 8.4, the measurement of $f_1(\lambda)$ and the analysis of ϕ_f were already described. In the following section, the remaining parameters will be determined.

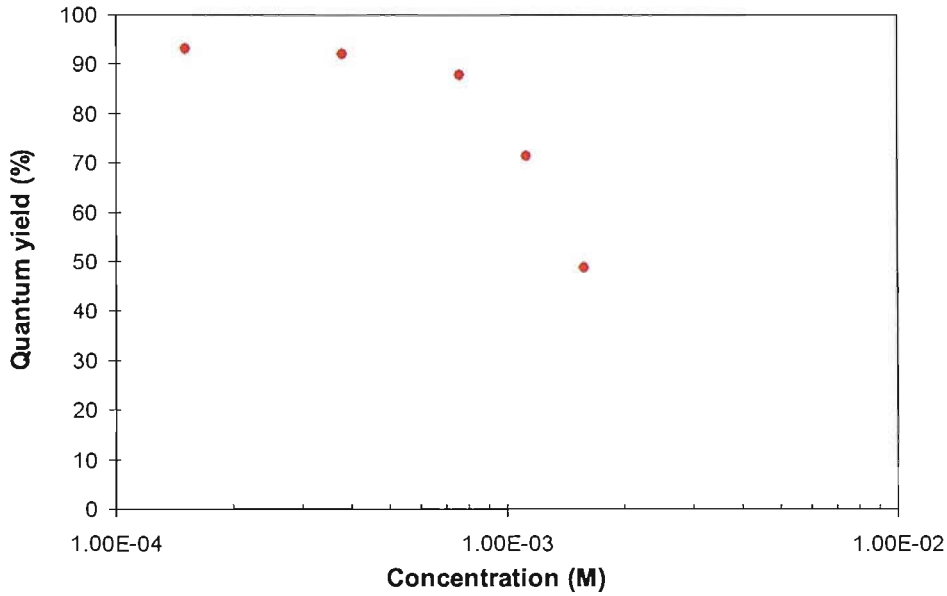

FIGURE 8.15: The dependence of fluorescence quantum yield on concentration of spin coat solution.

8.5.1 The Fraction of Photons Inside the Critical Cone

To determine the fraction of photons inside the critical cone, the structure of the fluorescent collector shown in Fig. 7.1 was considered. For simplicity of analysis, the refractive indexes of the fluorescent film and the glass substrate were assumed to be the same($n_{film} = n_{glass} = n_{FC}$).

The critical angle θ_c related to this refractive index of the fluorescent collector is computed from Eq. 5.13. The fraction of photons inside the critical cone is determined from Eq. 5.17.

Considering $n_{FC} = 1.50$, we obtained $\theta_c \approx 42°$ and $P \approx 25.5\%$. It should be noted that we have neglected the influence of Fresnel reflections within the critical cone.

This approximation should be adequate since the total fraction of photons that undergoes Fresnel reflection is small compared with the fraction of total internally reflected photons.

8.5.2 Re-absorption Losses

The re-absorption loss is one important mechanism related to the collection efficiency of the FC. It occurs due to the spectral overlap between absorption and fluorescence bands. This mechanism results in the distortion of the first generation fluorescence spectra, which is known as the red-shift effect [14, 87].

Theoretically, the re-absorption loss $r(\lambda)$ can be determined by comparing the first generation fluorescence spectra with the emission spectra measured at the edge of the collectors. It can be written as shown in Eq. 8.5

$$r(\lambda) = 1 - \frac{\widetilde{f}_e(\lambda)}{f_1(\lambda)} \tag{8.5}$$

The $f_1(\lambda)$ is the first generation fluorescence spectra, which is the emission spectra without re-absorption losses. In this study, the $f_1(\lambda)$ spectra was obtained by measuring the fluorescence light emitted from the front surface of the low concentration sample. The low concentration sample means it has a small amount of the absorbing molecules. Therefore, it has less chance to re-absorb the emitted light. In addition, the front fluorescence detection provides the minimum re-absorption losses as the detected signal is emitted from the sample with very small optical path length.

The $\widetilde{f}_e(\lambda)$ is the fluorescence spectra at the edge of the FC per total amount of absorbed photons. The $\widetilde{f}_e(\lambda)$ spectra were obtained by computing the ratio between the fluorescence signal detected at the edge of the collectors and the absorption efficiency Q_A.

Since $f_1(\lambda)$ and $\widetilde{f}_e(\lambda)$ were measured under different experimental conditions and setups, it is necessary to normalise these spectra prior to the analysis of $r(\lambda)$. In this analysis, $f_1(\lambda)$ was normalised using Eq. 6.5 to obtain the probability distribution of the emitted photons. $\widetilde{f}_e(\lambda)$ was, then, fitted to the normalised $f_1(\lambda)$ by assuming that there is no re-absorption loss at the long wavelength region where no overlapping occurs between the absorption and emission bands.

The procedures for the fitting are summarised as follows:

1. The $\widetilde{f}_e(\lambda)$ spectrum of the lowest concentration sample was fitted to the normalised $f_1(\lambda)$ spectrum using the least squares technique. Only the spectrum in the long wavelength region, where there is minimum overlapping, was considered.

2. The constant value, obtained from the fitting in step 1, was applied to all remaining spectra.

Figure 8.16 illustrates the normalised absorbance and fluorescence spectra. It is apparent that the shape of the normalised $\widetilde{f}_e(\lambda)$ is distorted from the $f_1(\lambda)$ spectrum. The distortion level tends to be higher as the concentration of the sample increases. This effect results from the re-absorption loss and the concentration quenching as mentioned in section 8.2.1.

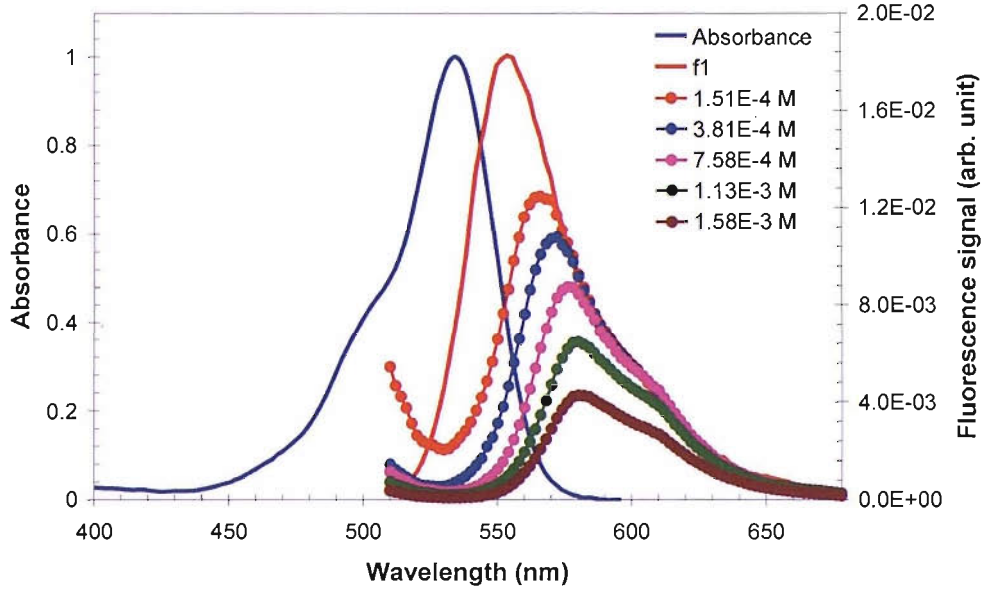

FIGURE 8.16: Normalised absorbance and fluorescence spectra of the samples. The blue line shows, as an example, the normalised absorbance spectrum of the sample. The red line shows the first–generation fluorescence spectrum (f_1) and the dotted lines represent the edge–fluorescence spectra.

In addition, it can be noticed that the normalised $\widetilde{f}_e(\lambda)$ values at the short wavelength region are higher than the normalised $f_1(\lambda)$. This is due to the influence of the excitation light source.

To obtain a more precise value of the re-absorption probability, it is essential to eliminate the effect of the excitation light and also the concentration quenching, which influenced the $\widetilde{f}_e(\lambda)$ spectra. To eliminate the effect of the excitation light, the values of the $\widetilde{f}_e(\lambda)$ spectra at the short wavelength region were fitted to the standard Gaussian shape profile $f(\lambda)$ centered at different wavelength and bandwidth (Eq. 8.6).

$$f(\lambda) = \frac{1}{\sigma\sqrt{2\pi}} e^{-(\lambda-\mu)^2/2\sigma^2} \tag{8.6}$$

where μ is band center wavelength and

σ is bandwidth.

The results of the fitting are presented in Fig. 8.17. For comparison, the raw data from the experiment are also presented. The fitted results were used to determine the re-absorption loss at each wavelength using Eq. 8.5.

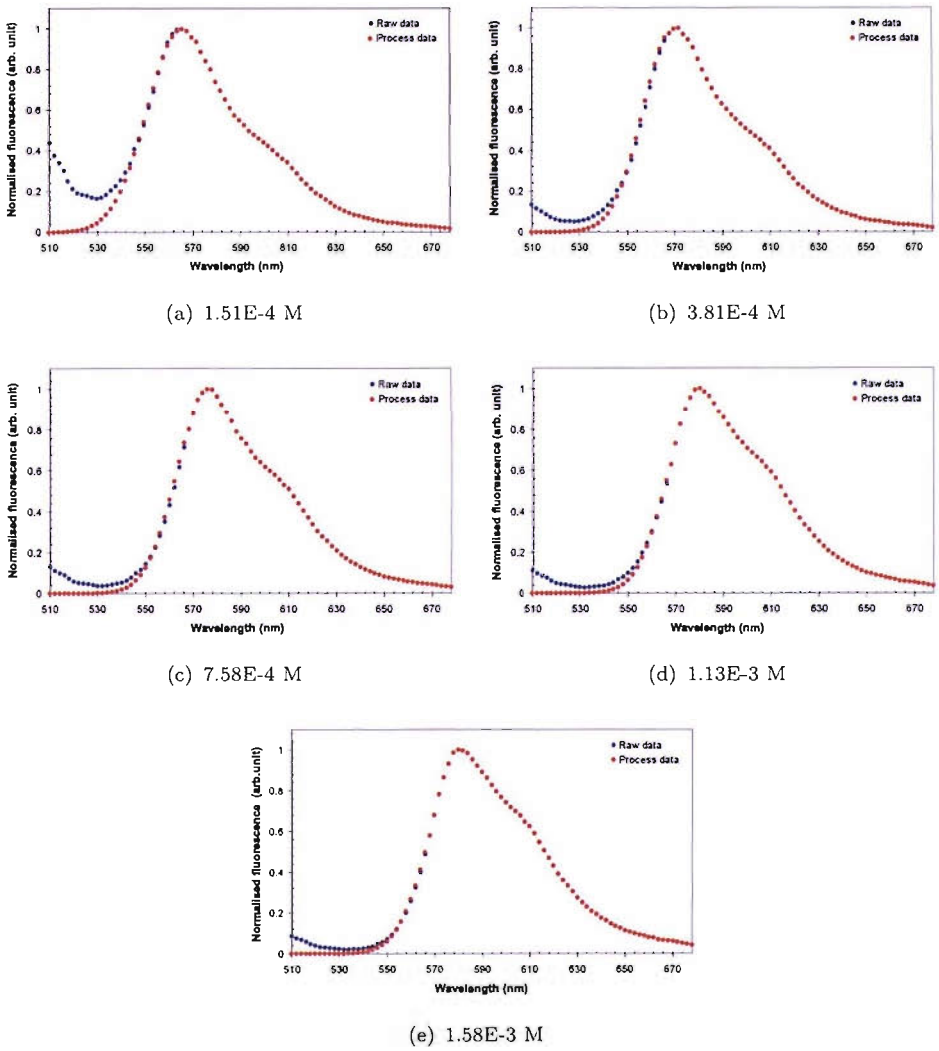

(a) 1.51E-4 M

(b) 3.81E-4 M

(c) 7.58E-4 M

(d) 1.13E-3 M

(e) 1.58E-3 M

FIGURE 8.17: The spectra of the samples before (blue dots) and after (red dots) being processed.

The influence of the concentration quenching on the $\widetilde{f}_e(\lambda)$ spectra was eliminated by re-normalising the $\widetilde{f}_e(\lambda)$ spectra using constant factors C_i. The factors were obtained by considering the drop of the fluorescence quantum yield

$$C_i = \frac{\phi_f}{\phi_{f0}} \tag{8.7}$$

where ϕ_f is the fluorescence quantum yield of the sample and ϕ_{f0} is the fluorescence quantum yield of the sample with no quenching effect. In this study, ϕ_{f0} is obtained from the sample with concentration of 1.51×10^{-4} M.

Figure 8.18 illustrates the dependence of $r(\lambda)$ on various sample concentrations. Apparently, the highest $r(\lambda)$ is located at the short wavelength region, where the absorbance and emission bands strongly overlap. The probability tends to decrease nonlinearly as the wavelength increases. Its magnitude is also related to the concentration of the samples as can be noted from the variation of the curves.

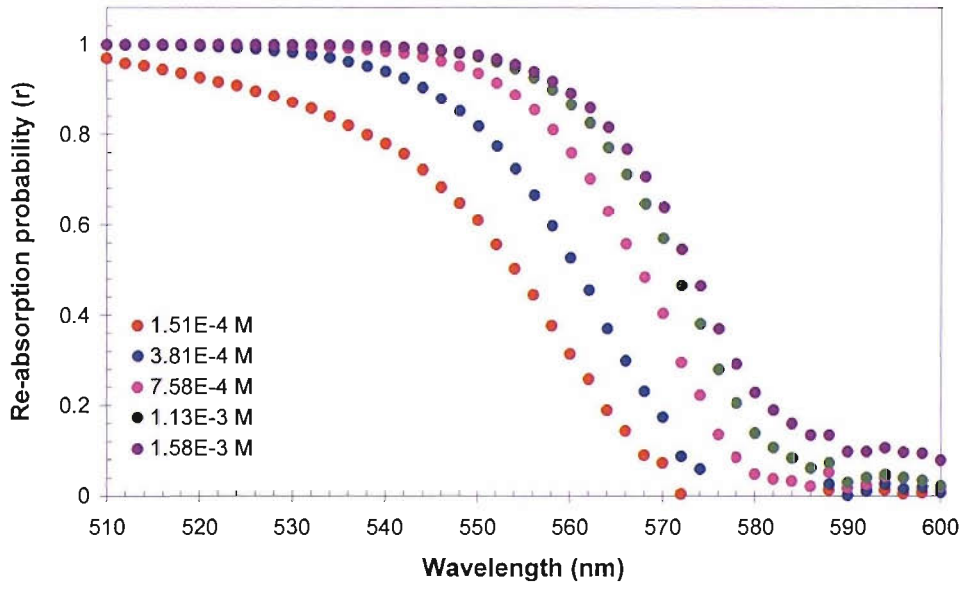

FIGURE 8.18: The correspondence of $r(\lambda)$ with various sample concentrations.

To investigate how the re-absorption losses vary with the concentration of the sample, the parameter R was computed using Eq. 8.8 and then plotted against the concentration (see Fig. 8.19). The 8% positive and negative potential error of the calculated values is also shown. The error was obtained from the average deviation of the $r(\lambda)$ from the WLM plot (see Fig. 8.20).

$$R = \int_0^\infty f_1(\lambda) r(\lambda) d\lambda \tag{8.8}$$

As expected, the re-absorption probability tends to increase nonlinearly with increasing concentration. The loss is approximately within the range of 32% to 60%, which corresponds to the lowest concentration (1.51×10^{-4} M) and highest concentration (1.58×10^{-3} M), respectively.

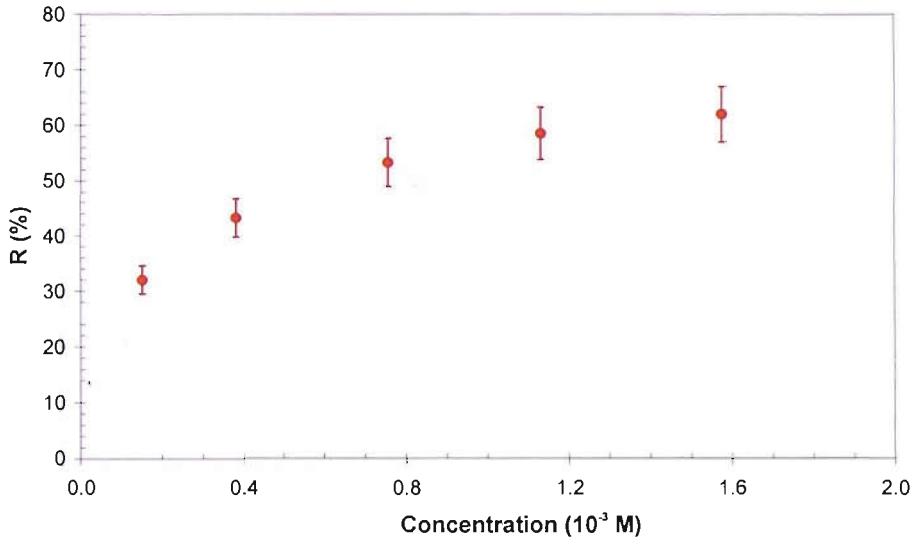

FIGURE 8.19: The dependence of re-absorption probability on concentration. The error bars represent an uncetainty of 8% in the calculated results.

Before discussing further, it is necessary to verify the result obtained from the analysis. The theoretical models (Eqs. 6.24 and 6.26) discussed in section 6.3.1, were employed for this purpose. To compare the analysed results with the theoretical models, $1 - r(\alpha)$ is plotted against αL. The α that was used for this comparison is the effective absorption coefficient of the sample (α_{eff}). It is defined as

$$\alpha_{eff} = \frac{A}{d} ln(10) \tag{8.9}$$

where d is the thickness of the collector and

A is the absorbance.

The factor $ln(10)$ was introduced in the expression since we required the *Napierian* absorption coefficient for this comparison.

Figure 8.20 compares the $1 - r(\alpha)$ obtained from the analysis with that from Eq. 6.26 (WLM model). The results, in overall, are in good agreement with the WLM

curve. The error bars representing the uncertainties for the 1-r and α_{eff}L values are also presented. The vertical error bars were estimated to be ±8% for all points. This uncertainty value represents from the average deviation of the 1-r values from those derived from WLM model. The horizontal error bars were estimated to be ±10%. This ±10% error was estimated from the variation of the α_{eff} values obtained from the absorbance spectra. The variation generally results from (1) the fluctuation of the Xenon light source used in the absorbance measurement and (2) the difference of the film thickness between the reference sample and the test sample.

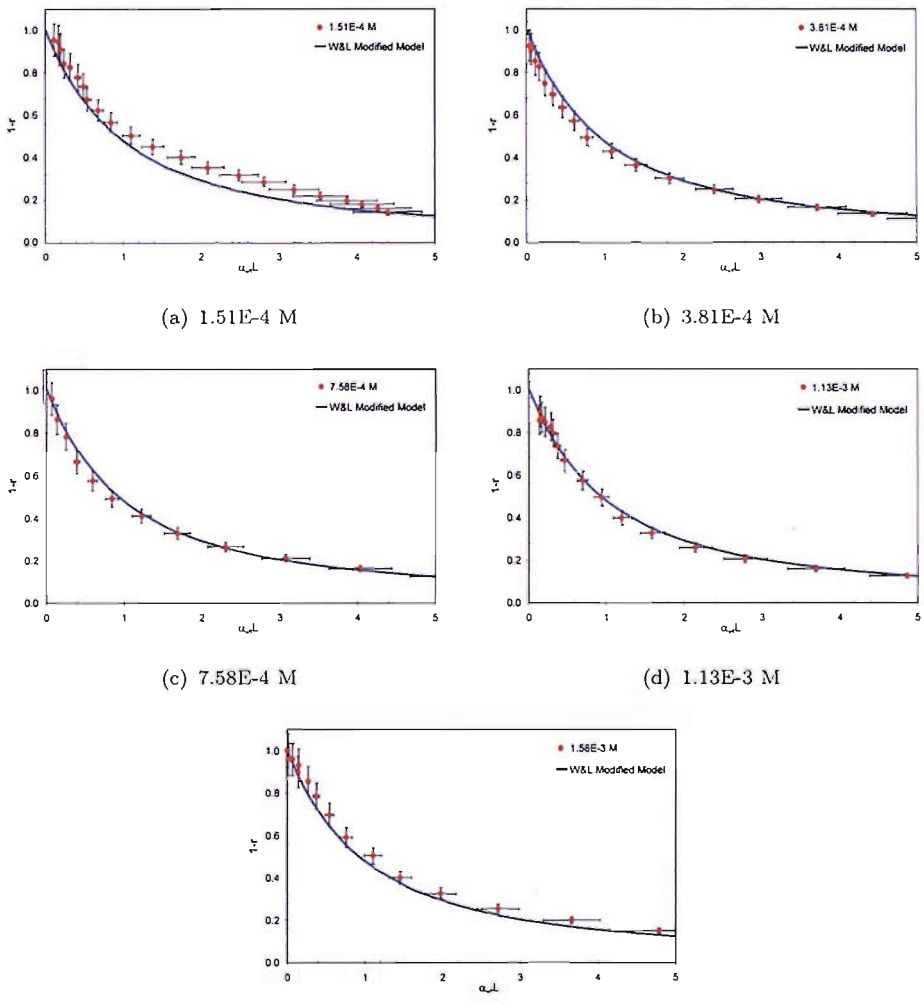

(a) 1.51E-4 M

(b) 3.81E-4 M

(c) 7.58E-4 M

(d) 1.13E-3 M

(e) 1.58E-3 M

FIGURE 8.20: The comparison of $1-r(\alpha)$ obtained from this analysis and Eq. 6.26. The solid line was obtained using Eq. 6.26. The vertical errors were estimated to be ±8% and the horizontal errors were estimated to be ±10%.

Comparing the $1-r(\alpha)$ from the experiment with that derived from Eq. 6.24 (WL model), it is found that the experimental values are higher than the model result.

This is not a surprise as both systems have different optical arrangements. Regarding our measurement system, there is an air gap in between the sample and the optical detector. Therefore, only a fraction of the rays, emitted at an angle less than the critical angle, was detected. As for Weber and Lambe's setup, a silicon solar cell was directly coupled to the collector. With this setup, the fluorescent light emitted at a larger angle can be detected. The emission light seems to have more chance to be re-absorbed by dye molecules. As a consequence, the values of $1 - r(\alpha)$ from the WL model are lower than those from our experiment. This result has a good agreement with the expression presented in [116], which reports the relationship between the re-absorption losses and the average optical path length $\bar{l}$ as shown in Eq. 8.10.

$$1 - r(\lambda) = exp(-\bar{l}/\lambda) \tag{8.10}$$

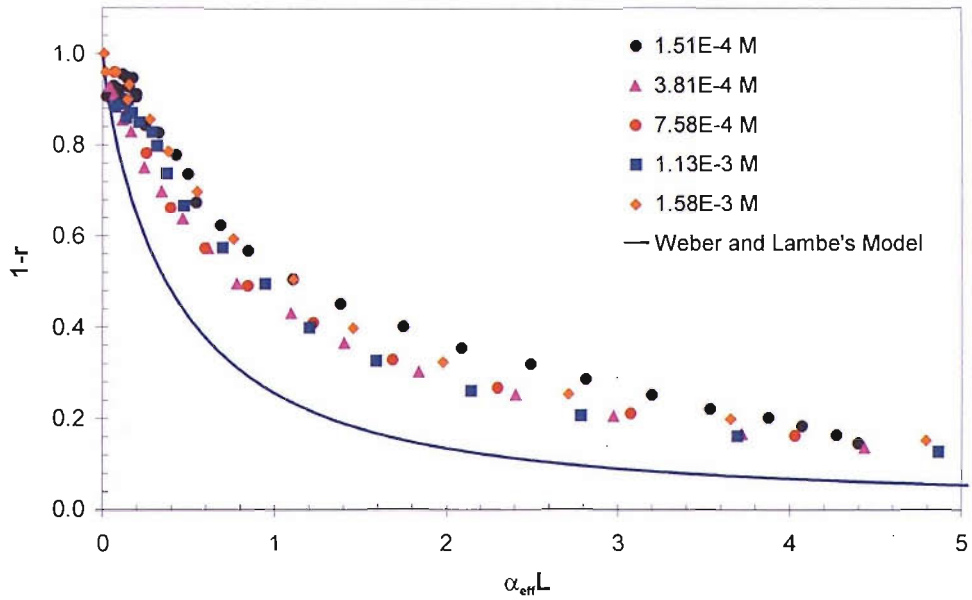

FIGURE 8.21: The comparison of $1-r(\alpha)$ obtained from this analysis and Eq. 6.24. The solid line was obtained using Eq. 6.24.

8.5.3 Collection Efficiency

The intention of this section is to estimate the collection efficiency of Rh6G-based samples when they are integrated with a solar cell as shown in Fig 5.2. To obtain this parameter, the re-absorption probabilities corresponding to this setup $(r(\lambda)_{Mod})$ are

needed. In this analysis, $r(\lambda)_{Mod}$ data were computed using Eq. 8.11.

$$r(\lambda)_{Mod} = \Lambda(\lambda) \times r(\lambda)_{Exp} \tag{8.11}$$

where $r(\lambda)_{Exp}$ are the re-absorption losses obtained from the previous analysis and Λ is a constant factor which is introduced to correct the difference due to the experimental configurations. It is given as

$$\Lambda(\lambda) = \Lambda(\alpha) = \frac{r_{WL}(\alpha)}{r_{Exp}(\alpha)} \tag{8.12}$$

where $r_{Exp}(\alpha)$ and $r_{WL}(\alpha)$ are the re-absorption losses obtained from our analysis and WL model, respectively.

The $r(\lambda)_{Mod}$ were used to determine the Q_C using Eq. 6.22. The results obtained from the computations are presented in Fig. 8.22. The plot shows the drop in Q_C as the concentration increases. The decrease in Q_C is possibly caused by a combination of two effects that were discussed previously. These are:

1. the increase in re-absorption probability because of higher absorbing molecules concentration and
2. the decrease in fluorescence quantum yield, which results from the interactions of the dye molecules at higher concentration (concentration quenching).

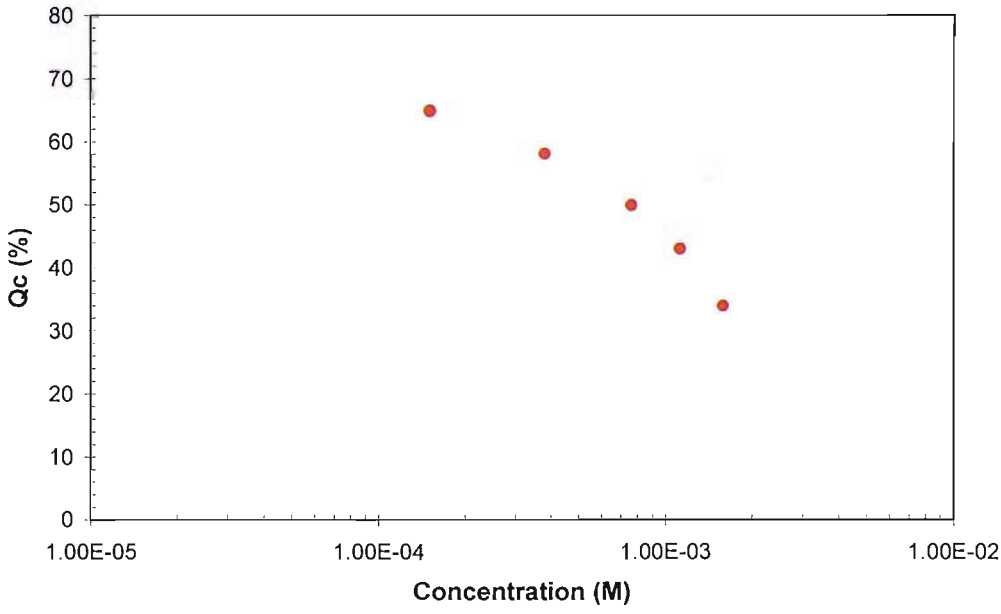

FIGURE 8.22: The dependence of collection efficiency on concentration.

8.6 Efficiency of Fluorescent Collector

So far, the parameters Q_A, Q_C and ϕ_f have been derived. It is now possible to determine the efficiency of fluorescent collectors, η_{FC}, which can be computed using

$$\eta_{FC} = \phi_f Q_A Q_C$$

where the parameter Q_A, Q_C and ϕ_f are obtained from the previous sections.

η_{FC} is plotted against the concentration as shown in Fig. 8.23. It is seen that η_{FC} increases with concentration up to a value of approximately 7.6×10^{-4} M. Above this concentration the efficiency tends to drop. The decrease in η_{FC} above this concentration is caused by the re-absorption loss and also the decrease in fluorescence quantum yield discussed previously. It should be noted that the maximum efficiency is found to be ~22.7%. This efficiency corresponds to a collector with an area 6.76 cm^2 and prepared from the spincoat solution with a concentration of $\sim7.6\times10^{-4}$ M.

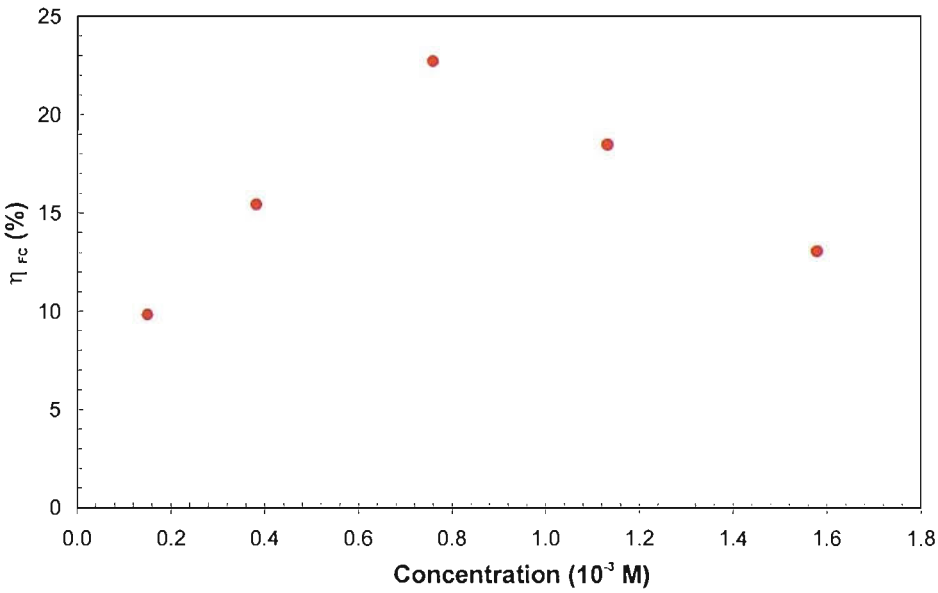

FIGURE 8.23: The dependence of η_{FC} on concentration.

The η_{FC} and also the photon flux gain Φ_G at the edge of the samples are summarised in Table 8.1. It should be noted that the Φ_G values are derived using Eq. 6.30.

TABLE 8.1: The efficiency of the FC and the photon flux gain at the edge

Concentration (M)	$n_{FC}(\%)$	ϕ_G
1.51×10^{-4}	9.9	2.6
3.81×10^{-4}	15.5	4.0
7.58×10^{-4}	22.7	5.9
1.13×10^{-3}	18.5	4.8
1.58×10^{-3}	12.6	3.3

8.7 Conclusion

Fluorescent collectors were fabricated and characterised for their optical properties. The experimental results showed that the prepared samples, which is a Rh6G film coated glass, can absorb light in the visible region, approximately 440 to 570 nm. The fluorescence spectra observed from the edge of the samples are within the range 530-670 nm. The fluorescent intensity per absorbed photon tends to decrease with increasing concentration. In addition, it was found that the peak intensity tends to shift to the longer wavelength region when the absorbance is higher. The causes of these mechanisms are:

1) the emitted photons are self-absorbed by the other molecules within the region where the absorbance and emission spectra overlap and,
2) the fluorescence quantum yield decreases due to quenching of fluorescent material.

We demonstrated that the first generation fluorescence spectra can be obtained from the front surface of the sample with peak absorbance less than 0.07. Although the experiment was also performed to measure the fluorescence spectra from spincoat material (with low concentration) in 1 cm path length cuvette, the method was found not appropriate to obtain the first generation fluorescence spectra. The is because the spincoat material did not become completely solid when the measurement was taken.

The effect of reflectors in the FC performance was also studied. It was found that adding Al-reflectors to the edges and back surface of the collector can help in maximising the intensity of the fluorescence signal. The intensity of the observed spectra was doubled when the Al-reflector was placed underneath the FC. The fluorescent intensity was maximised by a factor of 3 when the remaining edges and underneath of the collector were coupled with the Al-reflectors during the measurement.

The analysis techniques described in Chapter 6 were applied to analyse the experimental results. The major parameters obtained from the analysis are absorption

efficiency, collection efficiency, fluorescence quantum yield, re-absorption probability and efficiency of the fluorescent collectors.

The performance analysis revealed that the absorption efficiency of the prepared samples tends to increase linearly from approximately 16% to 66% as the concentration of the spincoat solution varied from 1.51×10^{-4} to 1.58×10^{-3} M. The re-absorption probability was also found to increase nonlinearly from approximately 32% to 60% as the concentration increases. On the contrary, the fluorescence quantum yield and the collection efficiency tends to drop as the concentration increases. The drop of the yield was clearly observed when the concentration is higher than 7.6×10^{-4} M. The collection efficiency of the samples was found to be approximately 39% to 64%. These results suggested that the maximum efficiency of the collector can be obtained at the optimised concentration. The maximum efficiency and photon flux gain obtained from the fabricated collectors were found to be approximately 22.7% and 5.9, respectively.

Part III

Towards an Integrated Concept

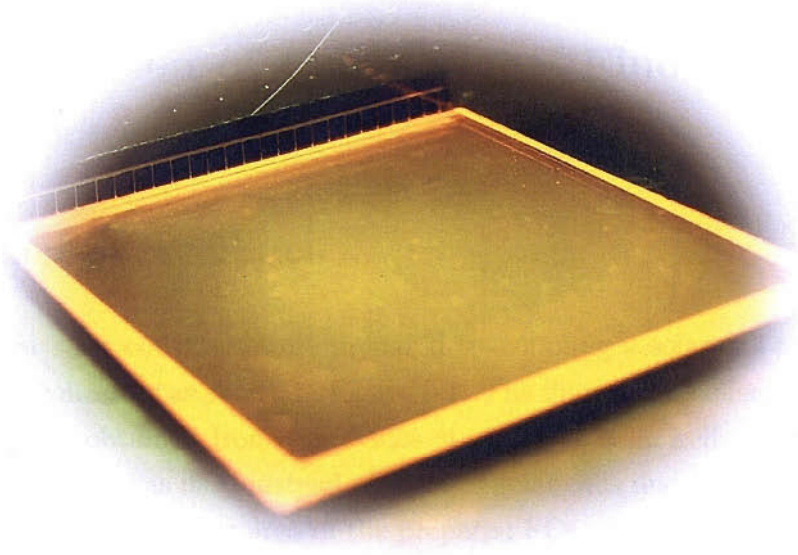

Chapter 9

Development of Fluorescent Solar Collectors

This chapter presents an attempt in developing fluoresent solar collectors based on the outcome from part I and II. The aim of this study is to explore the feasibility of employing the fluorescence dye molecules to improve the energy collection of c-Si solar cells. The chapter is divided into two major sections. The first section deals with the development of the convensional FSC and the second section involves the development of the hybrid thin-film FSC.

9.1 Fabrication of Conventional Fluorescent Solar Collectors

9.1.1 Sample Preparation

The fluorescent solar collectors were prepared by coupling a solar cell to one edge of the fluorescent collectors as shown in Figure 9.1. The fluorescent collectors (FCs) used in this work were obtained from a previous study. The solar cell is c-Si from AEG Telefunken. This cell was used instead of our c-Si solar cells due to its size being large enough to be matched to edge area of the prepared FCs. The Telefunken cell was cut to dimensions of about 2.6×0.2 cm^2 which is approximately twice the edge area of the FCs (2.6×0.1 cm^2). The quantum efficiency of the device was measured using the technique discussed in section 3.3.3. The measured result is shown in Fig. 9.2.

It should be pointed out here that the bigger dimension cell was made in order to facilitate the electrical connections. However, because the cell size is greater than that of the FC's edge area, some area of the cell was not in contact with the edge. This exposed area, hence, was covered with a black tape to eliminate artifacts caused by any external light. The aluminium reflectors (not shown in the figure) were also placed at the remaining edges and the bottom side of the FCs when the measurements were performed. The refractive index matching material was applied at the interface area to minimise reflection losses.

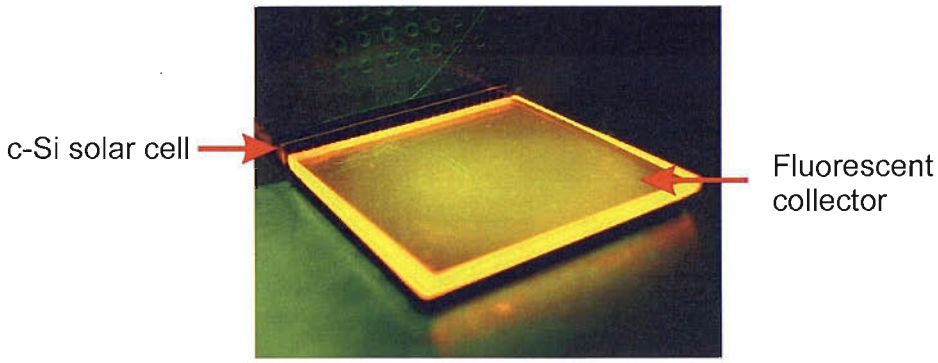

FIGURE 9.1: The prototype of fluorescent solar collector. A c-Si solar cell is coupled to one edge of the fluorescent collector.

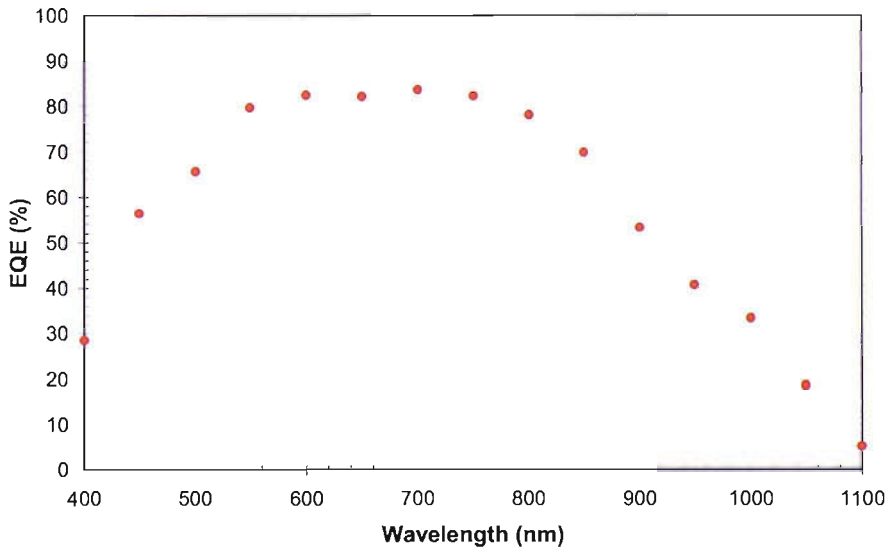

FIGURE 9.2: External quantum efficiency of a Telfunken cell.

9.1.2 Electrical Performance of Fluorescent Solar Collectors

9.1.2.1 Photon Flux Gain

The I-V characteristics of the device were measured using two different setups in order to evaluate how the performance of the solar cell integrated with FC can be improved (see Fig. 9.3). In the first setup, the light was incident directly onto the front surface of the c-Si solar cell, whereas in the second setup, the light was concentrated to the cell using a fluorescent collector. The light source used to excite the sample was a Xenon lamp with 500 nm bandpass filter (10 nm bandwidth). The fluorescent collector used in this study was the sample with concentration of 1.13×10^{-3} M. The efficiency of the sample was 18.5% and the corresponding photon flux gain is 4.8.

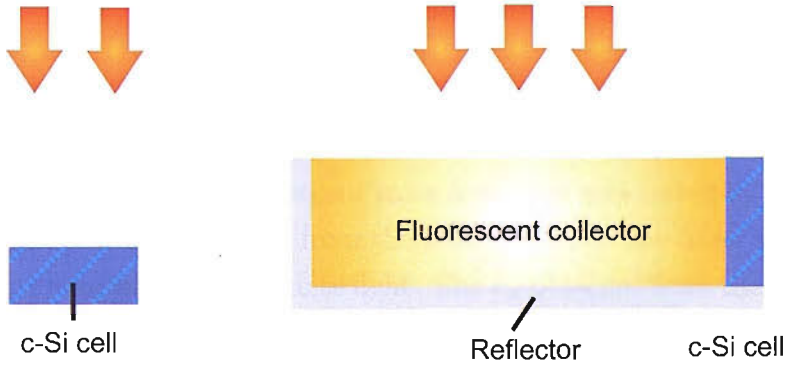

FIGURE 9.3: Experimental arrangements to determine the photon flux gain. Config. I–a solar cell is faced towards the light source. Config. II–a solar cell is coupled to one edge of the fluorescent collector.

The I-V curves obtained from the measurements are shown in Fig. 9.4. It is obvious that the short circuit current density was higher for the cell integrated with the fluorescent collector. This indicates that the photon flux incident on the cell is higher when the fluorescent collector was used. The photon flux gain was found to be 2.6. This gain is approximately half of the photon flux gain calculated from the previous analysis. The decrease of the photon flux gain is possibly caused by the imperfection of the aluminium reflectors used in this experiment. The non-ideal reflectance decreases the number of photons that can be absorbed within the collector plate and also the number of photons available at the edge of the collector.

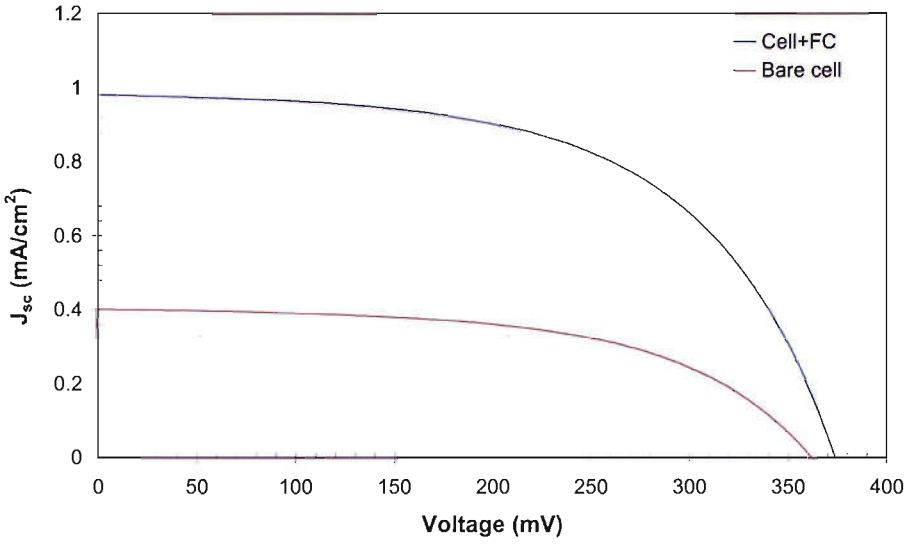

FIGURE 9.4: The I-V characteristics of a bare c-Si solar cell (red line) and fluorescent solar collector (blue line).

9.1.2.2 The Role of Dye Concentration on Electrical Performance

The electrical performance of fluorescent solar collectors was tested by measuring the average I_{sc} (> 50 points) produced from the solar cell when the front area of the FCs were uniformly illuminated with a white light. The I_{sc} obtained from the measurements is plotted against the concentration of the spincoat solution as shown in Figure 9.5.

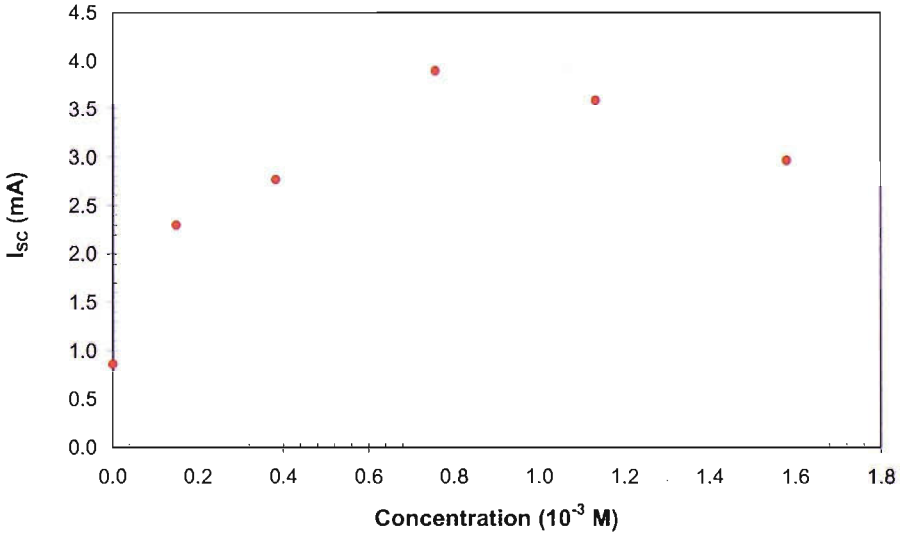

FIGURE 9.5: The dependence of short circuit current on concentration.

It was observed that the I_{sc} increases with concentration up to a value of approximately 7.6×10^{-4} M. Above this concentration the I_{sc} tends to drop. The trend of the results is quite similar to the characteristic of the η_{FC} obtained from the analysis in section 8.6 (see Fig. 8.23). This is not a surprise since the measured current is related directly to the efficiency of the FC and also the photon fluxes available at the edge. Based on the results shown in Table 8.1, it can be seen that the photon flux gain tends to increase with the increase in concentration. The higher photon flux gain was obtained due to the increase of the Q_A. At the concentration higher than $\sim7.6\times10^{-4}$ M, the photon flux gain was found to drop. This is due to the values of the Q_C and ϕ_f dropping to the level where they dominate the efficiency of the FC.

Figure 9.6 illustrates, for example, the spectral current output obtained from a FSC constructed from the FC plate which has the properties shown in Table 9.1. The plot shows for comparison the absorption band of the FC plate and the current output obtained from the cell when it was coupled to the matrix plate. As can be seen from the plot, the current generated from the solar cell is significantly increased in the wavelength region where the Rh6G dye absorbs. The enhancement of the current in this region is due to a fraction of the light being well absorbed by the FC plate and then subsequently re-emitted isotropically. A large amount of the emitted light ($\sim$75%) was trapped inside the FC due to total internal reflection and was delivered to the edge of the FC where it can be detected by the solar cell.

TABLE 9.1: The properties of the FC used to construct the FSC system

Parameters	Value	Unit	Note
Q_A	48.7	%	Obtained from section 8.1
ϕ_f	87.9	%	Obtained from section 8.4
Q_C	53.0	%	Obtained from section 8.5
η_{FC}	22.1	%	Obtained from section 8.6
ϕ_G	5.9	-	Obtained from section 8.6

To understand the characteristic of the spectral current output in more detail, it is essential to consider the arrangements set up to obtain these data as shown in Fig. 9.7. Assuming that the absorption coefficient of the matrix plate is very small and can be neglected, the reflectors are perfect and the edge area of the cell A_1 and the interfaces are completely flat, the current output that can be obtained from the device in config. I (Fig. 9.7(a)) is given by

$$I_1(\lambda_{ex}) = q\Phi(\lambda_{ex})A_1[1 - R_1(\lambda_{ex})]IQE(\lambda_{ex}) \tag{9.1}$$

where A_1 is the edge area of c-Si cell,

$\Phi(\lambda_{ex})$ is the photon flux at wavelength $d\lambda_{ex}$,

$R_1(\lambda_{ex})$ is the reflectance at the PV-air interface at wavelength $d\lambda_{ex}$ and

$IQE(\lambda_{ex})$ is the internal quantum efficiency of the cell at wavelength $d\lambda_{ex}$

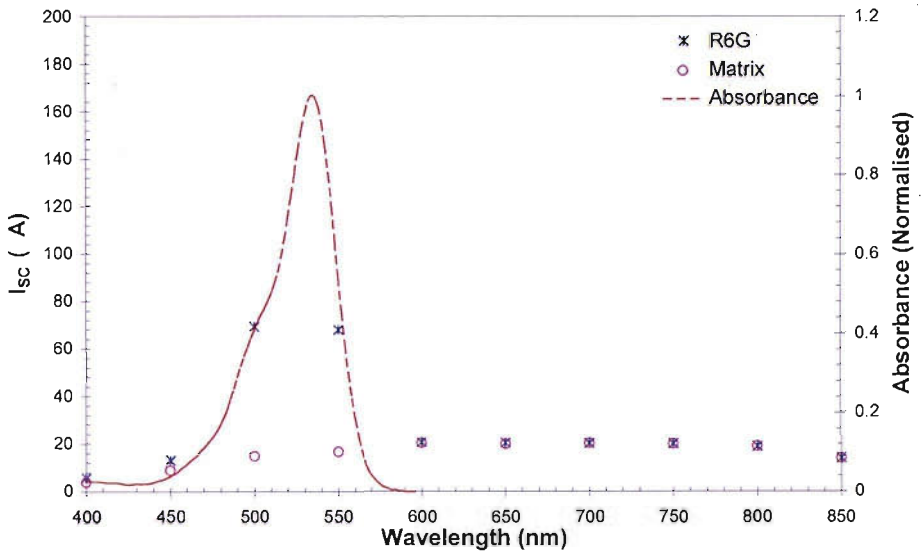

FIGURE 9.6: Spectral current output obtained from a FSC prototype (asterisks). The absorption band of the FC plate (dashed line) and the current output obtained from the cell when it was coupled to the matrix plate (circles) are plotted for comparison.

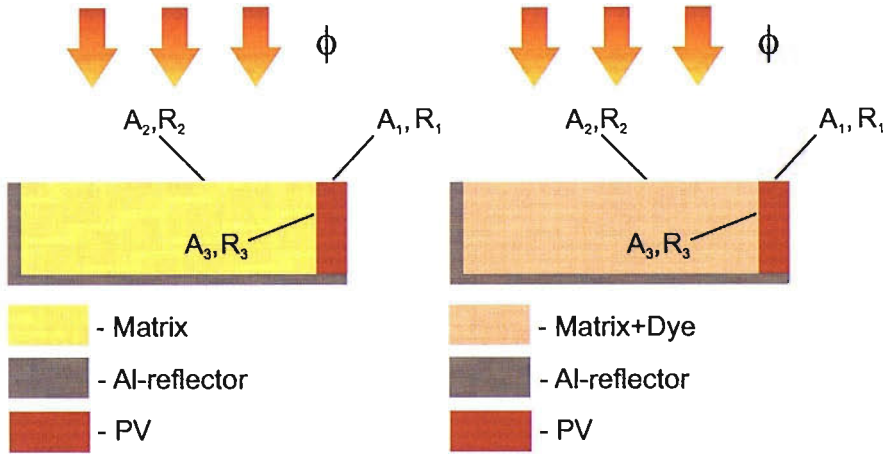

(a) System I: c-Si cell coupled to matrix FC (b) System II: c-Si cell coupled to matrix doped dye FC

FIGURE 9.7: The setup arrangements to obtain the results shown in Fig. 9.6.

The output current that can be obtained from the device in config. II (Fig. 9.7(b)) is composed of two components: the background current and the current from fluorescent light.

$$I_2(\lambda_{ex}) = I_1(\lambda_{ex}) + I_f \tag{9.2}$$

where $I_2(\lambda_{ex})$ is the output current from the cell when the FSC is illuminated with wavelength $d\lambda_{ex}$,
$I_1(\lambda_{ex})$ is the the background current at wavelength $d\lambda_{ex}$ and
I_f is the current due to fluorescent photons emitted at the edge of the FC plate. According to Eq. 6.32, I_f is given by

$$I_f = qA_2\Phi(\lambda_{ex})[1 - R_2(\lambda_{ex})]\left[1 - 10^{-2\alpha(\lambda_{ex})d}\right]\phi_f Q_C[1 - R_3(\lambda_{em})]IQE(\lambda_{em}) \tag{9.3}$$

where A_2 is the front-face area of the collector,
$IQE(\lambda_{em})$ is the internal quantum efficiency of the cell over the emission wavelength,
$R_3(\lambda_{em})$ is the reflectance at the PV-FC interface over the emission wavelength and
$R_2(\lambda_{ex})$ is the reflectance at the air-PV interface at wavelength $d\lambda_{ex}$

The photons flux $\Phi(\lambda_{ex})$ can be expressed in terms of the measured current $I_1(\lambda_{ex})$ as given by

$$\Phi(\lambda_{ex}) = \frac{I_1(\lambda_{ex})}{qA_1[1 - R_1(\lambda_{ex})]IQE(\lambda_{ex})} \tag{9.4}$$

Substituting Eq. 9.4 into Eq. 9.3, we have

$$I_2(\lambda_{ex}) = I_1(\lambda_{ex}) + \left(I_1(\lambda_{ex}) \times \frac{[1-R_2(\lambda_{ex})][1-R_3(\lambda_{em})]}{1-R_1(\lambda_{ex})} \frac{IQE_{em}}{IQE_{ex}} \frac{A_2}{A_1}\left[1 - 10^{-2\alpha(\lambda_{ex})d}\right]\phi_f Q_C\right) \tag{9.5}$$

Using Eq. 9.5, the output current obtained from the device shown in config II can be prediced. Table 9.2 shows the parameters that were chosen to model the output current. The parameters R_1, R_2 and R_3 were derived by considering only normal incident.

The result obtained from the calculation is compared with the measured data as shown in Fig. 9.8. It is seen that there is a significant difference between the experimental result and the calculated value in the region at which the dye absorbs the light. The experimental values are lower, approximately three times. One reason for this mismatch arises from the difference of the reflectance of the reflectors coupled to the edges of the FC that were used in the calculation and the experiment. The calculated result was derived from the perfect reflector; whereas the Al-reflector used to develop the FC prototype has a non-ideal reflectance. The amount of light that can be absorbed within the FC, hence, is not enhanced by a factor of 2 which was assumed in calculation (see Eq. 9.5). Another reason (for this difference) is because of the imperfect coupling at the PV-FC interface. In the calculation, the FC was assumed to be perfectly coupled to the PV cell. This assumption is not applicable for the developed prototype because the refractive index of the RI gel used for the optical coupling is not exactly the same as that of the FC. The edge of the FC which was coupled to the PV may not also be smooth and clear. This problem, therefore, results in some reflection loss at the FC-PV interface. Additionally, it is crucial to point out that the difference of the plots could be attributed to the light scattering inside the FC due to the bulk of surface imperfections. This effect was not taken into account in Eq. 9.5 but may be present in the real situation. To obtain a more realistic curve, the Eq. 9.5 should be modified to take into account the light scattering effect.

TABLE 9.2: The parameters chosen to model the spectral output

Parameters	Value	Unit	Note
R_1	33	%	Estimated using Eq. 2.74
R_2	4	%	Estimated using Eq. 2.74
R_3	18	%	Estimated using Eq. 2.74
ϕ_f	87.9	%	Obtained from section 8.6
Q_C	53.0	%	Obtained from section 8.5
ϕ_G	5.9	-	Obtained from section 8.6
A_1	0.078	cm^2	-
A_2	6.76	cm^2	-
β	1.1	-	Estimated value ($\beta = \frac{IQE(\lambda_{em})}{IQE(\lambda_{ex})}$)

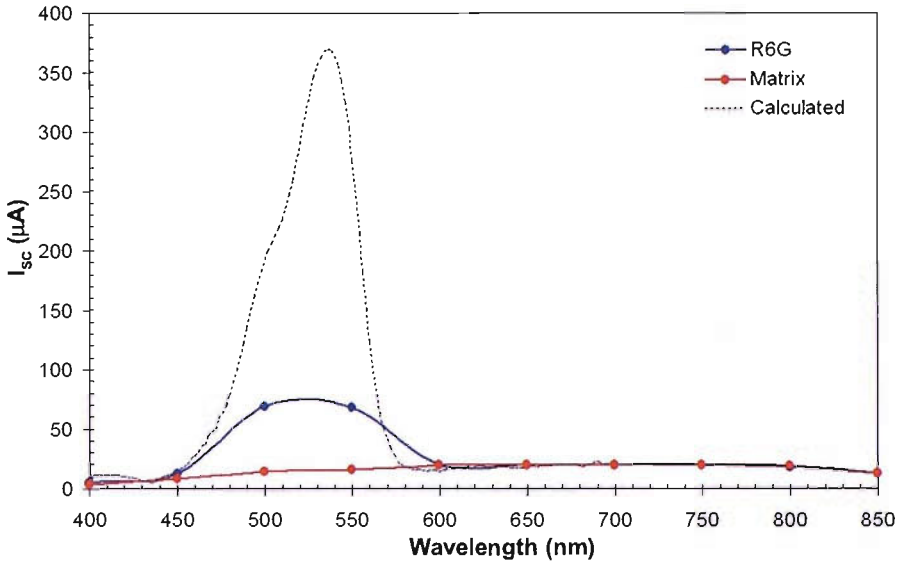

FIGURE 9.8: Spectral response of a developed prototype.

9.2 Fabrication of Hybrid Thin-film Fluorescent Solar Collectors

9.2.1 Design and Fabrication of Thin Film c-Si Solar Cells

This section presents an attempt in developing thin-film c-Si solar cells. The intended application of this batch is to develop thin-film solar cells whose structures can exploit the benefit of the light concentration once they are integrated with the fluorecence material.

9.2.1.1 Device Structure

Figure 9.9 presents the structures of the solar cells, which were designed and fabricated aiming to test the concept of light harvesting using the fluorescence collector. The devices have the trench areas to be filled with fluorescent organic dyes. To study the role of the metal reflector, the structures were also subdivided into two sets: one set has no Al reflector and another set has an Al reflector at the bottom of the trench area.

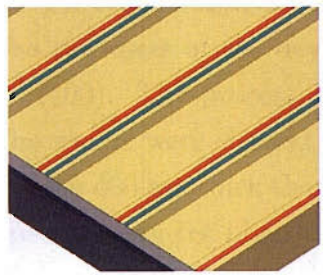

(a) Strip cell

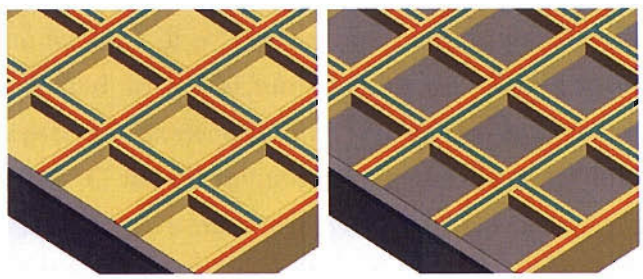

(b) Waffle cell: without Al back reflector

(c) Waffle cell: with Al back reflector

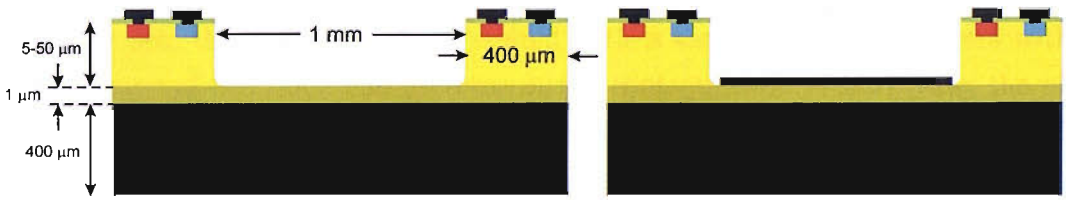

(d) A cross section of thin-film device: without Al back reflector

(e) A cross section of thin-film device: with Al back reflector

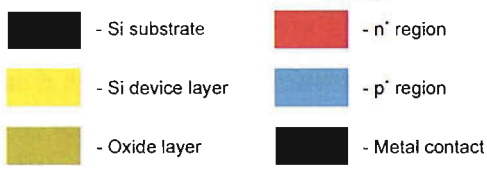

FIGURE 9.9: Structure of thin-film solar cells.

9.2.1.2 Fabrication

We have developed a process for fabricating thin film c-Si solar cells on silicon-on-insulator (SOI) wafers. The devices were fabricated at INNOS Limited, UK. The wafers were purchased from the Si-Mat Ltd, Germany. The device layers of the SOI wafers (100 mm diameter) were FZ type, boron-doped with a doping concentration corresponding to 1-3 Ω·cm. The thickness of the device layer ranged from 5-50 μm and the crystal orientation was (100). The process sequences used to fabricate the cells are shown in Fig. 9.10. The wafers were cleaned using the RCA method. Then, the front surface was passivated with 400 nm thick thermal oxide. To form the emitter area, the oxide windows were opened using the photolithography process. Phosphorus was then diffused at a temperature of 800 °C for 60 minutes using the 'Phosplus' solid source together with a combination of gas ambients: nitrogen, wet oxygen and dry oxygen. Prior to the forming of p^+ region, the thermal oxides were stripped out and the wafers were deposited with 100 nm thick oxide. The photolithography process was then used to open the oxide windows. After this stage, boron was diffused at a temperature of 1050 °C for 30 minutes using the 'Boron Plus' solid source. The emitter contact areas were patterned using the photolithography process. After that, the wafers were split into two sets. The first set of wafers was the structure presented in Figure 9.9(d). The second set was the cells with Al-reflector underneath the trench area (see Fig. 9.9(e)).

In the first set, the wafers were evaporated with a sequence of Ti-Al layers with a total thickness of 600 nm. The patterns of the contacts were defined using the photolithography process. The oxide layer was opened and followed with etching through the device layer using a deep reactive ion etch (DRIE) machine. The process was then followed with the anneal process under H_2/N_2 ambient at temperature around 450 °C for 30 minutes.

In the second set, the trench areas were patterned using the photolithography process, the oxide layer was opened and followed with etching through the device layer using the DRIE machine. The lift-off process was then used to define the contact areas. The photoresists used in this process were PMGI (Polymethylglutarimide) and SPR 220. The PMGI was used as the under layer since it is readily soluble in most standard alkaline photoresist developers and has highly controllable dissolution properties. The SPR 220 was used for the upper layer. The wafers were evaporated with a sequence of Ti-Al layers with a total thickness of 600 nm. The lift-off was performed in NMP

solvent (1-methyl-2-pyrrolidinone). The process was then followed by the anneal process under H_2/N_2 ambient at a temperature of around 450 °C for 30 minutes.

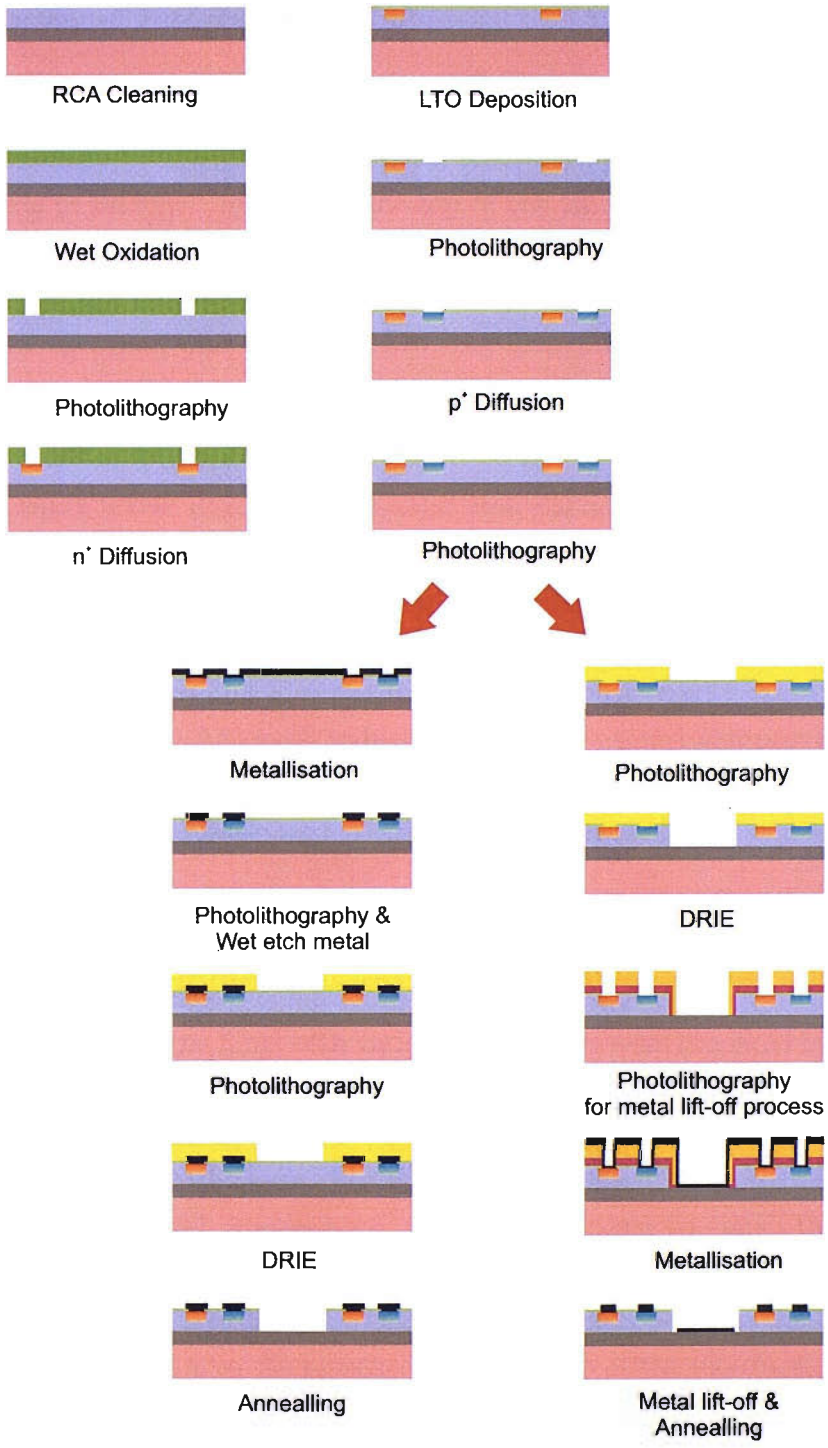

FIGURE 9.10: Process sequence for thin c-Si solar cell based on SOI wafer.

9.2.2 Integration of a Thin Film c-Si Solar Cell with Fluorescent Material

9.2.2.1 Survey of Integration Techniques

To fabricate hybrid thin-film fluorescent solar collectors, we need a method for incorporating the fluorescent material into the trench areas of devices. Ideally, the fluorescent material needs to be filled right up to the top of the trench apertures. Such a material should not cover the front surface of the device since it may inhibit the incident photon flux that can be absorbed by the device. Therefore, prior to the integration of the fluorescent material with the fabricated thin film cells, it is essential to establish a suitable method which meets the above requirements. The aim of this section is to present three major approaches that were investigated throughout this study.

The first approach is spin coating a fluorescent material onto the top surface of the test sample[1]. The spincoat solution was dropped on the top surface of the sample and spun at a constant speed of 3.4 krpm for 1 minute. The coating quality was investigated by an optical microscope (see Fig. 9.11). The result shows that the trench areas were not completely filled and also the front surface of the device was covered with the fluorescent material. Although reducing the coating speed can provide a thicker material in the trench, it results in a thicker film onto the surface of the sample. This approach, hence, is not appropriate to be used since it does not meet our requirements.

The second approach was carried out by sticking strips of the thin polymer film into the trench areas. This method relies on two major process steps. Firstly, the thin film of FC, which has its thickness compatible with the depth of the trenches, needs to be prepared. In this study, the films with various thicknesses were prepared by dropping a certain amount of the polymer solution into the moulds and letting them dry naturally, which takes about 60 minutes. The casting films were gently taken out from the moulds and measured for their thicknesses. The film with a thickness of approximately 10 μm was cut into the strips with dimension of 0.1×1 cm^2 in order to match the dimension of the trench area. The second process step involves the incorporation of the prepared films into the trenches. In order to obtain a good adhesion between the film and the samples, and also to minimise the presence of the air gap at the interfaces, a refractive index matching gel (G608N, Thorlabs, Inc.) was gently spread over the films. The

[1]The test samples that were used in this study were silicon wafers obtained from the development batch. This batch was pre-run to test the DRIE machine and to optimise the conditions used for etching the desgined patterns. The test wafers were etched to form the trench areas (5 to 50 μm) which have a similar pattern as the thin film cells. No diffusion layers or metal contacts were applied to these test structures.

films were then carefully stuck into the trenches. The result shows that the method can be used to fill the fluorescent material better than the previous approach. The front surface of the cell was also not covered by the fluorescent material. However, it is essential to note that the method is non-practicable for the devices with smaller trench dimensions. In addition, this approach is time-consuming compared with the previous approach. This method was, thus, not considered to be used further.

The last approach was the spreading technique. The method was performed by dropping a spincoat material onto the top surface of the cells. The material was then quickly spread with a glass cover slip, which has a smooth and sharp edge. The results revealed that the trench areas were completely filled with fluorescent material right up to the top of the trench apertures. The device areas, however, were covered with a thin layer of the fluorescent film (see Fig. 9.12). Although, this approach does not match some part of the requirements, it was considered to be used further due to its ease of use and simplicity.

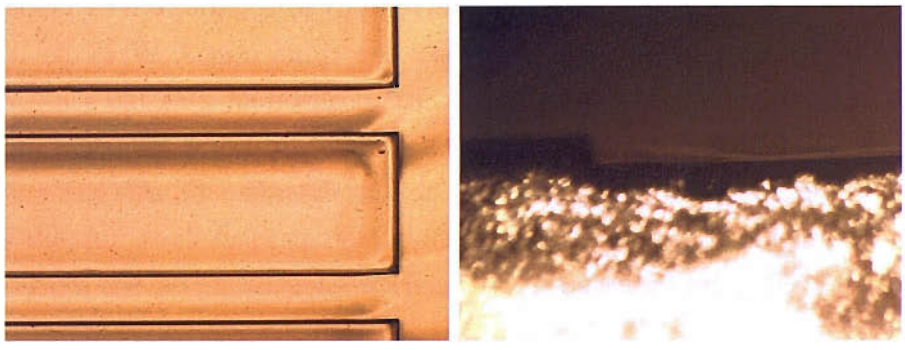

(a) Top view (b) Side view

FIGURE 9.11: Optical image of a sample prepared by spin-coating technique.

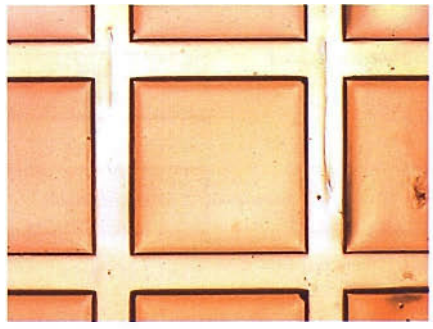

FIGURE 9.12: Optical image of a sample prepared by spreading technique.

9.2.2.2 Sample preparations and Characterisations

To study the performance of the hybrid thin-film FSC, a 10 μm thick c-Si solar cell, which has the structure shown in Fig. 9.13, was chosen to evaluate the concept. The device was coated with a solution of the Rh6G using the spreading technique. The Rh6G solution with concentration of approximately 1.1×10^{-3} M was prepared based on the method discussed in section 7.2.

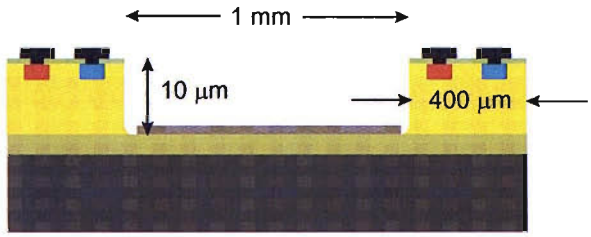

FIGURE 9.13: Dimension of thin film c-Si cell.

The electrical characteristics of the device were measured using the setup shown in Fig. 9.14. A 75 W Xenon lamp was used as a light source. The light was guided to the entrance slit of a monochromator (Bentham M300) via an optical fiber. The light is diffracted by a grating and monochromatic light leaves the monochromator through the exit slit. The monochromatic light was guided to illuminate over the front surface of the sample through an optical fiber and a combination of lenses. The current generated from the device at each wavelength was measured using the data acquisition unit.

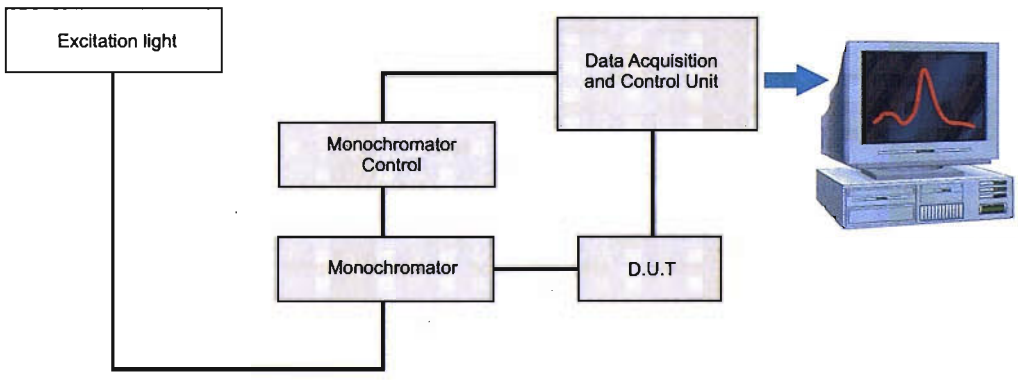

FIGURE 9.14: Spectral response measurement system developed from Bentham spectrometer.

9.2.2.3 Preliminary Results and Discussions

Figure 9.15 presents the spectral output of the device before and after incorporating with the matrix and fluorescent materials. Unfortunately, it was found that the response of the device was slightly lower when the fluorescent material was integrated to the device. The reason of this non-improvement is that the concentration of dye was probably too high to achieve the observable Q_C for this geometrical structure. Another reason may be due to the optical losses that were introduced after the fluorescent material was incorporated with the cell. As mentioned previously, the front surface of the cell was covered by the thin layer of the fluorescent material. Hence, it is possible that the thin layer film may reduce the amount of the incident photon flux.

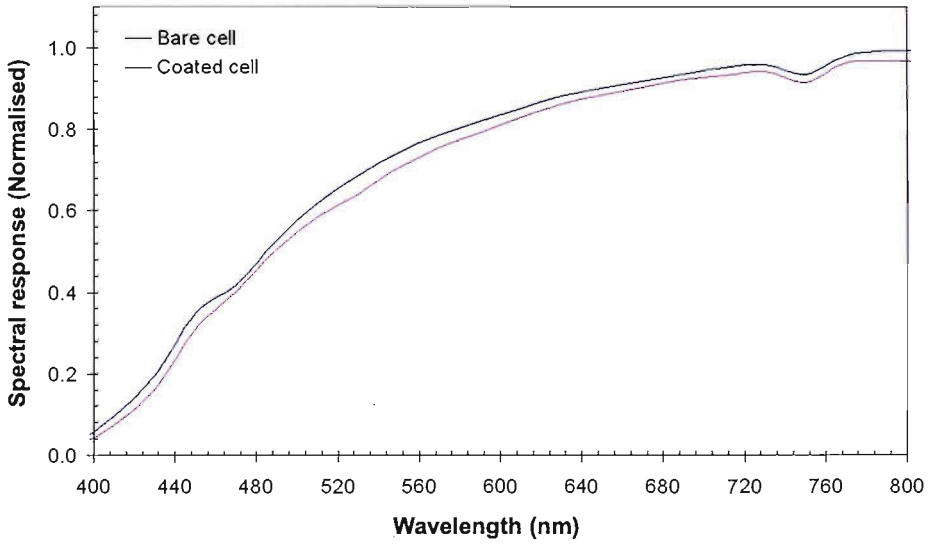

FIGURE 9.15: The spectral response of a wafer based c-Si solar cell before and after being coated with a fluorescent material.

Although, the decrease of dye concentration can lead to higher Q_C, it also results in a lower absorption efficiency. Hence, to gain a benefit from the thin film structure, it is essential to find a solution to enhance the performance of the FC material (both Q_A and Q_C) before the material is integrated with the device. Two possible methods that are currently investigated are:

- the use of fluorescent material with a broader absorption band and
- the use of multiple dyes to absorb more light.

The latter approach can be realised by mixing the dyes in the same plate or by using a stack arrangement. The preliminary results are presented in the following sections.

9.2.2.4 Improved FC Performance with a Mixture of Dyes

This section aims to demonstrate how the performance of FSC could be improved by using a mixture of dyes to absorb more light. The FCs with properties shown in table 9.3 were considered in this study.

TABLE 9.3: A set of square FC plates prepared for this study

Collector size (cm^2)	Fluorescent material	Concentration (M)
2.6×2.6	Cou540A	1×10^{-3}
2.6×2.6	Rh6G	1×10^{-3}
2.6×2.6	Cou540A: Rh6G	1×10^{-3}:1×10^{-3}

The absorbance and edge fluorescence spectra were measured with the measurement systems discussed in section 7.3. The excitation sources for the fluorescence measurement were a high power light emitting diode (LUXEON STAR 3 W) with a maximum peak at 442 nm and a 75 W Xenon lamp.

From the absorbance spectra of the collectors (see Figure 9.16), we have observed the following features:

- peaks at 420 nm for the donor dye (Cou540A) and at 530 nm for the acceptor dye (Rh6G),
- a spectrum of the mixture exhibits peaks from all the components in the mixture as a superposition of the individual spectra,
- absorbance of the donor dye is much lower than that of the acceptor dye.

Figure 9.17 illustrates the edge fluorescence spectra of the FCs when they were excited with the high power LED. It was found that the donor peak disappeared while the acceptor intensity in the mixed sample was enhanced. From this we can conclude that there was an energy transfer from the Cou540A to the Rh6G.

This preliminary result suggests that there is a potential to enhance the absorption efficiency by using multiple dyes. Further study, however, is required to obtain an insight into the principle of operation of the multiple dye system and also to optimise the properties of the prepared mixture.

9.2.2.5 Improved FSC Performance with a Stack Arrangement

The other way that could enhance the efficiency of the FSC is a stack method which was first proposed by Goetzberger *et al.* [11]. The concept of the method is to stack

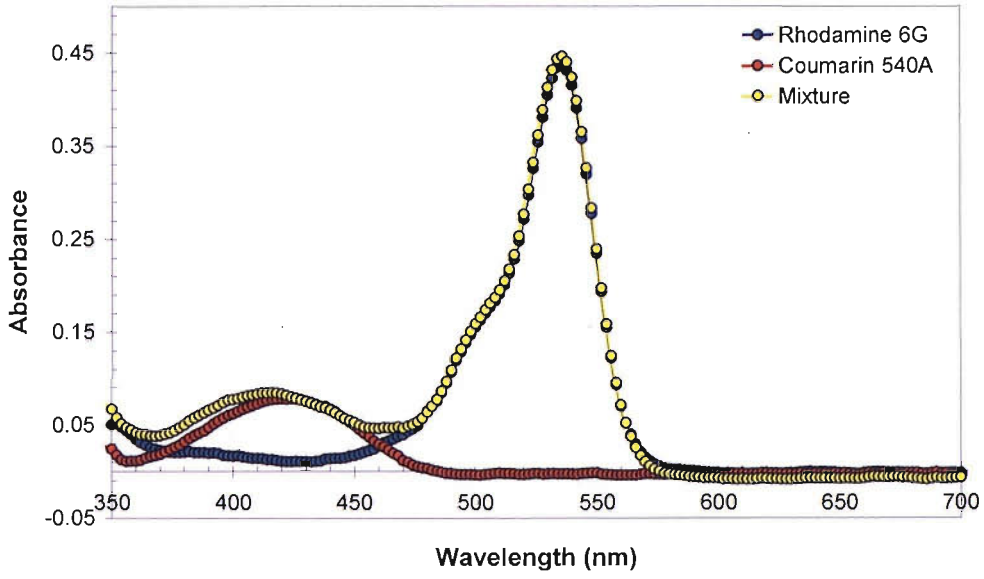

FIGURE 9.16: The absorbance spectra of Coumarin540A, Rh6G and Mixture films.

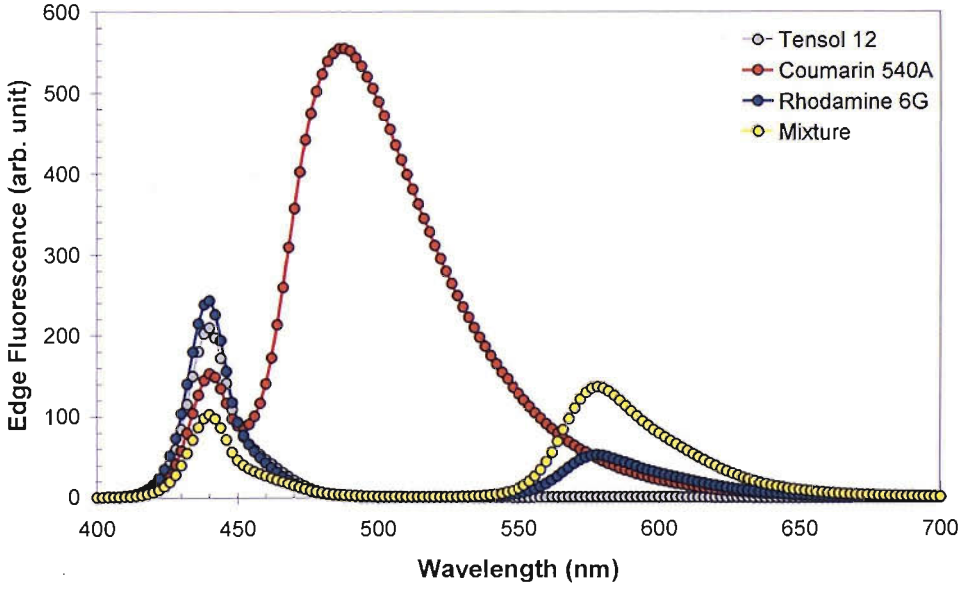

FIGURE 9.17: The fluorescence spectra of Cou540A, Rh6G and Mixture films.

the fluorescent collectors in such a way that the sunlight falls first on material having the largest bandgap. Photons, which are not absorbed in the first plate, are transmitted to the second plate, which then absorbs the remaing portion of photons. These selective absorption processes continue through the final collector plate, which has the smallest bandgap. In this study, the concept was verified by arranging the FC plates in such a way that the top plate absorbs the shortest wavelength radiation, whereas

the lower plates absorb longer wavelengths (see Fig. 9.18).

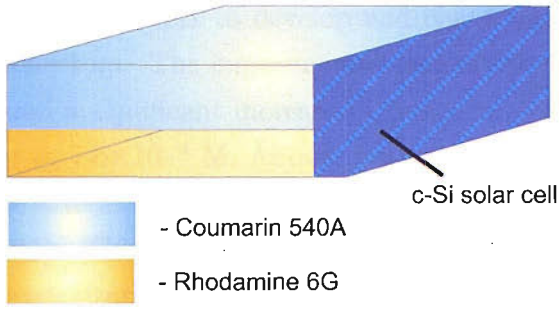

FIGURE 9.18: FSC system with a stack arrangement of collector plates.

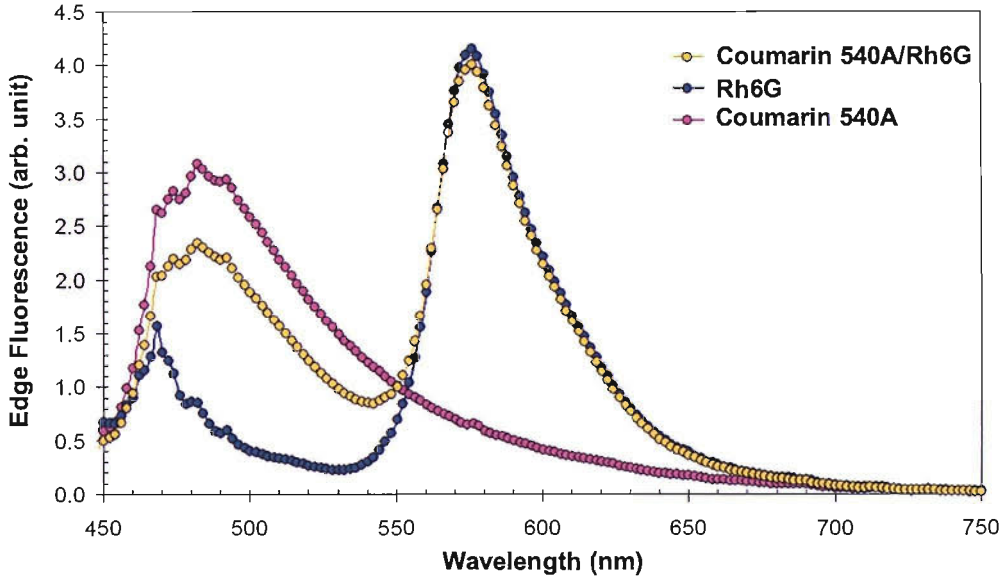

FIGURE 9.19: Comparing edge fluorescence of Coumarin540A, Rh6G and Coumarin: Rh6G in Stack under white light excitation.

The measurement results obtained when the system was illuminated with white light are illustrated in Fig. 9.19. Unlike the previous approach, the results show a broader range of emission spectra. By considering the spectral shape, it is seen that the spectra of the mixture exhibits peaks from all the components in the mixture, i.e., at 485 nm for Cou540A and at 580 nm for the Rh6G. The result suggests that this approach could also lead to an enhancement in efficiency of the fluorecent collectors.

9.3 Conclusion

This chapter discussed the attempts to develop and characterise the performance of the fluorescent solar collectors. The experimental results for the structure based on conventional cells showed a significant increase in the current output as the dye concentration increases up to 7.6×10^{-4} M. Above this concentration, the current output tends to drop. This characteristic is similar to the efficiency trend line of the fluorescent collectors (see Fig. 8.23). This result confirmed the validity of theoretical methods developed to study the performance of the FCs. Based on the current spectral output, we observed a significant enhancement of the current over the region where the dye absorbs the light. The current gain was found to be approximately three times lower than the theoretical value. It seems that the cause of the disagreement is due to the imperfection of the developed prototype such as the non-ideal reflectance of the reflectors, the effects of the roughness at the interface and also the absorption loss inside the matrix material.

Thin film c-Si solar cells were also designed and fabricated to test the idea of hybrid thin-film FSC. The preliminary results showed no improvement in the current spectral output when the device was integrated with the fluorescent material. The reason for this may be that the concentration of dye is too high to achieve the observable Q_C for this geometrical structure. This could also be due to the optical losses that were introduced because the front surface of the cell was covered with a thin layer of the fluorescent material.

In addition, we studied the feasibility of the use of multiple dyes and the stack arrangement to improve the FSC performance. Preliminary results showed that there is potential to enhance the efficiency of the FSC based on these approaches. However, further optimisation is required to obtain an insight into the principle of operation of these systems.

Chapter 10

Conclusions and Suggestions for Further Work

10.1 Conclusions

This thesis describes work carried out during four and half years of a PhD program, the main focus being the development of fluorescent solar collectors, including both the collector itself and the crystalline silicon solar cell to provide a conversion unit to electricity. Three principal tasks were performed during the course of the research.

The first task was to develop and study the performance of c-Si solar cells. The requirement was to obtain some experience in device processing and to gain a deeper insight into the principles of c-Si solar cell operation.

The devices were designed to have the $n^+/p/p^+$ structure and were fabricated at Southampton University Microelectronic Center (SUMC). Special attention was paid to the emitter layer since it can absorb a large fraction of sunlight. In the study, the devices were processed under various diffusion conditions to obtain emitter layers with different junction depths.

The doping profiles of the emitter areas were characterised using both SIMS and SRP techniques. The electrical performance of the devices was also characterised using the I-V measurement system and the spectral response measurement system. The SIMS study revealed the presence of a heavily doped region near the front surface of the device. This heavily doped region was believed to form a 'dead layer' in the emitter and was a major cause for the low quantum efficiency of the cells in the short wavelength region.

To understand the performance of the devices in more detail, we developed a theoretical model to analyse the collection efficiency of the minority carriers. Analysis of the results revealed that the poor response of the cell at short wavelength was due to a high front surface recombination velocity (10^6 cm/s). The surface recombination velocity at the back surface was found to be quite low (250 cm/s). To improve the efficiency of the devices, it was suggested that the diffusion process used to prepare the emitter needed further development to eliminate the 'dead layer'.

The second task of the research was the development of fluorescent collectors and the study of their optical performance. A method to prepare the fluorescent collectors was developed and used to fabricate samples for our study. A range of measurement systems and characterisation techniques were also established and successfully used to study the performance of the prepared collectors.

The results showed that the fluorescent collectors prepared from Rh6G dye can absorb light in the visible region, approximately 440 to 570 nm and emit light within the range 530 to 670 nm. The absorbance of the samples was found to increase linearly with increasing concentration of the dye molecules. The absorption efficiencies, however, were found to be quite low due to the narrow absorption band of the dye.

The first generation fluorescence spectra and also the edge fluorescence spectra of the FCs were characterised. Two approaches were used to determine the first generation fluorescence spectra. The first approach was the measurement of the fluorescence spectra emitted from the front surface of the low absorbance samples. The low absorbance samples were required in order to minimise the re-absorption loss. Another approach is the measurement of fluorescence light emitted from low concentration spincoat material in a 1 cm path length cuvette.

It was discovered that the first generation fluorescence spectra can be obtained from the front surface of the sample with a peak absorbance less than 0.07. The first generation fluorescence spectra could not be obtained from the latter approach. This was because the fluorescence spectra were influenced by the change in solvent nature or composition. The results revealed a shift of the fluorescence spectra as the spincoat material changed from liquid to solid form. It is the author's view that this approach is not applicable to obtain the first generation fluorescence spectra because the composition of the material in the cuvette is not similar to those of the FCs. Hence, to obtain the first generation fluorescence spectra of the FCs, the first approach is suggested.

The edge fluorescence spectra indicate that the number of photons, which are guided to the edges of the collector depends strongly on the concentration of the dye. The effect

of the dye concentration was noticed from the distortion of the emission spectra as the concentration increases. The peak intensity also dropped when the concentration exceeded 7.6×10^{-4} M. This behavior is caused by two major effects:

1) the dye molecules are self-absorbed by the other molecules within the region where the absorbance and emission spectra overlap and,

2) the fluorescence quantum yield is decreased due to quenching of fluorescent material.

To understand the photon transport losses within the FC plate, a model called 'Two Photon Fluxes' was developed within our group and used to determine the re-absorption probability and also the collection efficiency Q_C of the prepared samples. The results obtained from the analysis revealed that the re-absorption mechanism has a major influence on Q_C. This effect becomes dominant as the concentration of the dye increases. This result indicates that the best performance of the FCs can be obtained at an optimum concentration.

The final task of the research involved the development and study of the performance of integrating systems consisting of a fluorescent solar collector and a crystalline silicon solar cell. Two different structures of FSCs were used for this purpose. FSCs manufacturated by sawing from conventional silicon solar cells and waffle shaped hybrid thin-film FSCs which were designed and fabricated specially as part of a fluorescent collector system. Both structures were subjected to extensive electrical characterisation.

The experimental results for the structure based on conventional cells showed a significant increase in the output current as the dye concentration increased up to 7.6×10^{-4} M. Above this concentration, the output current tends to drop. This characteristic is similar to the efficiency trend line of the fluorescent collectors (see Fig. 8.23). This result confirms the validity of theoretical methods developed to study the performance of the FCs. Based on the current spectral output, we observed a significant enhancement of the current over the region where the dye absorbs the light. The current gain was found to be approximately three times lower than the theoretical value (see Fig. 9.8). It seems that the cause of the disagreement is due to the imperfection of the developed prototype such as the non-ideal reflectance of the reflectors, the effects of the roughness at the interface and also the absorption loss inside the matrix material.

The second type of structure, novel thin film c-Si solar cells with structures that exploit the benefit of light concentration, was successfully fabricated. A method for integrating FC materials with this novel device structure was also developed and used

to incorporate the FC layers into the trench area of the device. The preliminary results showed no improvement in current spectral output. The reason for this may be that the concentration of dye is too high to achieve an observable Q_C for this geometrical structure. This could also be due to the optical losses that were introduced because the front surface of the cell was covered with a thin layer of the FC material. Further optimisation is required in order to obtain a higher current gain from this novel device structure.

10.2 Suggestions for Further Work

10.2.1 c-Si Solar Cell

To improve the efficiency of the c-Si solar cell, the heavily doped region near the front surface of the device needs to be eliminated. The diffusion process used to prepare the emitter layer has to be modified and developed further. This could be done in two ways:

- introducing a drive-in process after the Phosphorus diffusion,
- lowering the temperature that was used to diffuse the Phosphorus dopant with an additonal drive in process step.

Note that the development of the diffusion process was subsequently pursued further by one of our colleagues, Stuart Boden. The preliminary results show that the emitter profile can be improved by using a lower diffusion temperature (800 °C, 60 minutes) together with a drive-in process (1000 °C, 30 minutes) [117].

10.2.2 Fluorescent Collector

The efficiency of the fluorescent collectors needs to be improved. This could be done by

- using a fluorescent material with a broader absorption band,
- employing fluorescent material with a larger Stokes shift and with high fluorescence quantum yield,
- employing a photonic band stop filter to prevent the loss of the emission light through the escape cone,
- use of multiple dyes to absorb more light.

The latter approach can be realised by mixing the dyes in the same plate or by using a stack arrangement. The preliminary results suggest that there is a potential to enhance the absorption efficiency by using multiple dyes. Further study, however, is required to obtain an insight into the principle of operation of the multiple dyes system and also to optimise the properties of the dyes that will be chosen to develop the system.

Appendix A

Correction of Fluorescence Spectra

The shape of fluorescence spectra were corrected by the use of secondary emission standard. To obtain the corrected spectra, a Coumarin 153 (CAS 53518-18-6), was considered as dye material. This dye was employed as a standard fluorophor since it has the following properties [107, 118]:

- High quantum yield
- Emission spectra independent of excitation wavelength
- Good photochemical stability in solution
- Broad wavelength emission with no fine structure
- Isotropic emission.

The sample was prepared to have the concentration of 1E-6 M (in Methanol) and was contained in a 1 cm path length quartz cuvette. The right angle detection (see section 7.3.2.3) was used to obtained the correction factors. The fluorescence spectra of the sample was collected and compared to its standard spectrum (see Table A.1) [118]. The spectral responsivity or the emission correction factors were obtained using Eq. A.1 [118].

$$\frac{1}{CF(\lambda_m)} = \frac{J(\lambda_m)}{F(\lambda_m)} \tag{A.1}$$

where $CF(\lambda_m)$ is the correction factor,
$J(\lambda_m)$ is the uncorrected spectrum and
$F(\lambda_m)$ is the technical spectrum. It was obtained from Table A.1.

The correction factors obtained from this measurement were used to correct the shape of the emission spectra.

TABLE A.1: Standard spectrum of Coumarin 153 [107]

λ (nm)	**Value**	CF	**λ (nm)**	**Value**	CF	**λ (nm)**	**Value**	CF
486	0.118	0.746	552	0.929	1.071	618	0.355	1.682
488	0.142	0.745	554	0.914	1.082	620	0.341	1.672
490	0.169	0.756	556	0.898	1.098	622	0.328	1.652
492	0.200	0.768	558	0.884	1.107	624	0.315	1.663
494	0.235	0.774	560	0.867	1.119	626	0.303	1.680
496	0.274	0.798	562	0.852	1.129	628	0.292	1.677
498	0.315	0.809	564	0.835	1.141	630	0.280	1.668
500	0.360	0.818	566	0.818	1.154	632	0.269	1.664
502	0.407	0.827	568	0.801	1.168	634	0.258	1.670
504	0.458	0.842	570	0.785	1.188	636	0.248	1.663
506	0.509	0.842	572	0.768	1.217	638	0.239	1.694
508	0.560	0.849	574	0.750	1.231	640	0.229	1.693
510	0.613	0.858	576	0.729	1.251	642	0.219	1.706
512	0.665	0.865	578	0.712	1.276	644	0.211	1.717
514	0.715	0.872	580	0.690	1.280	646	0.204	1.731
516	0.762	0.880	582	0.672	1.287	648	0.195	1.732
518	0.806	0.889	584	0.653	1.304	650	0.188	1.759
520	0.847	0.901	586	0.634	1.312	652	0.180	1.804
522	0.882	0.912	588	0.615	1.320	654	0.173	1.830
524	0.914	0.932	590	0.596	1.346	656	0.166	1.894
526	0.941	0.948	592	0.576	1.374	658	0.159	1.924
528	0.962	0.964	594	0.557	1.391	660	0.152	1.965
530	0.979	0.979	596	0.538	1.412	662	0.146	2.020
532	0.990	0.991	598	0.518	1.446	664	0.140	2.023
534	0.997	1.001	600	0.501	1.473	666	0.134	2.100
536	1.000	1.015	602	0.483	1.512	668	0.129	2.186
538	1.000	1.030	604	0.465	1.557	670	0.124	2.295
540	0.996	1.034	606	0.447	1.599	672	0.118	2.321
542	0.991	1.042	608	0.430	1.635	674	0.113	2.338
544	0.981	1.045	610	0.414	1.678	676	0.108	2.301
546	0.970	1.042	612	0.398	1.689	678	0.104	2.274
548	0.958	1.049	614	0.383	1.691			
550	0.944	1.061	616	0.368	1.682			

Appendix B

Instrumentation for Fluorescence Spectroscopy

A fluorescent molecule absorbs light at one wavelength and, in turn, emits light at a longer wavelength. To determine these absorption and emission spectra, the instrument called a spectrofluorometer is generally used. Figure B.1 illustrates the major components of the instrument.

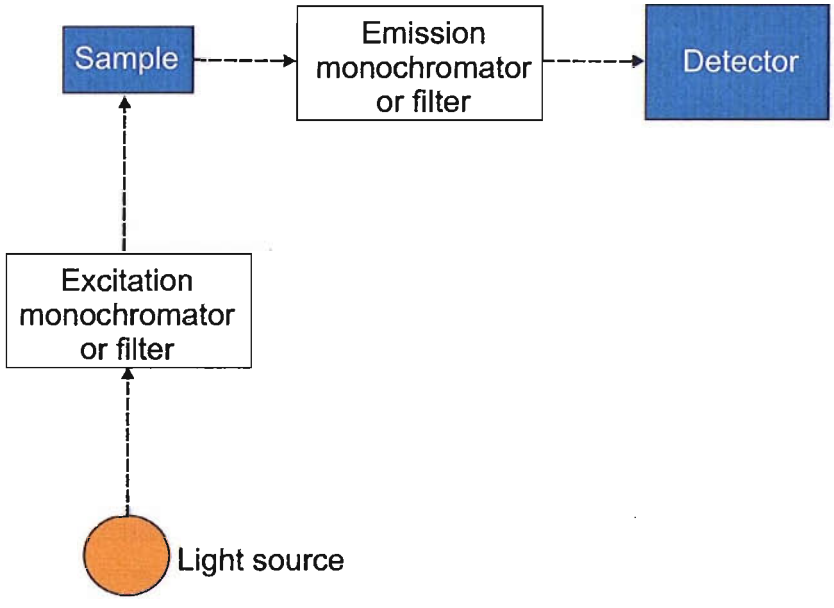

FIGURE B.1: Schematic diagram of a typical spectrofluorometer.

B.1 Light sources

The type of light sources required in fluorescence spectroscopy will primarily depend on whether excitation or emission spectra are being measured. Measurement of fluorescence excitation spectra requires a source which emits a high-intensity smooth continuous source that covers the range of excitation wavelengths.

The simple and cheapest lamps are those of the incandescent type. The lamps generate light by passing an electric current through a thin, filament wire until the wire is white-hot. These give continuous spectra which correspond to the temperature of the wire. Although the lamps can be used for excitation in the visible and infra-red regions, they are of little use for wavelength less than 450 nm. Their output in the UV region is relatively low and this restricts thier use with UV-absorbing fluorophores.

To date, the most versatile light sources commonly used are the arc lamps. These lamps consist of two electrodes typically made of tungsten, which are separated by a gas. When an electric current of sufficient intensity passes through the electrodes, the gas is inonized to a plasma which acts as an electrical conductor. The spectrum of the light depends on the gas contained in the bulb.

B.2 Filters and Monochromators

Since the typical light sources provide continuous spectra over wide wavelength ranges, it is then necessary to have a monochromator or filter to isolate an appropriate narrow spectral range from the sources.

B.2.1 Filters

Filters are the simplest and most efficient optical element that are used to reduce the spectral range (bandpass, cut-off and interference filter) or radiant power of incident radiation (neutral density or attenuance filter) upon transmission of radiation. They are at present available in many types. In this section, we will discuss only two main types of filters: colour filters and inteference filters.

The colour filter, also called the absorption glass, is the most widely used type of filter in fluorescence analysis. It works by attenuating light only based on the absorption effect, so the spectral performance is dependent on the physical thickness of the glass.

Increasing the thickness will increase the blocking level but also reduce the peak in band transmission. Therefore, the optimum thickness value must be determined.

The second type are inteference filters which are made by stacking thin layers of materials onto a glass substrate. The reflections created at each interface between the layers combine through wave interference to selectively reflect some wavelengths of light and transmit others. Examples of filters that are designed using interference coatings are bandpass, shortpass and longpass filters.

■ Bandpass filters

They are denoted by their center wavelength and bandwidth. The center wavelength is the arithmetic mean of the wavelength at 50 % of peak transmission. The bandwidth is specified as the Full filter Width at Half the Maximum peak transmission (FWHM) (See Fig. B.2).

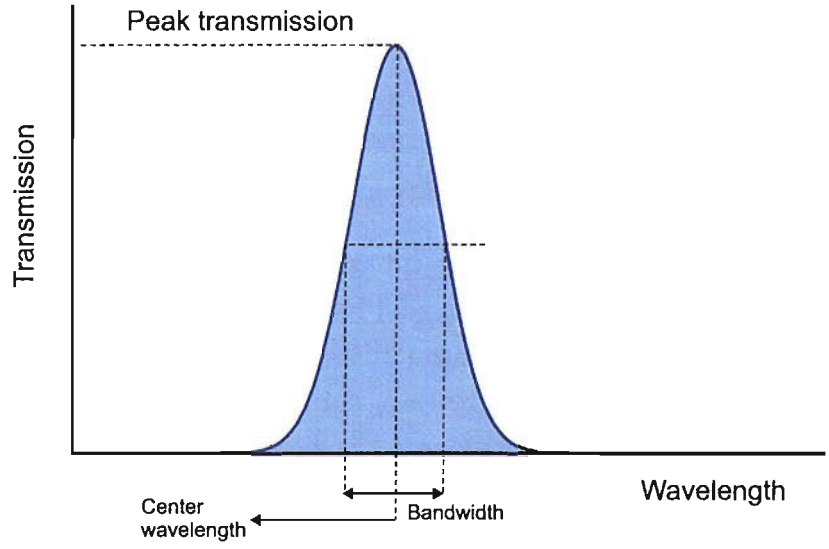

FIGURE B.2: Nomenclature for transmission characteristics of the bandpass filter.

■ Longpass and shortpass filters

Long pass filters and short pass filters are interference filters, which provide a sharp cut-off either above or below a particular wavelength. They are denoted by their cut-on and cut-off wavelength at 50 % of peak transmission. The spectra of light that can be obtained based on the use of these filters are illustrated in Fig. B.3.

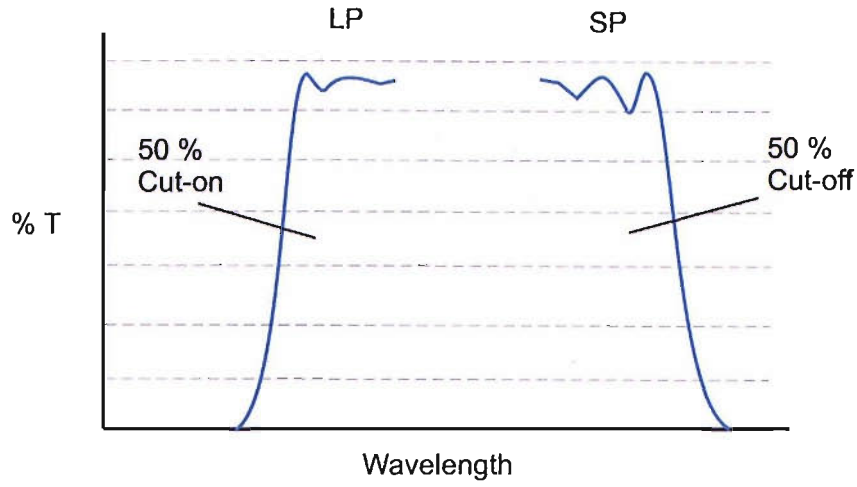

FIGURE B.3: Nomenclature for transmission characteristics of longpass and short-pass filters.

B.2.2 Monochromators

Monochromators are instruments that can filter a narrow band wavelength range from a broadband source. The systems generally consisted of (1) entrance and exit slits that allow the light to enter and exit the systems, (2) lenses or mirrors for the collimation of undispersed light and the focusing of dispered light and (3) dispersing elements, e.g., prism or grating that can separate the colors of light.

Figure B.4 shows common mountings for prism and grating systems. The white light is focussed on the entrance slit S and falls on a lens L_1 (or spherical mirror M_1) which makes its beam roughly parallel. The beam then reaches the dispersing element D which can be a prism or diffraction grating. Different wavelengths then follow different directions and are refocussed by another lens (or spherical mirror M_2). The diffracted spectrum falls into a narrow slit in the wall W and is detected by the photo detector (P) placed behind the slit.

B.3 Detectors

The most important light detector that is typically used in the spectrofluorometer is a photomultiplier tube (PMT). The PMT is an evacuated tube whose principle of operation is based on the photoelecric effect. The tube contains a photo emissive

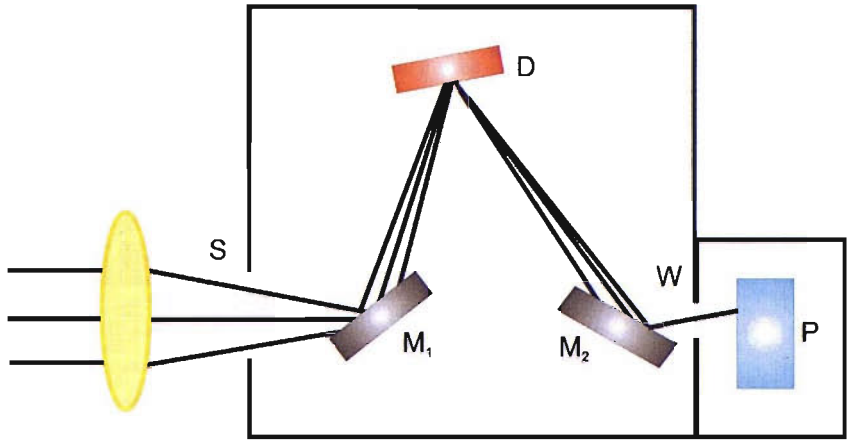

FIGURE B.4: Schematic diagram of a monochromator. S, slit; M_1. M_2, spherical mirrors (or lenses); D, dispering element (grating or prism) ; W, wall; P, photo detector.

surface called the photocathode and a series of additional anodes called dynodes[1] that collect electrons emitted from the photocathode (see Fig. B.5).

An electron ejected from the photocathode by incident radiation is accelerated over a number of dynodes to produce an avalanche of secondary electrons. There is thus a multiplication of the number of electrons produced at the photocathode or equivalently an amplification of the current.

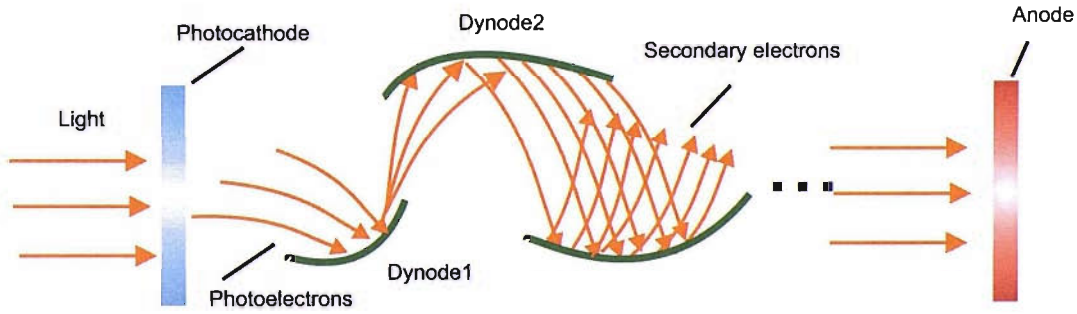

FIGURE B.5: Components of a photomultiplier tube.

[1]The dynodes are coated with a material that losses secondary electrons when it is hit by incident electrons.

Appendix C

Current-Voltage Characteristics of Thin Film c-Si Solar Cells

This section presents current-voltage characteristics of thin film c-si solar cells fabricated on SOI wafers (batch K2797s). The measurement setup described in section 3.3.2 was used to obtain the I-V results. Only five wafers were tested in this study since seven of them were lost during the serious fire in the Mountbatten Clean Room Complex on 30^{th} October 2005. The tested results are summarised in table Table C.1. As an example, the I-V curves of some devices (cells c4-2, c5-1, c8-10, c12-1) are presented in Fig. C.1.

TABLE C.1: Device parameters of thin film c-Si solar cells

Cell number	I_{sc} (A)	V_{oc} (V)	FF	Efficiency (%)	Cell Structure
c3-2	2.1×10^{-4}	0.16	0.23	0.01	Waffle cell
c3-4	7.7×10^{-4}	0.39	0.20	0.06	Strip cell
c3-9	7.2×10^{-4}	0.16	0.13	0.02	Waffle cell
c3-10	4.4×10^{-4}	0.39	0.27	0.05	Strip cell
c4-2	1.5×10^{-3}	0.36	0.36	0.20	Strip cell
c4-3	1.5×10^{-3}	0.47	0.28	0.20	Strip cell
c4-4	1.8×10^{-5}	0.15	0.25	0.001	Waffle cell
c4-5	8.8×10^{-4}	0.32	0.29	0.08	Strip cell
c4-9	1.6×10^{-3}	0.32	0.33	0.17	Strip cell
c5-1	4.1×10^{-3}	0.48	0.43	0.84	Waffle cell
c5-2	2.0×10^{-3}	0.46	0.37	0.34	Waffle cell
c5-3	1.3×10^{-3}	0.42	0.26	0.15	Waffle cell
c5-5	2.0×10^{-3}	0.36	0.21	0.15	Strip cell
c5-6	2.4×10^{-4}	0.14	0.27	0.009	Strip cell

Cell number	I_{sc} (A)	V_{oc} (V)	FF	Efficiency (%)	Cell Structure
c5-7	1.0×10^{-3}	0.38	0.42	0.16	Strip cell
c8-1	3.1×10^{-3}	0.08	0.37	0.09	Waffle cell
c8-2	2.0×10^{-3}	0.09	0.36	0.06	Waffle cell
c8-3	1.9×10^{-3}	0.12	0.39	0.09	Waffle cell
c8-4	5.7×10^{-4}	0.22	0.24	0.03	Waffle cell
c8-5	8.6×10^{-4}	0.25	0.37	0.08	Strip cell
c8-8	1.5×10^{-4}	0.39	0.18	0.01	Strip cell
c8-10	2.7×10^{-3}	0.42	0.40	0.45	Strip cell
c12-1	1.0×10^{-3}	0.12	0.33	0.04	Strip cell
c12-3	1.7×10^{-3}	0.21	0.23	0.08	Strip cell
c12-4	2.5×10^{-4}	0.35	0.29	0.025	Strip cell
c12-5	1.9×10^{-4}	0.17	0.26	0.008	Strip cell
c12-8	9.8×10^{-5}	0.08	0.27	0.002	Waffle cell
c12-9	3.1×10^{-5}	0.14	0.21	0.001	Waffle cell

* Note that the I-V characteristics of 10 cells from each wafer (wafer c3, c4, c5, c8 and c12) were inspected. The device parameters of the cells which can give some power output are presented in this table.

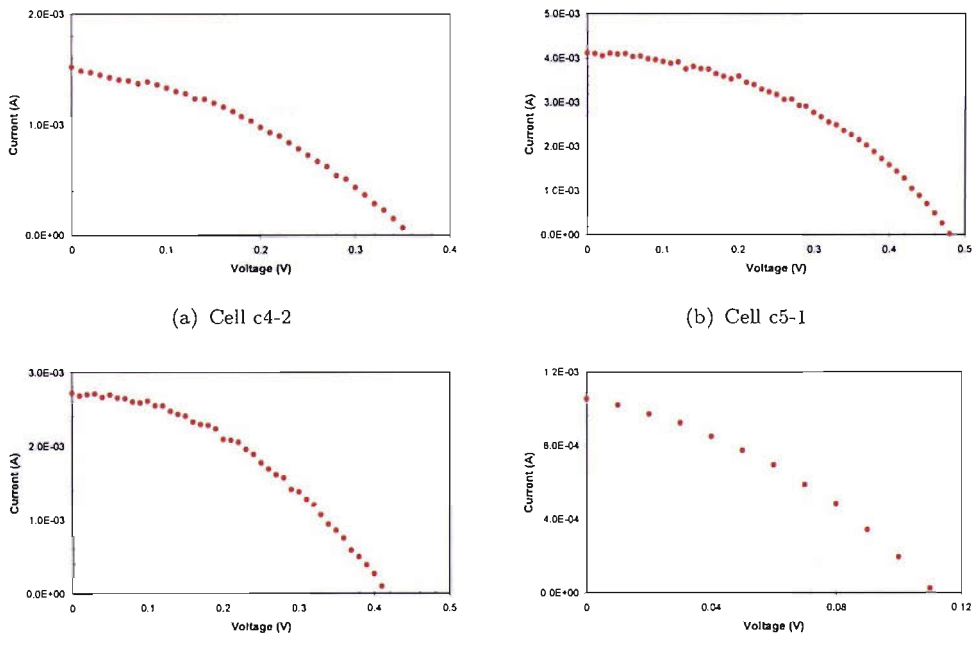

(a) Cell c4-2

(b) Cell c5-1

(c) Cell c8-10

(d) Cell c12-1

FIGURE C.1: I-V Characteristics (under light condition) of thin film c-Si solar cells.

It can be seen that the fabricated thin film cells exhibit poor I-V characteristics. The efficiency obtained from these cells is less than 1%. This low electrical performance is caused by various reasons. One of the major reasons is due to some device regions were left non-passivated. The non-passivated areas were created during the etching process to form the trench (see Fig. C.2). It can result in high surface recombination and low minority carrier lifetimes. Another reason is because there is some fault in the designed masks. It was found from the designed masks that the p-type contact area of one design is connected to the n-type region. Therefore, it resulted in a short circuit of some fabricated cells. In addition to these reasons, there are also some issues concerning the gold contamination[1] during the DRIE process and condition of the diffusion process that was used to form the n^+ and p^+ regions. Since the DRIE machine had also been used for etching some gold coated wafers, the solar cell wafers that were processed in this machine might have been contaminated by the gold. Moreover, the process, that was used to form these regions, was optimised for the c-Si wafers (FZ) but not the SOI wafers that used to fabricate these thin film cells. Thus, it may result in an un-desirable heavily doped region that was observed from the previous batch. All these issues, however, need to be investigated further before the final conclusion can be made.

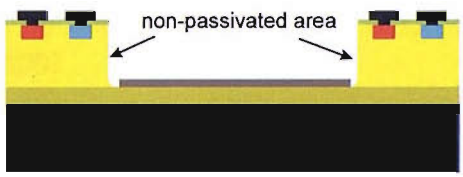

FIGURE C.2: A cross section of thin-film device. The non-passivated areas are pointed by the arrows.

[1]Gold is known as a 'lifetime killer' impurities, which shorten the lifetime of generated carriers in silicon solar cells [119].

References

[1] Key world energy statistics. International Energy Agency (IEA), 2004 Edition, 2004.

[2] CO2 emissions. URL http://www.greenpeace.org/international/campaigns/climate-change/science/co2_emissions. Last accessed: April 10th, 2007.

[3] The Effect of Finite Fossil Fuel Reserves on Climate Change Potential. URL http://www.hm-treasury.gov.uk/media/DDF/7C/climatechange_keithjackson_3.pdf. Last accessed: April 10th, 2007.

[4] Glossary of Energy-Related Terms. URL http://www.eere.energy.gov/consumer/information_resources/index.cfm/mytopic=60001. Last accessed: April 10th, 2007.

[5] G. Beaucarne, G. Agostinelli, L. Carnel, P. Choulat, H. Dekkers, V. Depauw, F. Dross, F. Duerinckx, Chun Gong, I. Gordon, I.K Filipek, Y. Ma, N. E. Posthuma, D. Van Gestel, E.V. Kerschaver, K.V. Nieuwenhuysen, E. Vermarien, and J. Poortmans. Thin, thinner, thinnest: An evolutionary vision of crystalline si technology. In *21st European Photovoltaic Solar Energy Conference*, pages 554–559, Dresden, Germany, 2006.

[6] A. Goetzberger and V.U. Hoffmann. *Photovoltaic Solar Energy Generation.* Springer, Berlin, Germany, 2005.

[7] R. Brendel. Crystalline thin-film silicon solar cells from layer-transfer processes: a review. In *Proceeding of 10th Workshop on Crystalline Silicon Solar Cell Materials and Processes*, pages 117–125, Copper Mountain, USA, 2000.

[8] G. Smestad, H. Ries, R. Winston, and E. Yablonovitch. The thermodynamic limit of light concentrators. *Solar Energy Materials*, 21:99–111, 1990.

[9] A. Luque. *Solar Cells and Optics for Photovoltaic Concentration.* Adam Hilger, Bristol, England, 1989.

[10] W.H. Weber and J. Lambe. Luminescent greenhouse collector for solar radiation. *Applied Optics*, 15:2299–2300, 1976.

[11] A. Goetzberger and W. Greubel. Solar energy conversion with fluorescent collectors. *Applied Physics*, 14:123–139, 1977.

[12] Lumogen F. URL `http://www.basf.com/additives/pdfs/p3201e.pdf`. Last accessed: April 10th, 2007.

[13] N. Panchuk-Voloshina, R.P. Haugland, J. BishopStewart, M.K. Bhalgat, P.J. Millard, F. Mao, W. Leung, and R.P. Haugland. Alexa dyes, a series of new fluorescent dyes that yield exceptionally bright, photostable conjugates. *J. of Histochemistry and Cytochemistry*, 47:1179–1188, 1999.

[14] K. Barnham, J.L. Marques, J. Hassard, and P.O. Brien. Quantum-dot concentrator and thermodynamic model for the global redshift. *Applied Physics Letters*, 76:1197–1199, 2000.

[15] B.S. Richards, A. Shalav, and R.P. Corkish. A low escape-cone-loss luminescent solar concentrator. In *Proc. 19th European Photovoltaic Solar Energy Conference*, pages 113–116, Paria, France, 2004.

[16] U. Rau, F. Einsele, and G. Glaeser. Efficiency limits of photovoltaic fluorescent collectors. *Applied Physics Letters*, 87:171101, 2005.

[17] A.J. Chatten, K.W.J. Barnham, B.F. Buxton, N.J. Ekins-Daukes, and M.A. Malik. A new approach to modelling quantum dot concentrators. *Solar Enegy Materials and Solar Cells*, 75:363–371, 2003.

[18] T. Markvart, L. Danos, P. Kittidachachan, and R. Greef. Detailed balance efficiency of ideal single-stage fluorescent collectors. In *Proc. 20th European Photovoltaic Solar Energy Conference*, pages Pre–print, Bacelona, Spain, 2005.

[19] L. Danos, P. Kittidachachan, T.J.J. Meyer, R. Greef, and T. Markvart. Characterisation of fluorescent collectors based on solid, liquid, and langmuir blodget (lb) films. In *21st European Photovoltaic Solar Energy Conference*, pages 443–446, Dresden, Germany, 2006.

[20] L.H. Sloof, R. Kinderman, A.R. Burgers, J.A.M. van Roosmalen, A. Buchtemann, R. Danz, M. Schleusener, A.J. Chatten, D.J. Farrell, and K.W.J. Barnham. The luminescent concentrator: A bright idea for spectrum conversion. In *Proc. 20th European Photovoltaic Solar Energy Conference*, pages Pre–print, Bacelona, Spain, 2005.

[21] A.R. Burgers, L.H. Sloof, R. Kinderman, and J.A.M. van Roosmalen. Modelling of luminescent concentrators by ray-tracing. In *Proc. 20th European Photovoltaic Solar Energy Conference*, pages Pre–print, Bacelona, Spain, 2005.

[22] S.T. Bailey, G.E. Lokey, M.S. Hanes, J.D.M. Shearer, J.B. McLafferty, G.T. Beaumont, T.T. Baseler, J.M. Layhue, D.R. Broussard, Y. Zhang, and B.P. Wittmershaus. Optimized excitation energy transfer in a three-dye luminescent solar concentrator. *Solar Energy Materials and Solar Cells*, 91:67–75, 2007.

[23] M. Hammam, M.K. El-Mansy, S.M. El-Bashir, and M.G. El-Shaarawy. Performance evaluation of thin-film solar concentrators for greenhouse applications. *Desalination*, 209:244–250, 2007.

[24] S.M. Sze. *Physics of semiconductor devices.* John Wiley and Sons Inc., New York, USA, 1981.

[25] C.T. Sah, R.N. Noyce, and W. Shockley. Carrier generation and recombination in p-n junctions and p-n junction characteristics. *Institute of Radio Engineers*, page 1228, 1957.

[26] J. Nelson. *Physics of solar Cells.* Imperial College Press, London, UK, 2003.

[27] Solar Grossary. URL `http://www.enviroharvest.ca/solar_glossary.htm`. Last accessed: April 10th, 2007.

[28] G.P. Smestad. *Optoelectronics of Solar Cells.* SPIE-The international Spcoety for Optical Engineering, Washington, USA, 2002.

[29] T. Markvart and L. Castaner. *Practical Handbook of Photovoltaics: Fundamental and Applications.* Elsevier Ltd., United Kingdom, 2003.

[30] T. Markvart. Photovoltaic solar energy conversion. European Summer University: Energy for Europe, Strasbourg, 2002.

[31] M.A. Green. *Solar Cells: Advanced Principles and Practices.* Centre for Photovoltaic Devices and Systems, Sydney, Australia, 1995.

[32] W. Shockley and H.J. Queisser. Detailed balance limit of efficiency of p-n junction solar cells. *J. Appl. Phys.*, 32:510–519, 1961.

[33] T. Markvart and L. Castaner. *Practical Handbook of Photovoltaics: Fundamental and Applications.* Elsevier Ltd., 2003.

[34] M.A. Green. *High efficiency silicon solar cells.* Trans Tech Publications, Switzerland, 1987.

[35] B. Valeur. *Molecular Fluorescence: Principles and Applications.* Wiley-VCH, New York, USA, 2002.

[36] F.G. Smith and T.A. King. *Optics and Photonics: An Introduction.* John Wiley and Sons, Ltd., New York, USA, 2004.

[37] Anti-reflective/coating. URL `http://en.wikipedia.org/wiki/Anti-reflective_coating`. Last accessed: April 10th, 2007.

[38] M.A. Green. *Solar Cells: Operating Principles, Technology and System Applications.* The University of New South Wales, Kensington, NSW, 1982.

[39] Coating Theory. URL `http://www.mellesgriot.com/products/optics/oc_2_2.htm`. Last accessed: April 10th, 2007.

[40] S.R. Wenham, M.A. Green, M.E. Watt, and R. Corkish. *Applied Photovoltaics (2nd Edition).* Centre of Photovoltaic Engineering, Sydney, Australia, 2006.

[41] A.G. Aberle. *Crystalline silicon solar cells: Advanced surface passivation and analysis.* Centre of Photovoltaic Engineering, Sydney, Australia, 2004.

[42] RCA Clean. URL `http://www.mines.edu/fs_home/cwolden/chen435/clean.htm`. Last accessed: July 2nd, 2007.

[43] L.S. Tan, L.C.P. Tan, M.S. Leong, R.G. Mazur, and C.W. Ye. Characterization of ultrashallow dopant profiles using spreading resistance profiling. *Journal of Vacuum Science & Technology B: Microelectronics and Nanometer Structures*, 20:483–487, 2002.

[44] R.B. Fair and J.C.C. Tsai. A quantitative model for the diffusion of phosphorus in silicon and the emitter dip effect. *J. of the Electrochemical Society*, 124:1107–1118, 1977.

[45] M. Uematsu. Simulation of boron, phosphorus, and arsenic diffusion in silicon based on an integrated diffusion model, and the anomalous phosphorus diffusion mechanism. *J. of Applied Physics*, 82:2228–2246, 1997.

[46] A. Bentzen, A. Holt, J.S. Christensen, and B.G. Svensson. High concentration in-diffusion of phosphorus in si from a spray-on source. *J. of Applied Physics*, 99:064502, 2006.

[47] G. Masetti, D. Nobili, and S. Solmi. Profiles of phosphorus predeposited in silicon and carrier concentration in equilibrium with sip precipitates. In *Proceedings of the 3rd International Symposium on Silicon Materials Science and Technology*, pages 648–657, Philadelphia, 1977.

[48] S. Solmi, A. Parisini, R. Angelucci, A. Armigliato, D. Nobili, and L. Moro. Dopant and carrier concentration in si in equilibrium with monoclinic sip precipitates. *Physical Review B*, 53:7836–7841, 1996.

[49] M.G. Dowsett, G.A. Cooke, D.I. Elliner, T.I. Ormsby, and A. Murrell. Experimental techniques for ultra-shallow profiling using sub-kev primary ion beams. In *Proceeding of SIMS XI*, 1997.

[50] ASTM F723-88: Standard practice for conversion between resistivity, dopant density for Boron-doped, and Phosphorus doped silicon. *ASTM Annual Standards*, 10, 1996.

[51] S.M. Sze. *Semiconductor devices: Physics and Technology.* John Wiley and Sons Inc., New York, USA, 1985.

[52] A.R. Burgers, J.A. Eikelboom, A. Schbnecker, and W.C. Sinke. Improved treatment of the strongly varying slope in fitting solar cell i-v curves. In *Conference Record of the 25th IEEE Photovoltaic Specialists Conference*, pages 569–572, Washington, USA, 1996.

[53] P.K. Singh, R. Kumar, P.N. Vinod, B.C. Chahravarty, and S.N. Singh. Effect of spatial variation of incident radiation on spectral response of a large area silicon solar cell and the cell parameters determined from it. *Solar Energy Materials and Solar Cells*, 80:21–31, 2003.

[54] Technical Guide. A guide to integrating sphere theory and applications. Labsphere Inc.

[55] H.G. Tompkins and W.A. McGahan. *Spectroscopic ellipsometry and reflectometry: A User's Guide.* John Wiley and Sons Inc., New York, USA, 1999.

[56] P. Kittidachachan, T. Markvart, D.M. Bagnall, R. Greef, and G.J. Ensell. An analysis of a dead layer in the emitter of $n^+/p/p^+/$ solar cells. *Solar Energy Material and Solar Cells*, 91:160–166, 2007.

[57] J. Sinkkonen, A. Hovinen, T. Sirtola, E. Tuominen, and M. Acerbis. Interpretation of the spatial response of a solar cell in terms of the spatial collection

efficiency. In *Proc. 25th IEEE Photovoltaic Specialist Conf.*, pages 561–564, Washington DC, 1996.

[58] C. Donolato. Reconstruction of the charge collection probability in a solar cell from internal quantum efficiency measurements. *J. Appl. Phys.*, 89:5687–5695, 2001.

[59] J. del Alamo and R.M. Swanson. The physics and modeling of heavily doped emitters. *IEEE Trans. Electron Devices*, 31:1878–1888, 1984.

[60] T. Markvart. Relationship between dark carrier distribution and photogenerated carrier collection in solar cells. *IEEE Trans. Electron Devices.*, 43:1034–1036, 1996.

[61] A. Cuevas, P.A. Basore, G. Girouit-Matlakowski, and C. Dubois. Surface recombination velocity of highly doped n-type silicon. *J. Appl. Phys.*, 80:3370–3375, 1996.

[62] P.A. Basore. Extended spectral analysis of internal quantum efficiency. In *Proceedings of the 23rd IEEE Photovoltaic Specialists Conference*, pages 147–152, IEEE, New York, 1993.

[63] A.H. Zewail and J.S. Batchelder. Luminescent solar concentrators: An overview. Polymers in Solar Energy Utilization, 1983.

[64] J.A. Levitt and W.H. Weber. Materials for luminescent greenhouse solar collectors. *Applied Optics*, 16:2684–2689, 1977.

[65] B.A. Swatz, T. Cole, and A.H. Zewail. Photon trapping and energy transfer in multiple-dye plastic matrices: an efficient solar-energy concentrator. *Optics Letters*, 1:73–75, 1977.

[66] C.F. Rapp and N.L. Boiling. Luminescent solar concentrators. In *Proc. 13th IEEE Photovoltaic Specialists Conference*, pages 690–693, Berlin, Germany, 1978.

[67] J.S. Batchelder, A.H. Zewail, and T. Cole. Luminescent solar concentrators. 1: Theory of operation and techniques for performance evaluation. *Applied Optics*, 18:3090–3109, 1979.

[68] J.S. Batchelder, A.H. Zewail, and T. Cole. Luminescent solar concentrators. 2:experimental and theoretical analysis of their possible efficiencies. *Applied Optics*, 20:3733–3754, 1981.

[69] V. Wittwer, K. Heidler, A. Zastrow, and A. Goetzberger. Theory of fluorescent planar concentrators and experimental results. *J. of Luminescent*, 24:873–876, 1981.

[70] V. Wittwer, W. Stahl, and A. Goetzberger. Fluorescent planar concentrators. *Solar Energy Materials*, 11:187–197, 1984.

[71] R. Reisfeld. Luminescent solar concentrators – a review. United State Patent No. 4367367, 1983.

[72] R. Reisfeld and C.K. Jorgensen. Luminescent solar concentrators for energy conversion. *Structure and Bonding*, 49:1–36, 1982.

[73] A.M. Hermann. Luminescent solar concentrators – a review. *Solar Energy*, 29: 323–329, 1982.

[74] A. Zastrow. The physics and applications of fluorescent concentrators: A review. *Proc. SPIE The International Society for Optical Engineerings*, 2255:534–547, 1994.

[75] Hot mirror. URL `http://en.wikipedia.org/wiki/Hot_mirror`. Last accessed: Sep 2nd, 2007.

[76] J.C. Goldschmidt, M. Peters, P. Loper, S.W. Glunz, A. Gombert, and G. Willeke. Photon management for full spectrum utilization with fluorescent materials. In *19th Workshop on Quantum Solar Energy Conversion - QUANTSOL 2007*, pages 12–13, Salzburg, Austria, 2007.

[77] A.J. Chatten, D.J. Farrell, C. Jermyn, P. Thomas, B.F. Buxton, A. Buchtemann, R. Danz, and K.W.J. Barnham. Thermodynamic modelling of luminescent solar concentrators. In *Proc. 31st Photovoltaic Specialists Conference*, pages 82–85, Orlando, Florida, 2005.

[78] T. Markvart. Detailed balance method for ideal single–stage fluorescent collectors. *J. Applied Physics*, 99:026101, 2006.

[79] K. Heidler, V. Witter, and A. Goetzberger. Fluorescent planar concentrator (fpc) monte carlo computer model limit efficiency and lastest experimental results. In *Proc. of 4th E.C. Photovoltaic Solar Energy Conference*, pages 682–686, Stresa,Italy, 1982.

[80] F. Agullo-Lopez, M. Carrascosa, and S. Unamunu. Monte carlo simulation of the performance of pmma luminescent solar collectors. *Applied Optics*, 22:3236–3241, 1983.

[81] S.J. Gallagher, P.C. Eames, and B. Norton. Quantum dot solar concentrator behaviour, predicted using a ray trace approach. *J. of Ambient Energy*, 25: 47–56, 2004.

[82] A.R. Burgers, L.H. Sloof, A. Buchtemann, and J. van Roosmalen. Performance of single layer luminescent concentrators with multiple dyes. In *Proc. of IEEE 4th WCPEC*, pages Pre–print, Hawaii, USA, 2006.

[83] K.R. McIntosh and B.S. Richards. Increased mc-si module efficiency using fluorescent organic dyes: A ray-tracing study. In *Proc. of IEEE 4th World Conference on Photovoltaic Energy Conversion*, pages Pre–print, Hawaii, USA, 2006.

[84] J.R. Lakowicz. *Principles of Fluorescence spectroscopy.* Kluwer Academic/-Plenum Publishers, New York, USA, 1999.

[85] M.A. Baldo, M.E. Thompson, and S.R. Forrest. Phosphorescent materials for application to organic light emitting devices. *Pure Appl. Chem.*, 71:2095–2106, 1999.

[86] F. Wilkinson. Electronic energy transfer between organic molecules in solution. *Adv. Photochem.*, 3:241–269, 1964.

[87] A.M. Taleb. Self absorption treatment for the luminescent solar concentrators. *Renewable Energy*, 26:137–142, 2002.

[88] J.S. Batchelder. The luminescent solar concentrator. PhD. Thesis, California Institute of Technology, 1982.

[89] B. Heeg, P.A. DeBarber, and G. Rumbles. Influence of fluorescence reabsorption and trapping on solid-state optical cooling. *Applied Optic*, 44:3117–3123, 2005.

[90] A.N.A. Rahman and A.F. Mansour. Trans-thioindigo as a possible dye for solar collectors. *J.Phys.D: Appl.Phys.*, 18:L49–L52, 1985.

[91] Front-face detection for highly-concentrated, opaque, or solid samples. URL `www.jobinyvon.com/usadivisions/fluorescence/applications/F-03_Front-Face_Det.pdf`.

[92] M. Yamashita, M. Nomura, S. Kobayashi, T. Sato, and K. Aizawa. Picosecond time-resolved fluorescence spectroscopy of hematoporphyrin derivative. *IEEE J. of Quantum Electronics*, pages 1363–1369, 1984.

[93] N.N. Barashkov, M.E. Globus, A.A. Ishchenko, I.P. Krainov, T.M.Muraveva, V.V. Pomerantsev, V.V. Popov, O.K. Rossikhina, V.G. Senchishin, A.V. Sidelnikova, and V.M. Shershukov. Present state of research on luminescent solar concentrators (review). *Journal of Applied Spectroscopy*, 55:1193–1205, 1992.

[94] A.F. Mansour, M.G. El-Shaarawy, M.K. El-Mansy S.M. El-Bashir, and M. Hammam. Optical study of perylene dye doped poly(methylmethacrylate) as fluorescent solar collector. *Polymer International*, 51:393–397, 2002.

[95] S.A. Evenson and A.H. Rawicz. Thin film luminescent concentrators for integrated devices. *Applied Opics*, 34, 1995.

[96] About PhotochemCAD. URL `http://www.photochemcad.com/`. Last accessed: April 10th, 2007.

[97] F.L. Arbeloa, T.L. Arbeloa, I.L. Arbeloa, A. Costela, I.G. Moreno, J.M. Figuera, F.A. Guerri, and R. Sastre. Relations between photophysical and lasing properties of rhodamines in solid polymeric matrices. *Applied Physics: B*, 64:651–657, 1997.

[98] D. Avnir, D. Levy, and R. Reisfeld. The nature of the silica cage as reflected by spectral changes and enhanced photostability of trapped rhodamine 6g. *J. Phys. Chem.*, 88:5956, 1984.

[99] D. Magde, R. Wong, and P.G. Seybold. Fluorescence quantum yields and their relation to lifetimes of rhodamine 6g and fluorescein in nine solvents: Improved absolute standards for quantum yields. *Photochemistry and Photobiology*, 75: 327–334, 2002.

[100] Methyl methacrylate. URL `http://en.wikipedia.org/wiki/Methyl_methacrylate`. Last accessed: April 10th, 2007.

[101] M.J. Weber. *Handbook of Optical Materials.* CRC Press, London, UK, 2003.

[102] R. Capan, A.K. Ray, T. Tanrisever, and A.K. Hassan. Spun thin films of poly(methylmethacrylate) polymer for benzene sensing. *Smart Mater. Struct.*, 14:N11–N15, 2005.

[103] P.J. Scully, D. Jones, and D.A. Jaroszynski. Femtosecond laser irradiation of polymethylmethacrylate for refractive index gratings. *J. Opt. A: Pure Appl. Opt.*, 5:S92–96, 2003.

[104] J.S. Batchelder. *The Luminescent Solar Concentrator.* PhD Thesis, California Institute of Technology, 1982.

[105] Acrylic glass. URL `http://en.wikipedia.org/wiki/Acrylic_glass`. Last accessed: April 10th, 2007.

[106] The form talysurf series 2: Operator's handbook.

[107] J.R. Lakowicz. *Principles of Fluorescence Spectroscopy, 3rd Edition.* Springer-Verlag New York Inc., Singapore, 2006.

[108] F.L Arbeloa, T.Lopez Arbeloa, I.L Arbeloa, A. Costela, I.Garcia-Moreno, J.M. Figuera, F.Amat-Guerri, and R. Sastre. Relations between photophysical and lasing properties of rhodamines in solid polymeric matrices. *Appl. Phys. B*, 64: 651–657, 1997.

[109] T. Wakebe and E.V. Keuren. The excitation spectra of two-photon induced fluorescence in xanthene dyes. *Jpn. J. Appl. Phys.*, 38:3556–3561, 1999.

[110] R.W. Olson, R.F. Loring, and M.D. Fayer. Luminescent solar concentrators and the reabsorption problem. *Applied Optics*, 20:2934–2940, 1981.

[111] J. Sansregret, J.M. Drake, W.R.L. Thomas, and M.L. Lesiecki. Light transport in planar luminescent solar concentrators: the role of dcm self-absorption. *Applied Optics*, 22:573–577, 1983.

[112] R. Soti, E. Farkas, M. Hilbert, Z. Farkas, and I. Ketskemety. Photon transport in luminsecent solar concentrators. *J. Luminescence*, 68:105–114, 1996.

[113] M.L. Lesiecki and J.M. Drake. Use of the thermal lens technique to measure the luminescent quantum yields of dyes in pmma for luminescent solar concentrators. *Applied Optics*, 21:557–560, 1982.

[114] A. Nakajima. Effect of dipolar molecules on intermolecular exciplexes. *J. of Luminescence*, 16:279–283, 2004.

[115] A. Kurian, N.A. George, B. Paul, V.P.N. Nampoori, and C.P.G. Vallabhan. Studies on fluorescence efficiency and photodegradation of rhodamine 6g doped pmma using a dual beam thermal lens technique. *Laser Chemistry*, 20:99–110, 2002.

[116] E. Loh Jr. and D.J. Scalapino. Luminescent solar concentrators: effects of shape on efficiency. *Applied Optics*, 25:1901–1907, 1986.

[117] S.A. Boden. Antireflection and light trapping for photovoltaics. Nine Month Progress Report, NSI, School of Electronics and Computer Sciences, 2005.

[118] J.A. Gardecki and M. Maroncelli. Set of secondary emission standards for calibration of the spectra responsivity in emission spectroscopy. *Applied Spectroscopy*, 52:1179–1189, 1998.

[119] S. Dubois, O. Palais, M.P. Pasquinelli, S. Martinuzzi, and C. Jaussaud. Influence of substitution metallic impurities on the performances of p-type crystalline silicon solar cells: The case of gold. *J. of Applied Physics*, 100:123502, 2006.

Bibliography

[1] S.M. Sze. *Semiconductor Devices: Physics and Technology*, John Wiley and Sons, Singapore, 1985.

[2] E. Hecht. *Optics*, Addison-Wesley Publishing Company, Massachusetts, USA, 1987.

[3] S.P. Parker. *Spectroscopy Source Book*, McGraw-Hill Book Company, New York, USA, 1988.

[4] M.A. Green. *Silicon Solar Cells: Advanced Principles and Practice*, Centre for Photovoltaic Devices and Systems, Sydney, Australia, 1995.

[5] J.R. Lakowicz. *Principles of Fluorescence Spectroscopy*, Kluwer Academic/Plenum Publishers, New York, USA, 1999.

[6] M.J. Madou. *Fundamentals of Microfabrication: The Science of Miniaturization*, CRC Press LLC., New York, USA, 2002.

[7] G.P. Smestad. *Optoelectronics of Solar Cells*, The International Society for Optical Engineering, Washington, USA, 2002.

[8] B. Valeur. *Molecular Fluorescence: Principles and Applications*, Wiley-VCH Verlag GmbH, Wienheim, Germany, 2002.

[9] T. Markvart and L. Castaner. *Photovoltaics: Fundamentals and Applications*, Elsevier Science Ltd., Oxford, UK, 2003.

[10] J. Nelson. *The Physics of Solar Cells*, Imperial College Press, London, UK, 2003.

[11] F.G. Smith and T.A. King. *Optics and Photonics: An Introduction*, John Wiley and Sons, Ltd., England, UK, 2004.

[12] D.K. Schroder. *Semiconductor Material and Device Characterization*, John Wiley and Sons, Inc., New Jersey, USA, 2006.